PRACA DOKTORSKA

Thermal properties and thermal residual stresses in graded Al–matrix composites reinforced with Al_2O_3 and SiC particles: Experiments and Numerical simulations.

mgr inż. Anil Antony Sequeira

Promotor

prof. dr hab. inż. Michał Basista

Promotor pomocniczy

dr inż. Witold Węglewski

Warszawa 2025

Abstract

Functionally graded materials (FGMs) based on aluminum alloys, which are the subject of this thesis, are advanced metal matrix composites designed for high–stress, high–temperature operating conditions that offer superior performance of structural components due to gradual spatial variation of mechanical and thermal properties of these materials. The motivation for investigating the thermal properties and thermal residual stresses of graded Al–matrix composites reinforced with Al_2O_3 and SiC ceramic particles stems from the automotive industry's demand for innovative structural materials for brake discs. Graded Al–matrix composites are competitive material choices for modern brake discs due to their high specific strength, high thermal conductivity, and wear resistance. A properly designed graded structure of Al/Al_2O_3 and Al/SiC FGMs can help reduce process–induced thermal residual stresses and effectively dissipate heat generated during brake operation. The choice of two alternative ceramic particles (Al_2O_3 vs. SiC) for the reinforcement of an Al alloy matrix was inspired by similar studies carried out in the research laboratories of car manufacturers (e.g., CR FIAT and Audi).

In this work, stepwise graded (or layered) aluminum alloy matrix composites $AlSi12+vAl_2O_3$ and AlSi12+vSiC, where v = 10, 20, 30 vol.%, were prepared using powder metallurgy. The powder mixtures of AlSi12, Al_2O_3 and SiC used to obtain composite layers and FGMs were prepared in a planetary ball mill. Hot pressing (HP) and spark plasma sintering (SPS) were used as powder consolidation techniques. Microstructural characterization was performed using scanning electron microscopy (SEM) and microcomputed X–ray tomography (micro–XCT). The thermal conductivity of composite layers and FGMs was evaluated using the laser flash technique within a temperature range that is relevant to brake disc application (from RT to 300°C–500°C). The coefficient of thermal expansion (CTE) was determined for a case study of AlSi12+vSiC composites from dilatometry experiments for RT to 500°C. Thermal residual stresses were measured using neutron diffraction. Additionally, Taber linear abrasion wear tests were conducted to evaluate the tribological properties of the $AlSi12+vAl_2O_3$ and AlSi12+vSiC composites and compare them with grey cast iron, a standard material used in brake discs.

The optimization of the powder mixing and consolidation process parameters has yielded composite layers and FGMs of high relative density. Overall, the samples manufactured by HP were less porous than the SPS samples and the $AlSi12+vAl_2O_3$ composites were less porous than AlSi12+vSiC composites. The thermal conductivity measurements showed that the ungraded composites exhibited lower conductivity with increasing ceramic content for both $AlSi12+vAl_2O_3$ and AlSi12+vSiC composites. For $AlSi12+vAl_2O_3$ composites, porosity and interfacial thermal resistance were identified as the key factors reducing thermal conductivity. In the case of AlSi12+vSiC composites, the formation of thin layers of oxides (Al_2O_3), and interfacial thermal resistance were the main contributors to this reduction. The graded

composites exhibited nearly constant thermal conductivity across the tested temperature ranges, achieving thermal conductivity that is at least twice that of conventional gray cast iron. This renders them a promising candidate for use in brake disc applications.

Micro–XCT–based finite element (FE) models, representing the actual microstructure, including defects such as pores, and accounting for thermal conductance at the metal–ceramic interface, were used in the numerical simulations. Numerical simulations of thermal conductivity showed excellent agreement with the experimental data, with relative errors ranging from 4% to 6%. Thermal residual stresses were found to be lower in graded composites compared to ungraded ones, as confirmed by neutron diffraction measurements. The micro–XCT–based FEM models predicted residual stresses with an accuracy of less than 5% deviation from the experimental data.

Dilatometric experiments revealed that the coefficient of thermal expansion (CTE) in the direction parallel to the pressing direction of graded composites was significantly lower than that in the direction perpendicular to the pressing direction. Overall, the graded composites demonstrated a favorable CTE, approximately 32% lower than that of the aluminum alloy (AlSi12) matrix, indicating enhanced thermal stability and suitability for applications requiring minimal dimensional changes under varying temperature conditions.

This study successfully investigated the thermal properties, thermal residual stresses, and tribological performance of graded AlSi12–matrix composites reinforced with Al_2O_3 and SiC particles, combining experimental and numerical approaches. The findings highlight the potential of functionally graded composites as high–performance materials for automotive brake discs, offering superior thermal conductivity, reduced residual stresses, enhanced thermal stability. The agreement between the experimental and numerical results validates the robustness of the proposed numerical models, helping in further exploration and application of graded composites in industrial settings.

Streszczenie

Materiały funkcjonalne gradientowe (FGM) oparte na stopach aluminium, które są przedmiotem niniejszej rozprawy, są zaawansowanymi kompozytami o osnowie metalowej zaprojektowanymi do pracy w warunkach podwyższonych naprężeń i temperatury, które zapewniają efektywne działanie elementów konstrukcji dzięki stopniowej przestrzennej zmianie właściwości mechanicznych i termicznych. Motywacja do zbadania właściwości termicznych i termicznych naprężeń resztkowych gradientowych kompozytów na osnowie aluminiowej wzmacnianych cząstkami ceramicznymi Al_2O_3 i SiC wynika z zapotrzebowania przemysłu motoryzacyjnego na innowacyjne materiały konstrukcyjne do tarcz hamulcowych. Kompozyty gradientowe na osnowie aluminiowej są konkurencyjnymi materiałami dlo nowoczesnych tarcz hamulcowych ze względu na ich wysoką wytrzymałość właściwą, wysoką przewodność cieplną i odporność na zużycie. Odpowiednio zaprojektowana gradientowa struktura Al/Al_2O_3 i Al/SiC może pomóc w zmniejszeniu termicznych naprężeń resztkowych powstających w procesie wytwarzania i skutecznie rozpraszać ciepło generowane podczas hamowania. Wybór dwóch alternatywnych cząstek ceramicznych (Al_2O_3 vs. SiC) do wzmocnienia osnowy ze stopu AlSi12 został zainspirowany podobnymi badaniami przeprowadzonymi w laboratoriach badawczych producentów samochodów (np. CR FIAT i Audi).

W niniejszej pracy stopniowane (lub warstwowe) kompozyty gradientowe (FGM) $AlSi12+vAl_2O_3$ i AlSi12+vSiC, gdzie v = 10, 20, 30 % obj., zostały przygotowane przy użyciu metody metalurgii proszków. Mieszaniny proszków AlSi12, Al_2O_3 i SiC użyte do uzyskania warstw kompozytowych i FGM przygotowano w planetarnym młynie kulowym. Jako techniki konsolidacji proszków zastosowano prasowanie na gorąco (HP) i spiekanie plazmowo-iskrowe (SPS). Charakterystykę mikrostrukturalną przeprowadzono za pomocą skaningowej mikroskopii elektronowej (SEM) i rentgenowskiej mikrotomografii komputerowej (micro–XCT). Przewodność cieplna warstw kompozytowych i FGM została wyznaczona przy użyciu techniki błysku laserowego w zakresie temperatur, który odpowiada warunkom pracy tarczy hamulcowej (od temperatury pokojowej RT do 300°C–500°C). Współczynnik rozszerzalności cieplnej (CTE) został wyznaczony w ramach studium przypadku dla kompozytów AlSi12+vSiC za pomocą badań dylatometrycznych w zakresie temperatur od RT do 500°C. Termiczne naprężenia resztkowe zmierzono metodą dyfrakcji neutronów. Dodatkowo przeprowadzono testy liniowego zużycia ściernego w urządzeniu Tabera w celu oceny właściwości tribologicznych kompozytów $AlSi12+vAl_2O_3$ i AlSi12+vSiC oraz porównania ich z żeliwem szarym, standardowym materiałem stosowanym w seryjnych tarczach hamulcowych.

Optymalizacja parametrów procesów mieszania i konsolidacji proszków pozwoliła na uzyskanie warstw kompozytowych i kompozytów gradientowych o wysokiej gęstości względnej. Ogólnie mówiąc, próbki wytworzone metodą HP były mniej porowate niż próbki SPS, a kompozyty $AlSi12+vAl_2O_3$ były mniej porowate niż kompozyty AlSi12+vSiC. Pomiary przewodności cieplnej wykazały, że kompozyty bez gradientu składu chemicznego wykazywały

niższą przewodność wraz ze wzrostem zawartości ceramiki zarówno dla układu AlSi12+vAl$_2$O$_3$, jak i AlSi12+vSiC. W przypadku kompozytów AlSi12+vAl$_2$O$_3$, porowatość i międzyfazowy opór cieplny zostały zidentyfikowane jako kluczowe czynniki zmniejszające przewodność cieplną. W przypadku kompozytów AlSi12+vSiC, tworzenie się cienkich warstw tlenków (Al$_2$O$_3$) i międzyfazowy opór cieplny były głównymi czynnikami przyczyniającymi się do redukcji przewodności cieplnej. Kompozyty gradientowe wykazywały w przybliżeniu stałą przewodność cieplną w badanych zakresach temperatur, osiągając wartość co najmniej dwukrotnie wyższą niż konwencjonalne żeliwo szare, co czyni je obiecującymi materiałami do zastosowania w tarczach hamulcowych.

W symulacjach numerycznych wykorzystano metodę elementów skończonych (MES), przy czym siatki elementów zbudowano na bazie obrazów z mikrotomografii komputerowej (micro–XCT), reprezentujących rzeczywistą mikrostrukturę, w tym defekty, takie jak pory. W modelach MES przewodności cieplnej uwzględniono przewodnictwo cieplne na granicach faz metal–ceramika. Wyniki symulacji numerycznych przewodności cieplnej wykazały doskonałą zgodność z danymi eksperymentalnymi, z błędami względnymi w zakresie od 4% do 6%. Z kolei modele termicznych naprężeń resztkowych wykorzystujące obrazy micro–XCT przy konstruowaniu siatek elementów skończonych pozwoliły oszacować naprężenia resztkowe w wytworzonych materiałach z dużą dokładnością – odchylenie od pomiarów wykonanych za pomocą dyfrakcji neutronów było mniejsze niż 5%. Stwierdzono, że termiczne naprężenia resztkowe są niższe w kompozytach gradientowych w porównaniu z kompozytami bez gradientu, co potwierdziły pomiary za pomocą dyfrakcji neutronów.

Eksperymenty dylatometryczne wykazały, że współczynnik rozszerzalności cieplnej (CTE) w kierunku równoległym do kierunku prasowania kompozytów gradientowych był znacznie niższy niż w kierunku prostopadłym do kierunku prasowania. Ogólnie rzecz biorąc, kompozyty gradientowe wykazały korzystny współczynnik CTE, około 32% niższy niż w przypadku osnowy ze stopu aluminium AlSi12, co wskazuje na zwiększoną stabilność termiczną i przydatność do zastosowań wymagających minimalnych zmian wymiarów w zmiennych warunkach temperaturowych.

W niniejszej rozprawie zbadano właściwości termiczne, termiczne naprężenia resztkowe powstające w procesie wytwarzania i właściwości tribologiczne warstwowych kompozytów gradientowych na osnowie ze stopu AlSi12 wzmocnionych cząstkami Al$_2$O$_3$ i SiC, łącząc metody eksperymentalne i numeryczne. Wyniki badań podkreślają potencjał funkcjonalnych opracowanych kompozytów gradientowych jako wysokowydajnych materiałów dla samochodowych tarcz hamulcowych, wykazujących doskonałą przewodność cieplną, zmniejszone naprężenia resztkowe i zwiększoną stabilność termiczną. Zgodność wyników eksperymentalnych z wynikami symulacji numerycznych potwierdza skuteczność zaproponowanych modeli, co może być pomocne w dalszych badaniach i zastosowaniu kompozytów gradientowych w warunkach przemysłowych.

Acknowledgements

I would like to express my profound gratitude to my supervisor, Prof. dr. hab. inż. Michał Basista, and my auxiliary supervisor, Dr. inż. Witold Węglewski, for their constant support throughout my academic journey. I deeply appreciate their immense dedication, and guidance which have been essential in shaping and guiding the preparation of my dissertation.

I would like to express my sincere gratitude to Dr. inż. Kamil Bochenek, for whose experimental support and insightful discussions I could always count on throughout my study.

I extend my sincere gratitude to Dipl.–Ing. Thomas Hutsch of Fraunhofer IFAM Dresden, Germany, for his invaluable guidance during my research stay.

I gratefully acknowledge Jördis Rosc and Roland Brunner from Materials Center Leoben (Austria) for performing the micro–XCT experiments.

Finally, I would like to thank my wife, Averil, and my son, Aven, for standing by me and supporting me throughout my PhD journey.

Table of contents

List of symbols and acronyms

|	
Volume fraction of matrix	V_m
Volume fraction of ceramic reinforcement	V_c
Thermal conductivity of matrix	λ_m
Thermal conductivity of ceramic reinforcement	λ_c
Effective thermal conductivity	λ_{eff}
Shear modulus of matrix	G_m
Shear modulus of ceramic reinforcement	G_c
Thickness of graded sample	t_{eff}
Functionally Graded Material	FGM
Metal Matrix Composites	MMC
Aluminum Metal Matrix Composite	AMMC
Grey Cast Iron	GCI
Thermal Conductivity	TC
Coefficient of Thermal Expansion	CTE
Thermal Residual Stresses	TRS
Powder Metallurgy	PM
Hot Pressing	HP
Spark Plasma Sintering	SPS
Scanning Electron Microscopy	SEM
Field Emission Scanning Electron Microscopy	FESEM
X–ray Diffraction	XRD
Energy–Dispersive X–ray spectroscopy	EDX
Neutron Diffraction	ND
Interfacial Thermal Resistance	ITR
Paul Scherrer Institute	PSI
Institute of Fundamental Technological Research	IPPT
Fraunhofer Institute for Manufacturing Technology and Advanced Materials in Dresden	IFAM
Material Center Leoben	MCL

INTRODUCTION

Aluminum Metal Matrix Composites – State of the art

Remarkable advancements in performance have already been achieved within composite materials engineering, particularly in metal matrix composites (MMCs). MMCs have been used extensively, revolutionizing industries of automotive, aerospace, and construction sectors. MMCs typically consist of a metal as matrix (Al, Cu, Ni, Mg, Fe, Ti, etc) and a ceramic reinforcement (SiC, Al_2O_3, TiC, B_4C, WC, TiB_2, etc) [1,2]. The selection of base metal and ceramic reinforcement materials depends on their compatibility and desired properties based on the intended application. The significant differences in physical, mechanical, thermal, and electrical properties between the metallic and the ceramic phases make the MMCs highly customizable. Among various metal matrices, Al–based MMCs have attracted more attention for their wide engineering applications due to their properties of formability, good ductility, light weight, and abundance [3]. When Al alloys are reinforced with ceramics particulates such as SiC, Al_2O_3, B_4C, and TiC they exhibit enhanced mechanical properties, good corrosion resistance and high specific strength [1,4,5]. However, improvements in thermal conductivity are not always realized and depend on several factors, including the composition, distribution of the ceramic phase, porosity levels, and the elimination of interfacial thermal resistance [6,7]. In fact, reinforcement with ceramics does not necessarily enhance thermal conductivity; for instance, in SiC–reinforced aluminum matrix composites, the thermal conductivity tends to decrease as the volumetric content of SiC increases [8]. Additionally, researchers have found that the inclusion of ceramics as reinforcement materials, have proved to be an effective way to increase the wear resistance of the Al matrix, strong bonding at the metal–ceramic interface, and improved fracture toughness [9]. These properties are influenced by the type and size of the reinforcement, as well as the interfacial bonding between the reinforcement and the matrix material [10]. Therefore, in recent decades, Al–based MMCs have attracted attention in the field of engineering.

In aluminum metal matrix composites (AMMCs), aluminum oxide (Al_2O_3) and silicon carbide (SiC) are the most used reinforcements [11]. The addition of SiC to aluminum and its alloys improves tensile strength, hardness, and wear resistance [12], whereas Al_2O_3 contributes primarily to improved compressive strength and wear resistance. AMMCs reinforced with Al_2O_3 or SiC possesses excellent thermal conductivity and a relatively low thermal expansion coefficient (CTE), making them suitable for thermal management applications [13]. They are also extensively used in the automobile sector due to their high elastic modulus, resistance to wear, and exceptional specific strength [14,15]. Nevertheless, the inherent characteristics of AMMCs did not allow them to be tailored for particular functions and applications. The concept of "Functionally Graded Materials" (FGMs, also known as "gradient materials") was introduced with

the idea of gradual changes in material properties at preferred positions. This allows FGMs to demonstrate superior functional performance in comparison with conventional composites. The concept of FGM was first introduced by Japanese researchers who conceived graded materials as a new concept in the 1980s to meet the challenges of very high temperature environment and to minimize thermal residual stress (TRS) concentrations [16]. Later, studies have shown that TRS can be drastically reduced by using FGM [17,18]. The variation of material properties in FGMs is frequently modeled using power-law function [19] and exponential function [20]. Literature pertaining to FGMs, in the material constituents [18], manufacturing methods [19], has increased significantly over the past three decades. This growth is attributable to the need to understand the mechanics and architecture of FGMs, given the wide material variations and applications of FGMs, such as in the automobile, defense, medical, aerospace, optoelectronics, and other industries [20]. Although, the concept of FGMs appears straightforward, realizing their practical implementation poses significant technological and scientific challenges for material designers and manufacturers. Manufacturing, characterizing and modeling such FGMs is challenging due to their complex microstructure and morphology.

Presently, the automotive industry is seeking new structural materials with high strength, rigid, lightweight, enhanced wear resistance and increased thermal conductivity. A structural component working under the conditions of extreme friction, corrosion, increased temperature, and thermal shocks is the brake disc. Automotive brake discs require materials with a high strength core which can effectively dissipate the heat and resist the wear on the outer surfaces. Problems concerning heat dissipation in brake disc system are presented schematically in **Fig.1.1**. Due to the intensive heat generation during the braking process, cast irons are commonly used. While cast irons offer excellent thermal conductivity, their relatively high density ($\approx 7.150 \, g/cm^3$) often results in increased component weight, limiting their suitability for weight-sensitive applications. Currently, metal-ceramic composites are used to reduce the weight of the brake disc system. However, material cost remains a critical limiting factor, and the incompatibility in thermal expansion between metal and ceramic compounds hinders heat transfer efficiency at their interface.

11
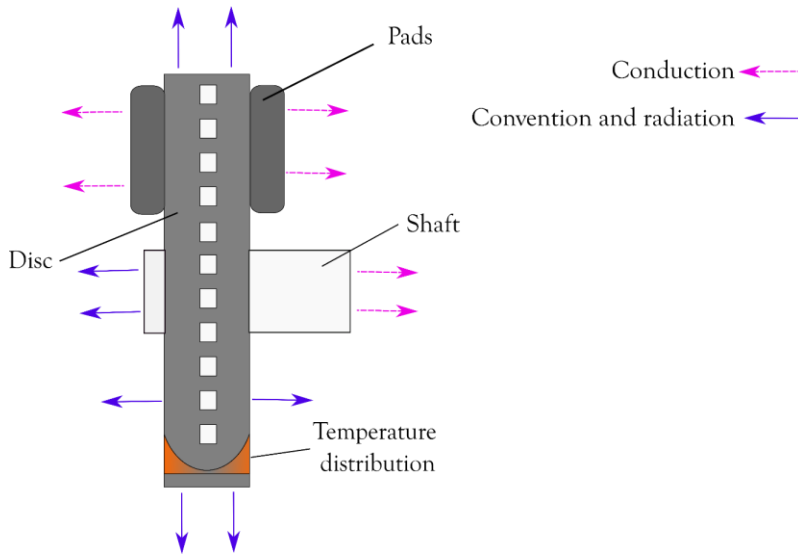
Fig.1.1 Hear transfer system in disc brake system.

In AMMCs, the Al matrix shows superior mechanical and thermal conductivity, while the ceramic reinforcement offers excellent wear resistance. In automotive brake disc application, it is essential to take advantage of the resulting in material properties from the properties of each of its constituents. Moreover, thermal behavior of such composites is essential to their functionality where heat must be dissipated as quickly as possible at surfaces exposed in high temperature environments and offer excellent wear resistance at the surfaces clamped to the brake pads. FGM composed of Al and ceramic perform exceptionally as they feature an Al core for strength and quick heat dispersal, with ceramic on the outer surfaces to resist wear and high temperatures. The macroscopic thermal conductivity of Al–ceramic graded materials is determined by the properties and volume fractions of their components and the gradation across layers; however, microscale factors such as particle size, dispersion, and porosity play a crucial role in defining the composite's overall performance. Porosity significantly lowers the thermal conductivity of the composite, making high pore concentrations undesirable for most structural applications due to degradation of potential thermal performance. Additionally, interfacial thermal resistance remains a key barrier to achieving improved thermal conductivity in aluminum matrix composites. The mechanism of heat transfer occurring at the metal–ceramic interface can have a significant effect on the thermal conductivity of a composite. Accordingly, the research presented in this thesis aimed to study the thermal conductivity of graded composites and explore the microstructural parameters responsible for the physical behaviors observed during fabrication and experiments, aiming to tailor the strength and thermal properties of newly developed FGMs.

1.1. Manufacturing routes for Functionally Graded Materials (FGM)

FGMs can be classified based on their cross section and the spatial distribution of their constituents. According to the cross–sectional characteristics, FGMs are divided into two types: thin FGMs and bulk FGMs. Thin FGMs are typically fabricated using techniques such as plasma spraying, vapor deposition, and other coating methods. In contrast, bulk FGMs are produced through methods like centrifugal casting, powder metallurgy, etc. Depending on the spatial distribution of the reinforcement, FGMs can also be categorized as: (a) continuous graded materials, where the composition varies smoothly across the volume, and (b) discrete (or stepwise graded) materials, where changes occur in distinct layers or steps. **Fig.1.2 (a)** shows a continuous FGM in which the change in composition and/or microstructure occurs continuously with position, while **Fig.1.2 (b)** is a schematic representation of a layered FGM, in which the material microstructure changes in a stepwise manner to form distinct layers.
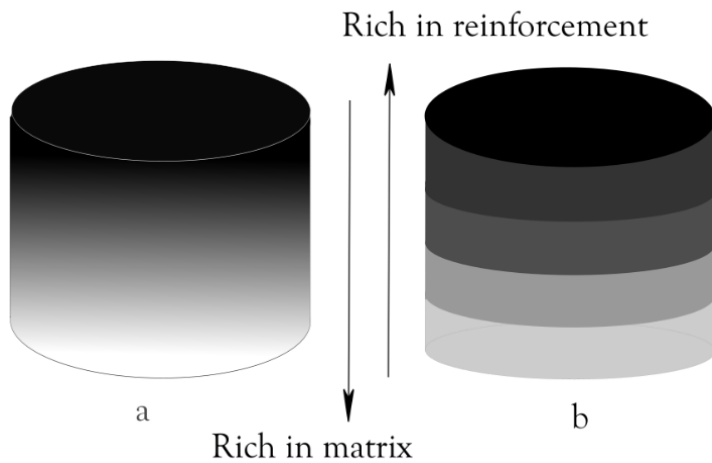
Fig.1.2 Illustration of (a) continuous FGM and (b) layered (stepwise) FGM.

The choice of processing route is of paramount importance in the manufacture of FGMs, as it has a direct impact on ability to precisely control the composition, microstructure, and ultimately, the graded properties of the material. Although friction stir processing, centrifugal casting, and powder metallurgy (PM) are the main methods for producing graded AMMCs, PM represents one of the most effective and reliable techniques for fabricating AMMC FGMs. As depicted in **Fig.1.3**, there is a range of techniques associated with PM, including various methods of stacking, compacting, and sintering. PM can accommodate a gradation step of MMCs, with easy control over the composition, microstructure, and form

[21,22]. Using PM it is possible to achieve graded properties depending on the application by optimizing the composition, number of gradation steps etc. For instance, one end of the component will contain a higher ceramic reinforcement content, thereby enhancing its wear resistance. The other end will consist primarily of an aluminum alloy, ensuring high toughness and effective heat dissipation [23]. Two FGMs produced in [24] involved Al reinforced with varying wt.% of SiC in each layer. The four-layered Al+wSiC (w=0, 3, 7, 10 wt.%) composite demonstrated enhanced metallographic homogeneity and superior mechanical properties when compared to the five-layered Al+wSiC (w=10, 20, 30, 40, 50 wt.%) composite.
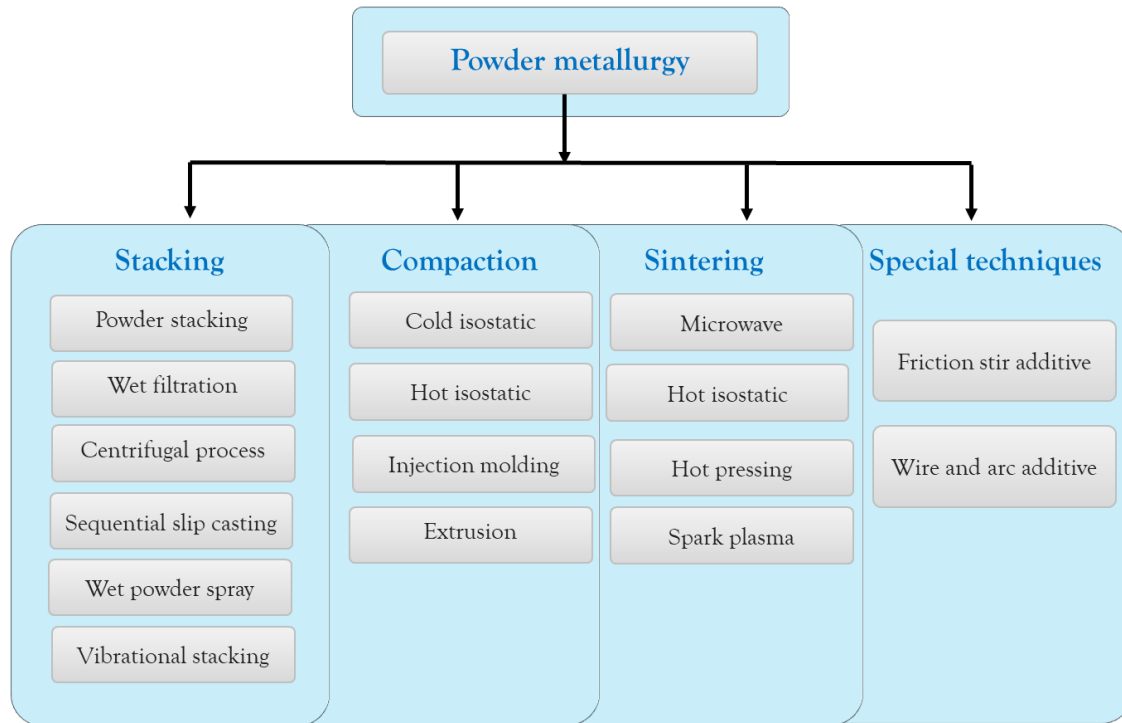
Fig.1.3 Classification diagram of powder metallurgy techniques.

PM techniques have proven to be highly successful in mitigating undesirable chemical reactions between the reinforcement and matrix materials, while ensuring a homogeneous distribution of the reinforcing phase [21]. Among different sintering techniques listed in **Fig.1.3**. The ability of spark plasma sintering (SPS), to achieve sufficient microstructural control, coupled with its rapid thermal cycles and lower processing temperatures, makes it an ideal technique for fabricating FGMs, in comparison to e.g., conventional sintering via hot pressing (HP). The sintering setups of SPS and HP are illustrated in **Fig.1.4**. SPS has emerged as the preferred route for consolidation and sintering of Al powders. This process enables the achievement of almost full material densification while preserving a fine-grained structure. Maintaining a fine-grained microstructure during processing enhances mechanical strength and bulids a strong bonding between reinforcement and matrix, resulting in fully dense composites [22]. The rapid heating

14

and short sintering cycles in SPS, combined with applied pressure, uniquely minimize grain growth while maximizing densification. The most significant parameters influencing the diffusion mechanics of sintering include dwell duration, heating rate, temperature, and pressure variations [23–26]. Proper control of the sintering temperature, heating rate and related process parameters is essential to achieve the desired microstructure and properties in the final product. For instance, in [23], Al/Al_2O_3 composites were prepared at two distinct sintering temperatures (500 °C and 550 °C) for a constant sintering time of 45 minutes. The findings indicated that as the reinforcement weight fraction increased, the relative density decreased, while the wear resistance and hardness increased. Results also showed that the addition of Al_2O_3 decreased the wear rate by 40% [23]. In a study on Al/SiC particulate composites [24], by extending the sintering time from 1–2 min in friction powder sintering (FPS), the relative packing density has increased by 12.35%, and the thermal conductivity has increased about 67% [24]. In another SPS process conducted at 580 °C and 600 °C, the fabricated composites achieved a close to full density of 97–99%, and microstructural analysis revealed no significant differences between those reinforced with SiC particles at either temperature [27]. Therefore, SPS has become a preferred method among many researchers for producing high–quality AMMCs.

In this work, for the comparative analysis, two PM techniques, namely hot pressing (HP) and spark plasma sintering (SPS) are considered. These techniques have proven favorable for the homogeneous distribution of ceramic particles in the Al matrix, enabling a seamless transition between layers. Additionally, these techniques effectively restrict chemical reactions between the reinforcement and matrix materials and help achieve a fully dense material.
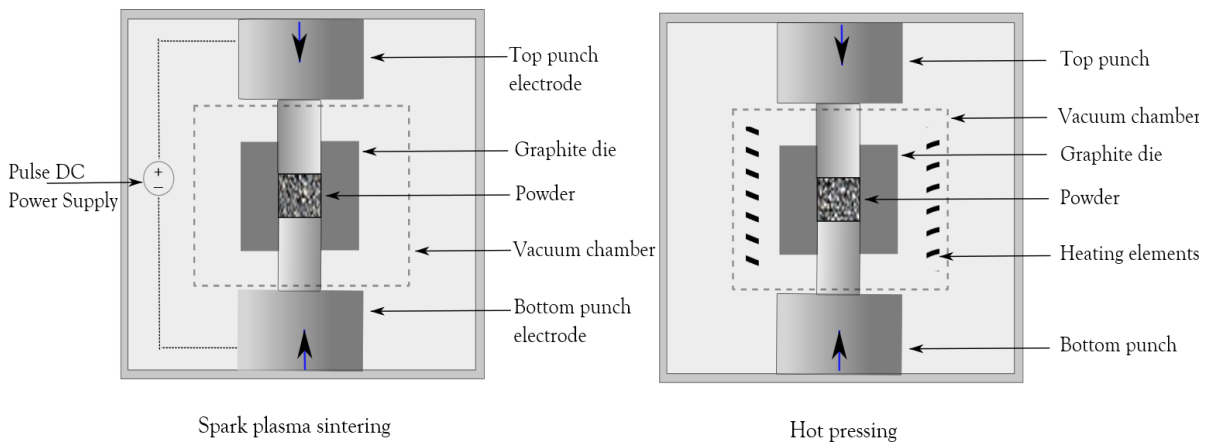
Fig.1.4 Schematic depiction of spark plasma sintering (SPS) and hot pressing (HP) setups.

15

1.2. Thermal residual stresses (TRS) in FGM

Significant stress in sintered components during the cooling process is attributed to the mismatch of the coefficients of thermal expansion (CTE) between the metal (e.g., Al) and the reinforcements (e.g., Al_2O_3 or SiC). A key characteristic of FGMs is that they can reduce thermal residual stress in the bulk material and stress singularities at material interfaces. To avoid the unexpected fracture of structural components under operating conditions, these stresses need to be assessed for the thermomechanical property gradient. Residual stresses are generally classified into macro- level and micro-level stresses, both of which may be present simultaneously within a material. Macro residual stresses (macro-RS) are due to misfit between different regions, caused e.g., by welding, shot peening, or non-uniform plastic deformation. These stresses exhibit variation over macroscopic distances that exceed the scale of the material's grain size and are detectable by destructive techniques (e.g., hole drilling) In Ref.[25] macroscopic residual stresses developed during cooling from the sintering temperature due to thermal expansion differences between regions of the graded Al/Al_2O_3 plate with varying aluminum content, are determined.

Residual microstresses, resulting from variations within the material's microstructure are categorized as micro (micro-RS) and sub-micro (submicro-RS) residual stresses Micro-RS operate at the grain size level, while submicro-RS are generated at the atomic scale within the grains (e.g., stress fields around dislocations). Micro-RS are misfit stresses generated by a mismatch in elastic constants or thermal expansion coefficients between individual grains in polycrystals or between different phases within a composite [26].

Fig.1.5 (a) shows the Moiré interference pattern highlighting displacements initiated by cutting a notch in this graded plate under macro-residual stress. The position where displacement measurements were taken is indicated by the white reference bar. **Fig.1.5 (b)** shows the cracking in the composite with an aluminum matrix and carbide particles, caused by residual microstresses generated during cooling after hot pressing at 650 °C with a heating rate of 20 °C/min [28].

Pores can affect the TRS distribution in the metal and ceramic phases of a composite. In Ref.[29] the average TRS were measured for the $AlSi12/Al_2O_3$ composites fabricated by hot pressed and squeeze cast . It is found that the average TRS values in both phases (compressive in the ceramic phase and tensile in the AlSi12 matrix.) were slightly lower than the HP because of its higher porosity, which can partially accommodate the residual stresses.

(a)   (b)
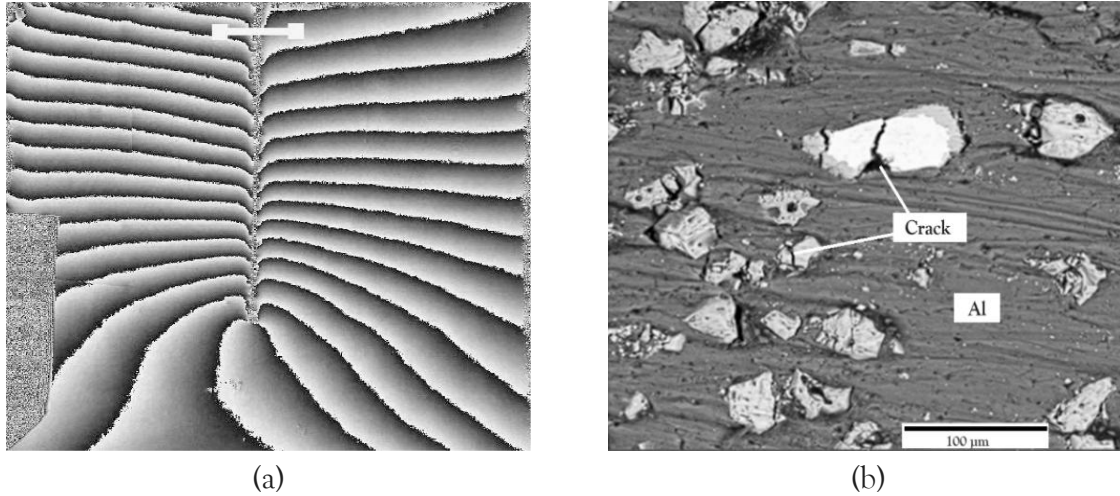
Fig.1.5 (a) Moire´ interference pattern revealing displacements generated by cutting a notch in a Al/Al$_2$O$_3$ graded plate with macro–RS [25]. This figure is reproduced with permission from Springer Nature. **(b)** Cracking patterns in the compressed specimens due to micro–RS in Al matrix and carbide particles [28]. This figure is reproduced with permission from Elsevier.

Residual stresses can change in sign and magnitude over distances comparable to the grain size. Such residual stresses can be high enough to cause fracture or local yielding on both microscopic and macroscopic scales, significantly affecting the performance of the component. Ignoring the presence of residual stresses in composite design can increase the risk of unexpected structural failure; therefore, their impact must be carefully evaluated. It is possible to minimize or eliminate the processing–induced residual stresses of a graded composite through properly designing the composition gradient and the number of layers. Therefore, one of the objectives of the research reported in this thesis was to investigate the thermal residual stress in graded composites and to study the actual effect of graded microstructure on the processing–induced thermal residual stresses. Well-designed graded structure of Al–matrix composites can reduce the process–induced thermal residual stresses (especially in the ceramic phase) without compromising thermal conductivity or strength of the composites.

Among the non–destructive techniques used to determine residual stresses, X–ray diffraction (XRD), synchrotron X–ray diffraction (SXRD), and neutron diffraction (ND) are the most popular. While X–ray diffractometers are standard equipment in materials research laboratories, SXRD and ND measurements require specialized facilities. In addition to diffraction methods, optical methods such as Raman spectroscopy (RS) and photoluminescence piezo spectroscopy (PLPS) are used to determine the TRS. Recent advances in residual stress measurement methods, both destructive and non–destructive, and their existing problems and difficulties are presented in [30]. **Table 1.1** lists the various non–destructive techniques used for measuring residual stresses and their specification, advantages and disadvantages. The non-destructive measurement of residual stress has significantly progressed with the advent of

17

specialized neutron and synchrotron X–ray diffraction instruments. The neutron diffraction method is more effective due to the high penetrating power of neutrons in most materials. These techniques are crucial for composites as they enable the assessment of stresses in each constituent phase of the composite material. Additionally, energy–dispersive methods, such as time–of–flight ND or energy dispersive synchrotron radiation diffraction, can capture the entire diffraction pattern avoiding any angular scanning and provide complete 3D map of the residual stresses within a specimen. Neutron diffraction, in particular, can well distinguish between all three types of residual stress and facilitates the rapid determination of stresses in various crystal families within the same phase.

Table 1.1 Residual stress measurement using non–destructive techniques based on the NPL Report, [31].

Technique	Material type	Resolution	Penetration	Advantages	Disadvantages
X–ray diffraction	Metal/ Ceramic	20 μm	<20 μm 50 μm–Al	• Versatile. • Widely available. • Moveable setups. • Macro and micro–RS.	• Standard measurements. • Lab–scale setups. • Minor samples.
Neutron diffraction	Metal/ Ceramic	≈1 mm	100 mm –Al	• First–rate penetration &Resolution. • 3D maps. • Macro and micro–RS.	• High–tech facility. • Lab–scale setups.
Synchrotron X–ray diffraction	Metal/ Ceramic	1 μm–100 μm	>500 μm	• Improved penetration. • Gradient evaluation. • Quick. • Macro and micro–RS.	• High–tech facility. • Lab–scale setups.
Ultrasonic	Metal/ Ceramic	0.5–150 mm	>100 mm	• Widely available. • Quick. • Low cost. • Moveable setups.	• Limited resolution. • Bulk measurements over ultrasonic whole volume.
Raman/PLPS	Plastic/ Ceramic	0.5 μm	< 1 μm (near surface)	• High resolution. • Portable.	• Limited to surface. • Limited range of materials.
Magnetic	Metal /Ferrom agnetic	0.1 mm–2 cm	200–300 μm	• Rapid. • Wide variety of magnetic materials. • Portable.	• Ferromagnetic materials only. • Signal manipulation required.

Building on the advantages of neutron diffraction and energy–dispersive methods in assessing residual stresses, analytical and numerical techniques offer alternative approaches for

predicting and understanding stress distribution in composite materials. Analytical methods, such as Eshelby's [32] and weight function [25]. Eshelby's methods assume that inclusions have an ellipsoidal shape and the matrix is isotropic and homogeneous. The weight function approach enables the calculation of residual stresses from observed displacements. Besides analytical methods, numerical approaches are widely used to estimate the residual stresses and the constitutive response of the AMMCs A simple finite element (FE) numerical model was utilized to analyze the distribution and magnitude of thermal residual stresses induced during fabrication in Al/SiC composites [33]. The results showed that minimal SiC content led to lower residual stress. In addition, the distribution of SiC particles in the matrix affects the amount and the gradient of internal stresses generated. In Ref. [29], the residual stresses in the ceramic (Al_2O_3) phase were experimentally measured via neutron diffraction and numerically simulated using a finite element model based on micro–XCT data, incorporating the actual microstructure of the composite. The model predictions for two different volume fractions of Al_2O_3 agree well with the ND measurements [29]. A 3D numerical model using cubic unit cell was used to simulate thermal residual stress for the Mg alloy reinforced with SiC particles with volume fraction of 12% fabricated by hot forging technology [34]. A multiscale model for predicting the macro–RS and micro–RS residual stresses in MMCs based on realistic 3D digital microstructure models showed good self–consistency and good accuracy [35]. These models are widely used to predict the stress and strain behavior of MMC materials. It is important to note that numerical models based on material microstructure accurately predict residual stresses for FGMs. Therefore, it is reasonable to use numerical models with FE meshes based on, for example, micro–XCT scans, which provide sufficient microstructural data to mimic the real material microstructure. Such an approach to FE modeling of TRS will be used in this dissertation.

1.3. Functionally graded Al–matrix composites reinforced with Al_2O_3 particles

Al_2O_3 (aluminum oxide or alumina) is known for its excellent hardness, good compressive strength, high melting point, good thermal stability, and wear resistance. When used as an reinforcement in AMMCs, alumina particles may significantly enhance the composite's wear resistance, hardness, and overall mechanical strength [36]. The size, shape, and distribution of the Al_2O_3 particles within the Al matrix play a key role in determining the thermal and mechanical properties of the composite The Al/Al_2O_3 composites produced with fine Al powder (3–4.5 μm average particle size) using the powder metallurgy technique exhibited higher relative density and elastic modulus values, as well as lower CTE values as compared to composites with coarser Al powder (10 μm average particle size). The elastic modulus was improved and the CTE was reduced with increasing Al_2O_3 content across all cases [37]. As reported in [38], the thermal conductivity of α–Al_2O_3 particulate–reinforced Al matrix

19

composites fabricated by conventional PM processes can be enhanced by adjusting the volume fraction and particle size of Al_2O_3. The use of fine Al_2O_3 particles enhances the hardness and wear resistance, as evidenced in [39]. The stir–cast Al matrix composites reinforced with Al_2O_3 and SiC demonstrated enhanced physical and mechanical properties, including a low CTE (4.6×10^{-6}/°C), ultimate tensile strength increased significantly by as much as 23.68% accompanied by high impact strength and hardness [40]. These characteristics make these composite materials suitable for use as lightweight materials in automobile components. The composites reinforced with SiC particles exhibited a lower wear rate compared to those reinforced with Al_2O_3 [40]. A comparison of thermal conductivity in $AlSi12/Al_2O_3$ composites produced through squeeze casting and hot pressing methods is discussed in [41]. Results revealed that squeeze–cast composites possess enhanced thermal conductivity, lower TRS, and reduced frictional wear in comparison to hot–pressed composites. The recent literature on these FGMs with their research outcomes are listed in **Table 1.2**.

1.4. Functionally graded Al–matrix composites reinforced with SiC particles

Silicon carbide (SiC) contains both carbon and silicon atoms and has high hardness, low thermal expansion, and good resistance to wear and corrosion. When used as a reinforcement it improves the density, tensile strength, hardness and wear resistance of AMMCs [12]. AMMCs reinforced with SiC particles are of great interest especially for the automotive and electronic components sector due to their excellent properties such as high fatigue strength and thermal conductivity (180–200W/mK). The thermal conductivity of Al/SiC composites is the critical property for applications requiring efficient heat dissipation.

The use of SiC particulates as a reinforcement in Al matrix presents certain challenges. Among the many challenges, grain growth in the matrix, interfacial reactions and defects at the phase boundries are particularly significant. Thermal conductivity measured by Xenon Flash Analysis (XFA) test showed that as the SiC content in the composite samples increased, the thermal conductivity decreased to 61.5 W/mK. This reduction was attributed to the growing number crystalline defects especially dislocations at the phase boundaries [36]. In composites produced by powder metallurgy, poor interfacial bonding may result from incomplete sintering and insufficient interfacial reactions. Conversely, excessive interfacial reactions at elevated temperatures between aluminum and silicon carbide may contribute to undesirable phase formation such as aluminum carbide (Al_4C_3). In the case of aluminum–silicon (AlSi) alloys and silicon carbide (SiC), the presence of oxygen can result in the formation of undesirable oxides such aluminum oxide (Al_2O_3) and /or silicon dioxide (SiO_2) [42,43]. There are several studies [44–49] on Al/SiC composites fabricated by powder metallurgy, showing the degradation of

overall thermal conductivity due to the formation of oxides and carbides between the interface of Al and SiC by an interfacial reaction.

These new phases can be formed at grain boundaries of metal matrix and reinforcing particles during processing of composites. These compounds are considered to be thermodynamically unstable making the composite more susceptible to degradation of its properties and negatively impact the material's performance despite the minor amount of new phases [50]. A higher content of oxides or carbides plausibly leads to a reduction in the overall thermal conductivity of the composite. The oxide film that forms around aluminum particles either at the Al–SiC interface and/or Al–Si during the sintering process is likely due to the presence of oxygen adsorbed onto the aluminum powder during its preparation. Although this oxide layer acts as a barrier, hindering the formation of metal–metal bonds, it also serves to protect the aluminum from further oxidation. At lower temperatures, the alumina formed is typically amorphous, with a thickness ranging from 0.5 to 5 nm. When this critical thickness is exceeded due to continued oxidation, the layer becomes unstable and transforms into the crystalline γ–Al_2O_3 phase. This transition from amorphous to crystalline γ–Al_2O_3 generally occurs when the temperature exceeds 400 °C. In typical sintering techniques such as HP and SPS, the process is conducted under a vacuum atmosphere; however, this environment does not fully reduce or eliminate the Al_2O_3 layer, which is confirmed by the obtained results of the investigations presented in this thesis. This result proves findings reported in earlier investigations using SPS of Al–SiC composites with low SiC contents [28] and also in high SiC content [42].

Additionally, Al/SiC composites fabricated by powder metallurgy have shown a degradation in overall thermal conductivity due to the formation of Al_4C_3 at the interface between Al in the liquid or semiliquid form and SiC through an interfacial reaction, which increases interfacial resistance [43]. The reaction governing Al_4C_3 formation is expressed as:

$4Al + 3SiC \leftrightarrows Al_4C_3 + 3Si$.
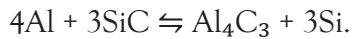
However, this reaction shows the positive free Gibbs energy change of this reaction over 200 °C. Additional reaction between Al and Si on SiC particles can take place with a negative free Gibbs energy change at 700 °C, according to the following reaction [51]:

$2Al + SiO_2 + CO \leftrightarrows Al_2O_3 + Si + C$
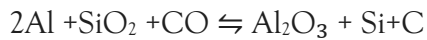
The above reaction causes a simultaneous reduction in the amount of Al and an increase in γ–Al_2O_3. The presence of carbon leads to significant consumption of Al and the formation of undesirable Al_4C_3 during densification. This reaction is accompanied by the formation of γ–Al_2O_3, resulting from the reduction of Si on SiC particles by Al in the presence of CO.

To mitigate the negative effects of these interfacial reactions, various processing techniques have been explored. For instance, vacuum hot pressing (VHP) offers a viable alternative, yielding superior thermal performance due to better control over interfacial reactions compared to other methods like liquid infiltration and spark plasma sintering (SPS) [48]. Additionally, the use of process control agents (PCA) during milling enhances the interfacial bonding between Al and SiC particles, thereby improving thermal conductivity [52]. Moreover, sintering parameters, such as temperature and holding time, significantly affect composite properties; shorter holding times lead to poor thermal conductivity due to the formation of Al_4C_3 and pores, whereas prolonged sintering introduces a SiO_2 layer that increases interfacial thermal resistance [53]. Studies have also shown that maintaining a eutectic composition of 13 wt.% Si effectively inhibits Al_4C_3 formation, improving thermal properties [43]. High–frequency induction sintering (HFIS) has been found to improve composite density and hardness while preventing harmful Al_4C_3 formation [54]. Furthermore, explosive compaction has emerged as a rapid densification technique that minimizes Al_4C_3 formation, preserving thermal conductivity [53]. Increasing the sintering temperature reduces the volume fraction of Al_4C_3 and Si phases, further enhancing thermal conductivity [55]. Post–oxidation treatment is another effective approach to removing residual carbon, preventing Al_4C_3 formation during aluminum infiltration, and increasing the thermal conductivity of treated samples by approximately 6.5% compared to untreated ones [56]. During the hot forging of Al/SiC composites, forging at temperatures below aluminum's melting point resulted in porous structures, leading to reduced thermal conductivity. Conversely, forging above the melting point yielded fully densified composites with significantly enhanced thermal conductivity. An interfacial reaction between the aluminum matrix and SiC particles led to the formation of an Al_4C_3 reaction layer, whose thickness increased progressively with rising forging temperatures [57]. However, in the unique processing of Al/SiC composites in continuous solid–liquid co–existent state by SPS, the measured thermal conductivity was higher with increasing the SiC content and the highest value (252 W/mK) was obtained for Al/50 vol.% SiC composite [50]. The AlSi12 matrix composite reinforced with 70 vol.% SiC particles of two sizes showed that the composite was free from interfacial reaction compounds. The SiC acted as heterogeneous nucleation sites for the Si phases in the matrix and the composite had a better thermal conductance than the unreinforced matrix [58].

The particle size of SiC in AMMCs is a crucial factor influencing their thermal conductivity. Smaller particles tend to provide different thermal properties compared to larger particles due to their impact on microstructure and interfacial characteristics. The Al/SiC composites with 50 vol.% SiC fabricated for the electronic packaging application showed that coarse SiC particles result in higher CTE and higher thermal conductivity, while fine SiC particles reduce CTE and TC [59].

22

In [60], SiC particulate preforms with significant different average particle sizes (170 μm and 16 μm) were infiltrated with liquid aluminum. The study demonstrated that the overall coefficient of thermal expansion (CTE) is mainly influenced by the composite's compactness, or total particle volume fraction, while factors such as average particle size and particle size distribution have minimal impact on the overall CTE. In another study [61], smaller SiC particles were found to increase interfacial thermal resistance due to a higher interfacial area per unit volume, leading to a significant reduction in the overall thermal conductivity of the composite. Therefore, to enhance the thermal conductivity of Al/SiC composites with interfacial thermal barriers, the use of larger reinforcement particle sizes is recommended [47], as they reduce the extent of interfacial resistance. Additionally, the introduction of an appropriate amount of cerium into Al/SiC composites fabricated via a pressureless infiltration process could effectively improve the interfacial conditions, thereby improving the thermal conductivity of the Al/SiC composites [62]. The sintering process and the resulting porosity are critical factors influencing the thermal conductivity of Al/SiC composites. Sintering temperature, time, and pressure affect the density and microstructure of the composites, which in turn affect the thermal conductivity. The samples of Al/SiC composites with volume fraction of ceramic reinforcement above 50%, prepared by vacuum pressure infiltration, showed that even small variations in porosity ranging from 2.5% to 4.5% can substantially reduce the thermal conductivity of SiC–dense composites [63]. The presence of roughly 13% residual porosity significantly reduces the thermal conductivity of AlSi12/SiC composites produced via constant pressure infiltration [64]. The effects of varying SiC particle concentrations and the number of layers on Al2024/SiC FGMs processed by powder metallurgy were investigated in [65]. The authors reported significant improvements in bending strength, microhardness, and wear behavior. Additionally, they found that the rate of intermetallic formation affected the porosity [57]. The wear behavior of A356/SiC composites was compared with that of conventional grey cast iron (GCI), using a brake shoe lining material as the counterpart pin to represent an automotive friction material. [66].

Table 1.2 presents a concise literature review of the last decade of research on Al/SiC and Al/Al_2O_3 FGM systems, their processing parameters using powder metallurgy, and characterization of properties. The researchers have rigorously investigated the mechanical properties (e.g., hardness, fracture toughness, compression, tensile, and flexural strengths) and tribological properties of different compositions and numbers of layers in graded Al/SiC and Al/Al_2O_3 composites. The effect of microstructure of composite layers on the thermal properties and thermal residual stresses of these FGMs has received little attention. Therefore, in this thesis, the influence of microstructure on thermal conductivity and TRS in stepwise graded $AlSi12/Al_2O_3$ and AlSi12/SiC composites fabricated using HP and SPS will be investigated and compared with the results obtained for ungraded $AlSi12/Al_2O_3$ and AlSi12/SiC composites.

Table 1.2 Literature survey of the Al/SiC and Al/Al₂O₃ FGM systems obtained by powder metallurgy, with their sintering techniques and properties investigated.

Material	Sintering condition	Properties	Outcome	Ref.
Al+wSiC (w = 0, 3, 7, 10 wt.%)	Conventional sintering for 1 h at 580 °C in inert atmosphere furnace.	• Hardness • Fracture toughness • Tensile test • Wear	• Obtained uniform material distribution and absence of interfacial cracks. • The hardness and toughness of the FGM represented an improvement over those of pure Al. The hardness of the composite increased by increasing the SiC wt.%, and wear volume loss and coefficient of friction were lowered.	[67] [68]
Al2024+vSiC (v=30, 40, 50, 60 vol.%)	Hot pressed at 560 °C and 500 MPa in an argon atmosphere.	• Microhardness • Bending strength	• A significant improvement in the mechanical properties of the composites was observed, largely driven by the increase in microhardness and the presence of intermetallic formations.	[69]
Al+vSiC (v=2.5, 5, 7.5, 10 vol.%)	Conventional sintering for 5 h at 630 °C in a vacuum condition and cooled at room temperature.	Hardness	• Smooth transitions of microstructure between adjacent layers. • SiC addition improved Al/SiC crystallite size. • Al+10% vol. SiC yielded the best hardness result. By incorporating non-conductive SiC, the Al-based graded material's corrosion resistance can be improved due to SiC's inherent properties.	[70]
Al7075+wSiC (w= 0, 15/ 15, 20/ 10, 20/ 10, 15, 20 wt.%)	Conventional sintering at 530 °C for two hours in an inert gas furnace.	Hardness	• The mechanical properties mainly depended on the type of interfacial bonding between the layers, micro-cracks, pores, and SiC agglomerations.	[71]
Al+vSiC (v=10, 20, 30, 40 vol.%)	Conventional sintering at 550 °C for 3.5 h.	• Microhardness • Flexural strength • Thermal fatigue • Thermal shock resistance	• Microhardness changes at the interfaces matched the analytically predicted stress. • The effective flexural strength was enhanced by roughly 41%.	[72]
Al6061+wSiC (w=0, 5, 10, 15 wt.%)	Sintered for 1 h, and 2 h at 530 °C, within a controlled atmosphere furnace.	• Hardness • Fracture toughness • Impact strength	• Extended sintering, by regulating grain growth, detrimentally impacted the mechanical properties. • The best hardness and impact strength were found in the fourth layer of the FGM (15 wt.% SiC) due to better load sharing and restricted dislocation movement. • The absence of crack formation among and within the layers.	[73] [74]
Al+vSiC (v=0, 10, 20 /0, 20, 40 vol%)	Conventional sintering for 40 min at 580 °C. (liquid phase)	Ballistic test	The investigated FGMs didn't offer good ballistic protection in any of the thicknesses or compositions tested. This was shown by large cracks and punched-out sections found in the samples.	[75]
Al+vSiC (v=0, 2.5, 5 ,7 vol.%)	Conventional sintering for 1 h at 600 °C.	• Hardness • Compression	• The compressive strength is depends on even distribution, good mixing, the amount of reinforcement, and grain size. An increase in reinforcement content led to higher hardness.	[5]
Al2124+vSiC (v=10, 20, 30, 40 vol.%) –continuous gradient	Vibration followed by preheating in furnace to 500 °C, pressed at a pressure of 1.5 GPa.	• Hardness • Fracture toughness	• The SiC content altered from a layered structure to a continuous gradient along the sample due to the vibration. Compared to metal matrix composites, FGMs showed improved toughness.	[76]
Al6061/SiC (SiC 0–40 vol.%)	Hot pressing at 600 °C under 100 MPa for	• Compression	• FGMs exhibited higher storage moduli and damping capacities than MMCs.	[77] [78]

Continuous gradient	90 min in a vacuum and argon atmosphere.	• Damping capacity	• Compression of the FGM showed strong dependence on the varying composition through its thickness. • Increasing the testing temperature reduced the strength, whereas higher compositional gradients enhanced yield and ultimate compressive strengths.	
Al2024+vSiC (v=15, 25, 35, 45, 55 vol.%)	Hot pressing at 550 °C with 400 MPa for 1 h, followed by heat treatment for 2 h at three temperatures of 530, 545, and 560 °C.	• Microhardness • Fracture toughness	• The sample treated at 545 °C exhibited the highest microhardness and flexural strength, while further increases in the treatment temperature led to decreases in both properties.	[79]
AA7075+8% graphite+2% SiC	Conventional sintering 120 min at 620 °C and microwave sintering 30 at 500 °C.	• Tensile • Compression • Hardness • Ductility	• The microwave-sintered composite exhibited a fracture strain of 7.98%, highlighting the advantages of microwave sintering over conventional methods.	[80]
Al /SiC/MgO$_2$ (Four layers)	Conventional sintering for 40, 250, 260 min at 480, 500, 520 °C respectively.	• Hardness • Compression • Wear	• FGMs exhibited superior compressive strength, microhardness, and macro hardness compared to composite materials. • Tribological study showed that the second layer of the FGM, composed of Al/10 vol.% SiC, provided the best wear resistance.	[81]
AA5083+wAl$_2$O$_3$ (w =10, 20, 30, 40, 50, 60 wt%) 3, 4 and 6 layers	Conventional sintering for 1 h at 750 °C in a protective argon gas environment.	• Hardness • Corrosion tests	• Hardness values increased as the amount of Al$_2$O$_3$ reinforcement in the FGM layers increases. • Layers with higher Al$_2$O$_3$ reinforcement experienced greater corrosion.	[82]
Al+vAl$_2$O$_3$ (v =0, 5, 10, 15 vol.%) (four-layer FGM)	Conventional sintering for 3 h at 600 °C using 2–step cycle.	Hardness	• The ceramic particles were evenly spread in the metal, and the layers changed smoothly with clear boundaries between them. • Hardness values increased as the amount of Al$_2$O$_3$ reinforcement in the FGM layers increases.	[83]
Al+vAl$_2$O$_3$ (v =0, 10, 20, 30, 40 vol.%) (five–layer FGM)	SPS at 1050, 1400 and 1450 °C under 40 MPa for 10 min, heating at ~100 °C and cooling at ~130 °C.	• Flexural strength • Fracture toughness	• The maximum bending strength of was obtained in sample sintered at the highest temperature. • At the lowest sintering temperature, the sample's fracture surface had many cracks and voids. • Sintering at 1400 °C prevented grains from growing and created weak boundaries, leading to cracks between grains.	[84]

1.5. Thermal modeling of functionally graded materials

Analytical and numerical models are often used as an alternative or support to experimental measurements for advanced composite materials. In the case of AMMCs, such approaches have been widely used to determine their effective thermal properties. Among the most commonly applied analytical models for predicting effective thermal conductivity are the Maxwell [85], Hasselman–Johnson [86] Bruggeman [87], Lewis–Nielsen [88] and Hashin–Shtrikman [89]. Numerical approaches include the representative volume element (RVE)–based finite element (FE) homogenization method [90,91], which accounts for factors such as inclusion anisotropy, distribution, interfacial thermal conductance, and geometry. Popular numerical models, which predict the effective thermal conductivity are comprehensively reviewed in [92].

For evaluating effective thermal expansion, analytical models such as those proposed by Schapery [93], Kurner [94] and Turner [95], are commonly applied. Additionally, numerical modeling techniques, including two–dimensional (2D) micromechanical finite element method (FEM) modeling [96] and three–dimensional (3D) FEM approaches [97]. have been developed to simulate thermal expansion behavior. Similarly, the modeling of thermal residual stresses in AMMCs has been addressed in studies such as [25,34].

Due to the compositional and structural gradients in FGMs, the conventional approximations and models used for traditional composites are not directly applicable. Nevertheless, simple rules of mixtures (ROM), which are based on the volume fractions, thermal properties of the individual components, and their distribution, are still commonly employed. These include models such as the Voigt model [98], which assumes heat flow is parallel to the layers and provides an upper bound for the effective thermal properties, and the Reuss model [99], which assumes heat flow is perpendicular to the layers and provides a lower bound. Such models have been widely adopted in the analysis of FGM structures [100]. For example, the effective TC and CTE that are dependent on both temperature and position in a continuous FGM of metal and ceramic are estimated using a simple rule of mixtures [101].

FGMs have microstructures that gradually change due to the gradation in the volume fraction of their constituent phases. Micromechanical analyses of FGMs often depend on estimations of the volume fraction and shape of the reinforcing phases. In general, material property gradation in structures can be modeled in two ways: (1) by assuming a predefined profile for the variation of volume fraction, or (2) by employing micromechanical approaches to study the behavior of the inhomogeneous medium. Various homogenization techniques employed to define the spatial distribution of the constituent phases, allowing for the evaluation of effective material properties across the thickness of the FGM structure are power law function for FGM, sigmoidal function for FGM, Mori–Tanaka scheme for FGM, and exponential function for FGM. These techniques are discussed in detail in [102]. Thermal analysis of FGMs is performed by appropriately modeling the temperature distribution through the thickness, as the material properties vary along this direction and they are dealt with the following approaches.

1. Constant and linear variation

In the case of a constant temperature distribution, identical temperatures were assumed at the top (T_{hot}) and bottom (T_{cold}) surfaces. Conversely, for a linear distribution, a temperature gradient was introduced by assigning different values to (T_{hot}) and (T_{cold}). The thickness – direction temperature variation can be expressed as [103]:

$$T_z = T_{cold} + (T_{hot} - T_{cold})\frac{2Z + h}{2h} \tag{1.1}$$

where T_Z is the temperature at any point across the thickness (h) of the graded structure through the coordinate direction Z.

2. Heat conduction equation in one–dimensional case

The nonlinear temperature variation is typically derived by solving the heat conduction equation. Due to the assumption that material properties remain uniform along the plane of the plate and vary only through the thickness, a one–dimensional heat conduction equation was considered to be sufficient for performing the 2D thermal analysis [104]. The static steady state one dimensional heat equation without heat flux is given by:

$$-\frac{d}{dz} = K_z + \frac{dTz}{dz} \tag{1.2}$$

where T_Z is temperature as a function of position, K_z is thermal conductivity in thickness direction (z) of FGM

3. Heat conduction equation in three–dimensional case

Graded structures were evaluated for their static and dynamic responses by applying a simple power–law variation to the volume fractions of their ceramic and metal components and 3–D heat equation [105]:

$$\frac{\partial T}{\partial t}\rho C_p = K_x \frac{\partial^2 T}{\partial x^2} + K_y \frac{\partial^2 T}{\partial y^2} + K_z \frac{\partial^2 T}{\partial z^2} + q \tag{1.3}$$

where q is thermal flux, $\frac{\partial T}{\partial t}$ is rate of change in temperature with respect to time, ρ is density, C_p is specific heat at constant pressure, K_x, K_y, K_z are thermal conductivity in the direction of x, y, z of FGM respectively. For steady-state analysis of FGMs, the left–hand side of Eq. 1.3 is set to zero.

Extensive research has focused on thermal conductivity and residual stresses in FGMs, especially in multi–layered structures, helping to improve and optimize their thermal performance. To compute effective thermal conductivity, several multiscale and numerical methods have been developed to account for the graded microstructures. A multiscale modeling approach was developed to predict the effective thermal conductivity of two–phase graded particulate composites by considering pairwise thermal interactions within a graded RVE [106]. The method ensured the continuity of homogenized thermal fields using a transition function and accurately captured the thermal profile across the graded region. In a similar approach, the results indicated that the effective thermal conductivity distribution greatly depends on Kapitza thermal resistance, particle size, and degree of material gradient using a self–consistent model [107].

FE-based homogenization was also employed to estimate both the effective thermal conductivity and the coefficient of thermal expansion (CTE) in FGMs with periodic ceramic patterns [108]. The accuracy of these predictions was validated through experimental comparisons. In another study, a discrete element method (DEM) was used to investigate the role of pores and gradient architecture in Al/Al_2O_3 composites [109]. This model's predictions were validated against experimental measurements, demonstrating that thermal conductivity can be significantly influenced by gradient architecture and infiltration characteristics. Micromechanical modeling, particularly in SiC–carbon FGM systems with through-thickness gradation [110]. This model accounted for temperature-dependent thermal properties and a linearly varying transition zone, enabling accurate prediction of both effective thermal conductivity and CTE. These results were validated against analytical solutions and experimental data, reinforcing the model's reliability for thermal response analysis in graded composites.

The evaluation of thermal residual stress has been extensively studied through layered structures and gradient designs aimed at estimating or minimizing stress. An early analytical solution employed Laplace transforms to solve the heat diffusion equation in up to three–layered systems under specified boundary and initial conditions, and was later extended to handle eight-layered FGMs subjected to stepwise front-surface heating [111,112]. Another analytical model addressed transient heat conduction and the resulting thermal stresses in multilayered systems, identifying optimal material compositions to reduce stress distributions [113]. The thermal stress in Al/Al_2O_3 FGMs was further analyzed using a piecewise exponential gradation law [111], revealing that transient thermal stresses were lower in multi-layered configurations than in single–layer plates. In the context of Ni/Al_2O_3 systems, residual thermal stresses induced during fabrication were investigated by comparing temperature-dependent and independent gradation profiles. The study showed that a linear composition gradient from ceramic to metal yielded the minimum residual stress, and that multilayer FGMs with more than 11 layers of constant composition could replicate this low-stress state [114]. A thermoelastic numerical model applied to Al/SiC FGM system used Mori–Tanaka's theory to identify optimal phase volume fractions that minimized thermal stresses under service conditions [115]. For higher volume fraction of ceramic this method was improved and presented in [116], in which employed multiple design framework and considered the volume fraction effect to reduce the thermal residual stresses. Further, a coupled thermomechanical finite element formulation was implemented in ABAQUS™ for metal/ceramic FGM plates under plane strain conditions [117]. Using user-defined subroutines, this model was effectively handled spatially varying material properties and enabled accurate prediction of both temperature fields and residual thermal stresses in FGMs.

Despite these advancements, modeling FGMs with complex and irregular microstructures remains an area open for further investigations. Most research reported in the literature have focused on investigating composites and FGMs with microstructures exhibiting regular geometrical shapes of inclusions. However, FGMs produced by powder metallurgy, often

28

exhibit intricate, complex microstructures with varying particle distributions and porosity, and there is a limited work that explores materials with such complex microstructures. To end this, recently, a powerful non-destructive technique such as X-ray micro-computed tomography (micro-XCT) was used to provide a 3D reconstruction of the composite microstructure. A step-by-step methodology for using micro-XCT in numerical modeling of material properties of metal-ceramic composite is presented in [118]. Micro-XCT was also used to investigate the porosity and particles distribution in MMCs [119]. A FE analysis was combined with micro-XCT images capturing the actual material microstructure to compute Young's modulus in [120]. However, reports on using micro-XCT to evaluate thermal conductivity and thermal residual stresses in continuous or layered graded materials produced by powder metallurgy are still limited. Therefore, in this work, 3D finite element models of the thermal conductivity and thermal residual stresses are developed based on microcomputed X-ray tomography (micro-XCT) images of actual material microstructures. The influence of porosity, thermal resistance, and imperfect interfaces between the AlSi12 matrix and ceramic reinforcements (Al_2O_3 or SiC) is integrated into the numerical models o accurately predict the behavior of the composites and FGMs.

MOTIVATION, GOALS, and RESEARCH HYPOTHESES

2.1 Motivation

The motivation to study the topic of thermal properties and thermal residual stresses in graded Al-matrix composites reinforced with Al_2O_3 and SiC particle experimentally and by numerical simulations resulted from the needs of the automotive industry to search for new structural materials for the brake discs. Friction–based heat dissipation systems, such as automotive brake systems, should have a combination of good strength, high coefficient of friction, light weight, good wear resistance, good thermal performance, and low production cost. An automotive brake disc is one of the structural elements working under the conditions of intense friction, corrosion and increased temperature. The efficiency, durability, and heat dissipation capability of a brake disc during braking are strongly influenced by both the operating conditions and the intrinsic properties of the material. Brake discs must absorb a significant amount of mechanical energy in a very short period of time, while being exposed to the destructive effects of high temperatures and operating under high thermal loads. **Fig.2.1** shows thermal cracks propagating radially from the hat to the exterior of the disc made of grey cast iron. The use of metal–ceramic composites in brake discs often leads to residual thermal stresses due to the mismatch in thermal expansion coefficients between the metal and ceramic phases, arising both during fabrication and under operating conditions. These stresses can cause cracks to form at the interfaces which in turn can cause a disc to fail in service [91].
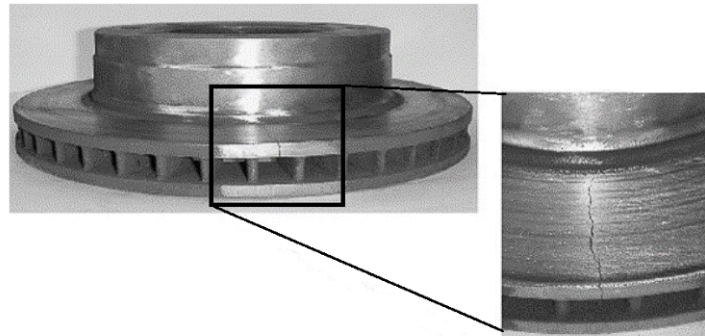
Fig.2.1 Ford (F–250) grey cast iron brake disc failure due to thermal cracking [121]. (This figure is reproduced with permission from Elsevier).

Studies have demonstrated that introducing a gradient in the microstructure of the brake disc material can substantially enhance the overall performance of the braking system [100]. This helps to improve the wear resistance on the outer surface as combined with effective heat flux dissipation of the graded system with high strength and low weight compared to brake disc

materials such as GCI currently used in the automotive industry. Furthermore, the use of a metal–ceramic FGM brake discs may reduce thermal cracking and wear [122]. The metal core of an FGM brake disc maintains strength, rigidity and quick dissipation of heat, whereas ceramic is present on the outer surfaces to resist intensive wear and elevated temperature conditions. The Al-matrix composites reinforced with ceramics AMMCs are designed for temperature applications up to 450-500 °C. The properties of the AMMCs can change with temperature, and the processing–induced thermal residual stresses can affect their performance. Therefore, a thorough understanding of their thermal and mechanical behavior under operating conditions is essential.

2.2 Goals, objectives, and research hypotheses

The materials fabricated and investigated in this thesis are AlSi12/Al$_2$O$_3$ and AlSi12/SiC layered composites (FGMs) with a stepwise gradient of the Al$_2$O$_3$ and SiC volume fractions. The main focus is on the thermal conductivity and thermal residual stresses due to their impact on brake disc performance. While the wear behavior of the fabricated AMMCs is not the primary focus of this work, it is also examined given the potential application of these materials to brake discs. Two ceramic powders, Al$_2$O$_3$ and SiC, which are commonly used in automotive AMMCs applications, are selected as the reinforcing phases in AlSi12-matrix FGMs for a comparative analysis of thermal conductivity and thermal residual stresses in the produced materials. Also, this study seeks to answer the question of whether the composites and FGMs produced by HP and SPS exhibit significant differences in their thermal properties and thermal residual stresses.

This dissertation has the following **primary goals**:

1. To fabricate the AlSi12/Al$_2$O$_3$ and AlSi12/SiC layered FGMs of high relative density using powder metallurgy.

2. To experimentally evaluate the (i) thermal conductivity, (ii) processing–induced thermal residual stresses, and (iii) wear resistance of the manufactured AlSi12/Al$_2$O$_3$ and AlSi12/SiC FGMs using HP and SPS techniques.

3. To examine the influence of the sintering technique (HP vs SPS) and the material microstructure on thermal conductivity, and processing–induced residual stresses, in both FGMs.

4. To develop micro-XCT-based FEM models for the thermal conductivity and thermal residual stresses of the FGMs taking into account the actual material microstructure and imperfect interfaces.

These goals will be accomplished through the fulfillment of the **specific objectives** listed below.

2.2.1 Experimental objectives

Materials processing

a) to prepare ungraded composite samples of AlSi12+vAl_2O_3 and AlSi12+vSiC with the ceramic content v = 10, 20, 30 vol.% using two alternative sintering techniques, hot pressing (HP) and spark plasma sintering (SPS);

b) to prepare FGM samples of AlSi12/Al_2O_3 and AlSi12/SiC consisting of two layers (0/10 vol.%, 10/20 vol.% and 20/30 vol.% of ceramic reinforcement) and three layers (10/20/30 vol.% of ceramic reinforcement) using HP and SPS;

c) to prepare reference materials AlSi12, Al_2O_3, and SiC using HP and SPS to determine the basic mechanical and thermal properties of the constituent materials.

Materials characterization

a) to characterize the microstructure of the fabricated materials using scanning electron microscopy (SEM) and X–ray micro–computed tomography (micro–XCT);

a) to measure the thermal diffusivity and specific heat of the hot pressed and spark plasma sintered samples of ungraded composites and FGMs in the temperature range of 25–300 °C to determine their thermal conductivities;

b) to measure the processing–induced thermal residual stresses (TRS) in the metal and ceramic phases of the ungraded composites and FGMs using neutron diffraction (ND);

c) to examine the wear behavior of the outer layers of FGMs produced by HP and SPS.

2.2.2. Modeling objectives

1. to develop a FEM model for thermal conductivity using the micro–XCT images to create meshes of finite elements which closely represent the microstructure of the produced FGMs;

2. to develop a FEM model for thermal residual stresses in the AlSi12 matrix and ceramic phase (Al_2O_3 or SiC) of the FGMs using FE meshes generated from the micro–XCT images;

3. to validate the predictive capability of the above models using the experimental measurements of TRS by neutron diffraction and thermal conductivity of the FGMs.

2.2.3. Research hypotheses

After conducting a thorough review of the existing literature, the following research hypotheses are formulated:

1. The average thermal residual stresses in the metal and ceramic phases of sintered AlSi12/Al_2O_3 and AlSi12/SiC FGMs are lower than the corresponding TRS in the ungraded composites.

2. The grain size of the metal matrix can affect the thermal conductivity of AlSi12/Al_2O_3 and AlSi12/SiC composites and FGMs.

3. The formation of interfacial compounds during sintering can affect the thermal conductivity of the produced ungraded composites and FGMs.

4. The use of micro–XCT–based finite element models allows for the accurate prediction of thermal conductivity and thermal residual stresses in AlSi12/Al_2O_3 and AlSi12/SiC composites and FGMs, provided that the type and shape of the finite elements are appropriately selected to represent the reconstructed microstructures closely.

METHODOLOGY

The overarching methodological approach implemented in this thesis encompasses a series of interconnected research activities. These activities include materials processing, characterization, modeling and simulations, which are collectively essential for achieving the goals of the thesis. General methodology for the research work is shown in **Fig.3.1**. A comprehensive chain of the interrelated research blocks "processing–characterization–modeling" enables the determination of the pivotal impacts of the proposed FGMs on the thermal conductivity and processing–induced thermal residual stresses under investigation.
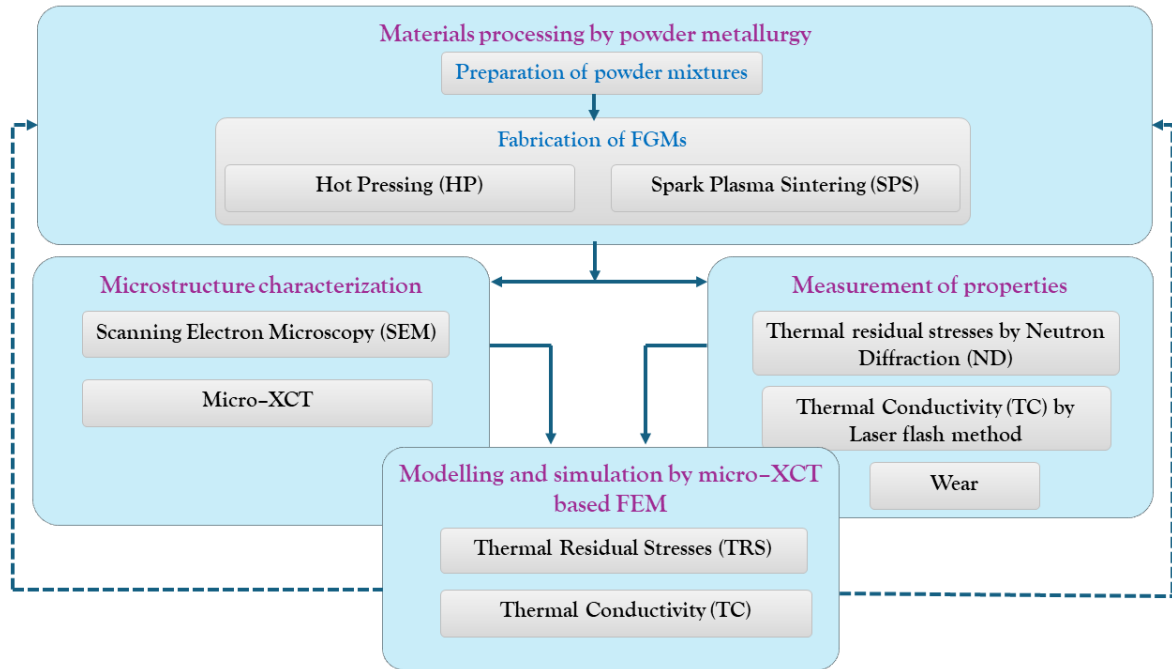
Fig.3.1 General methodology for the research work.

3.1 Materials and processing

3.1.1 Materials

The two materials selected in this study are ungraded and stepwise graded $AlSi12/Al_2O_3$ and $AlSi12/SiC$ composites. The AlSi12 alloy was chosen as the matrix material because it offers excellent specific mechanical strength, light weight, and good corrosion resistance compared to pure Al which make this material appealing for the automotive industry [123]. A commercial powder of AlSi12 (NewMetKoch, average particle size 4.6 μm, purity 99.99%) was used in the

fabrication of the ungraded composite layers and layered FGMs. The composition of the raw AlSi powder, approximately 12.1 wt.% Si and 87.9 wt.% Al, closely matches that of the standard commercial AlSi12 alloy (ENAC–44200). The SEM image and EDS spectrum of the AlSi12 powder are presented in **Fig.3.2**.

<div align="center">(a)   (b)</div>
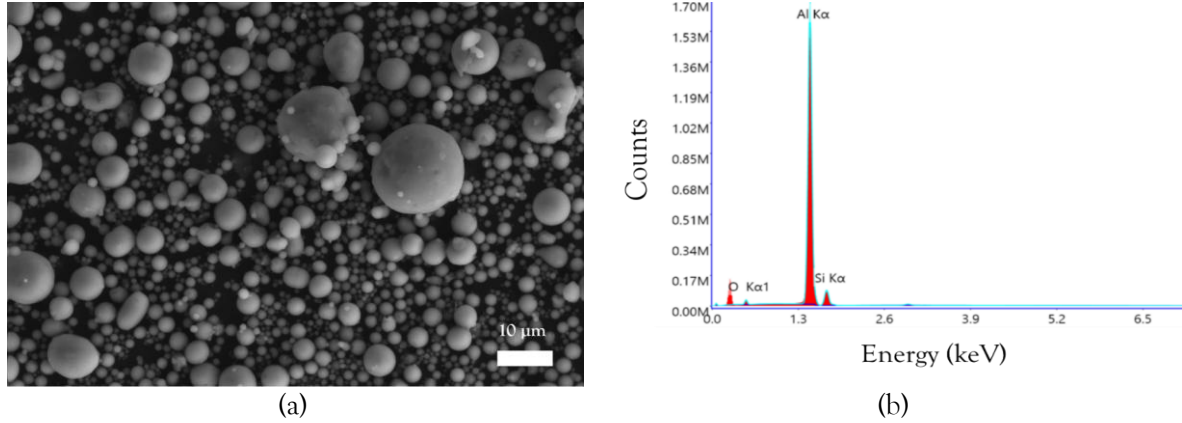
Fig.3.2 (a) SEM image of as–supplied AlSi12 powder, (b) Corresponding EDS spectrum

The ceramic reinforcements used in the processing of AlSi12 matrix composites and FGMs by powder metallurgy were aluminum oxide (Al_2O_3), also known as alumina, and silicon carbide (SiC). These ceramic materials are stable within the specified working temperature range and non–reactive with the aluminum alloys. They enhance the surface resistance, high specific stiffness, strength and wear resistance of the aluminum alloys, making them suitable for modern brake disc applications [12,124]. However, the thermal conductivity of Al_2O_3 and SiC ceramics are quite different (i.e., Al_2O_3 = 33 W/mK (*) and SiC = 240 W/mK(*)). Therefore, the selection of these two ceramic materials will make it possible to examine the effect of thermal conductivity of the reinforcing phase on the thermal conductivity of the graded composites (AlSi12/Al_2O_3 and AlSi12/SiC).

Fig.3.3 shows SEM images of the as–received commercial powders of Al_2O_3 (Goodfellow, average particle size 5.3 μm, purity 99.99%) and SiC (Goodfellow, average particle size 10 μm, purity 99.99%) used in this work. The average particle size of the raw powder was measured using a Malvern Mastersizer 3000 particle size analyser with an attached HydroMV2000 expansion unit.

---

* measured in–house on Al_2O_3 and SiC sinters.
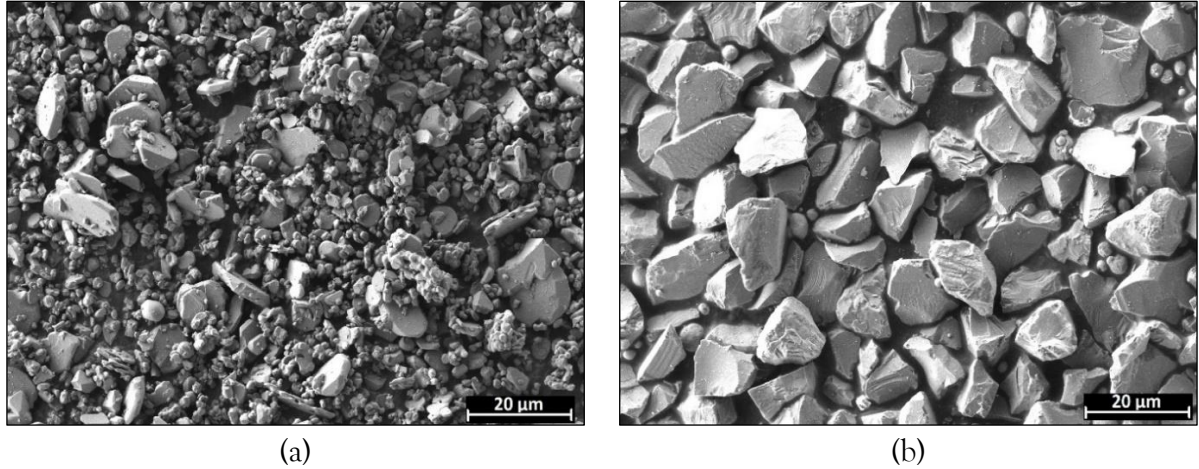
Fig.3.3 SEM images of the as–received ceramic powders: (a) Al_2O_3, (b) SiC.

The samples thicknesses of the single layer, two–layer, and three–layer materials were 1 mm, 2 mm, and 3 mm, respectively. The two–layer FGMs comprised two composite layers of equal thickness with (i) 0 and 10 vol.%, (ii) 10 and 20 vol.%, (iii) 20 and 30 vol.% of ceramic phase (Al_2O_3 or SiC). The three–layer FGM comprised three composite layers of equal thickness with 10, 20, and 30 vol.% of ceramic particles (Al_2O_3 or SiC) embedded in the AlSi12 matrix as shown schematically in **Fig.3.4**. In the following sections, the sample notation A, B, C, D, E, F, and G shown in **Fig.3.4** will be used. An indication of the ceramic reinforcement used in each case will also be provided.

Ungraded composites

10% vol. ceramic + 90% vol. AlSi12	20% vol. ceramic + 80% vol. AlSi12	30% vol. ceramic + 70% vol. AlSi12
Sample A	Sample B	Sample C

Two–layer FGMs

10% vol. ceramic + 90% vol. AlSi12	20% vol. ceramic + 80% vol. AlSi12	30% vol. ceramic + 70% vol. AlSi12
100% vol. AlSi12	10% vol. ceramic + 90% vol. AlSi12	20% vol. ceramic + 80% vol. AlSi12
Sample D	Sample E	Sample F

Three–layer FGM

30% vol. ceramic + 70% vol. AlSi12

20% vol. ceramic + 80% vol. AlSi12

10% vol. ceramic + 90% vol. AlSi12

Sample G

Fig.3.4 Schematic representation of the layered AlSi12/Al_2O_3 and AlSi12/SiC materials studied in this thesis, along with their notation. Samples A, B, C are ungraded composite samples with 10%, 20%, and 30 vol.% of Al_2O_3 or SiC. Samples D, E, F are FGMs made of two composite layers with 0/10vol%, 10/20vol.%, and 20/30vol.% of Al_2O_3 or SiC content. Sample G is a three–layer FGM containing 10, 20, and 30 vol.% of Al_2O_3 or SiC.

3.1.2   Processing

3.1.2.1   Preparation of powder mixtures

The starting powders were weighed in the specified proportions and placed in a container inside a glove box (see **Fig.3.5**) in order to avoid contamination and oxidation. The 250 ml containers with powder mixtures and Ø10 mm tungsten carbide grinding balls were then mounted in a planetary ball mill Pulverisette 5 Fritsch (see **Fig.3.6**). To achieve a uniform

distribution of ceramic particles within the AlSi12 matrix, a thorough optimization of the mixing process was conducted, and the following set of parameters was finally applied: rotational speed of 100 rpm, a ball to powder weight ratio (BPR) of 5:1, a mixing time of 5 hours, a milling interval of 15 minutes, and a 45 minute break following each run. To ensure minimal oxidation and maintain powder integrity, the powders were initially sealed in a glove box under an inert atmosphere before milling. To facilitate effective dispersion and reduce agglomeration, the containers were partially filled (half full) with heptane as a milling medium. Following the milling process, residual heptane was removed by drying the powders in a vacuum oven.


Fig.3.5 Glove box used for preparation of the starting powders (IPPT PAN).

Fig.3.6 Pulverisette 5 Fritsch planetary ball mill used to obtain powder mixtures (IPPT PAN).

3.1.2.2 Sintering

The powder mixtures were compacted and sintered using two alternative powder metallurgy techniques, hot pressing (HP) and spark plasma sintering (SPS). Prior to sintering by HP the green body was formed by cold pressing using uniaxial manual press PAREN, PLR–25/25 (**Fig.3.7**) under a pressure of 100 MPa. The green compacts were then carefully stacked in the HP die to form a single FGM sample. Hot pressing was performed in a Thermal Technology LLC HP20–4560 FP34 hot press at IPPT PAN (see **Fig.3.8 (a)**). In parallel, the sintering of the powder blends was carried out by SPS using the FCT Systeme GmbH device at the Fraunhofer–IFAM in Dresden (see **Fig.3.8 (b)**). The HP and SPS processes were carried out in a vacuum atmosphere using graphite molds. Once the pressure was released, the samples were allowed to cool in the die case until they reached room temperature (RT).
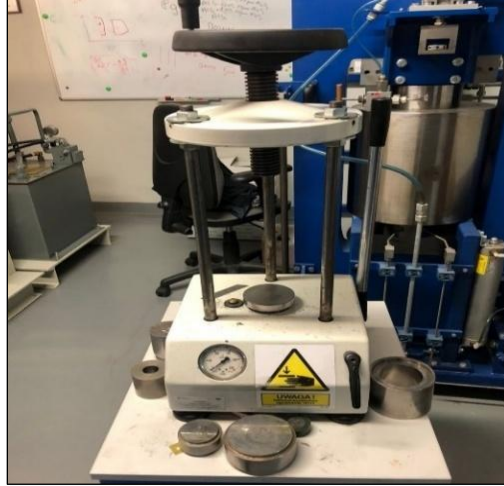
Fig.3.7 Uniaxial manual press used for cold pressing of powder mixtures (IPPT PAN).

(a) Thermal Technology LLC hot press (IPPT PAN). (b) FCT Systeme GmbH device for spark plasma sintering (Fraunhofer–IFAM, Dresden).

Fig.3.8 The equipment used for the compacting and sintering of the composites and FGMs.

Experimental trials were conducted to identify optimal processing conditions that yield composite materials with a relative density not less than 96%. Due to the substantial differences in the melting points of AlSi12, Al_2O_3, and SiC, the process parameters were varied for the fabrication of AlSi12/Al_2O_3 and AlSi12/SiC composites and FGMs. The process parameters for HP and SPS are listed in **Table 3.1** and depicted in **Fig.3.9** and **Fig.3.10**.

Table 3.1 Process parameters for sintering of AlSi12/Al₂O₃ and AlSi12/SiC composites and FGMs by hot pressing (HP) and spark plasma sintering (SPS).

Material	AlSi12/Al$_2$O$_3$		AlSi12/SiC	
Process	HP	SPS	HP	SPS
Sintering temperature (°C)	560	502	560	547
Heating rate (°C/min)	5	70	5	70
Sintering pressure (MPa)	30	40	30	40
Dwell time (min)	180	10	180	10

To ensure optimal compaction while avoiding equipment damage, the process parameters were carefully chosen and fine-tuned. During the rapid SPS process, the dwelling time was shortened and the sintering pressure increased relative to the hot pressing (HP) conditions to prevent overheating and melting of the AlSi12 material. For the AlSi12/SiC composites, considering the high melting temperature of SiC (above 2830 °C) [125], a sintering temperature of 547 °C was chosen to ensure effective bonding between AlSi12 and SiC. In the case of pure SiC sintering, a temperature of 2285 °C was applied, with a holding time of 45 minutes under pressure of 40 MPa, to achieve better densification.
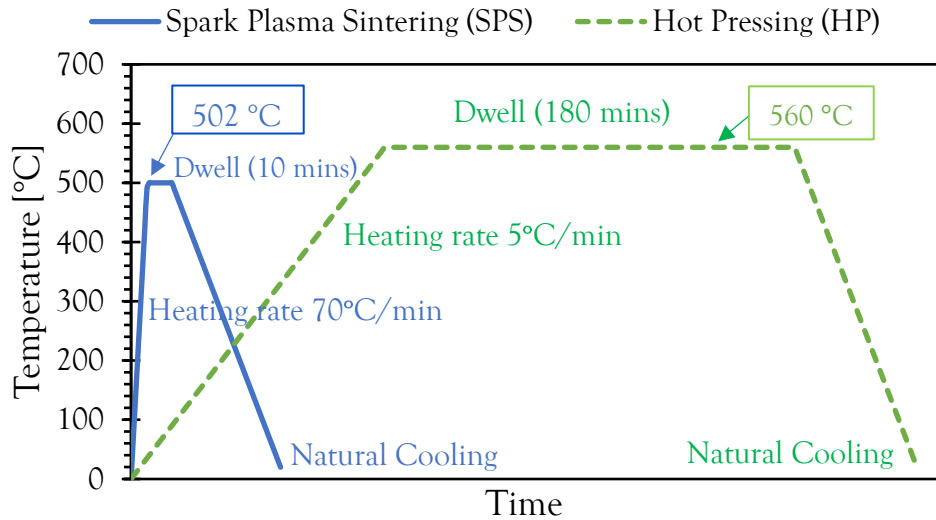
Fig.3.9 The process parameters for HP and SPS of AlSi12/Al₂O₃ composites and FGMs.
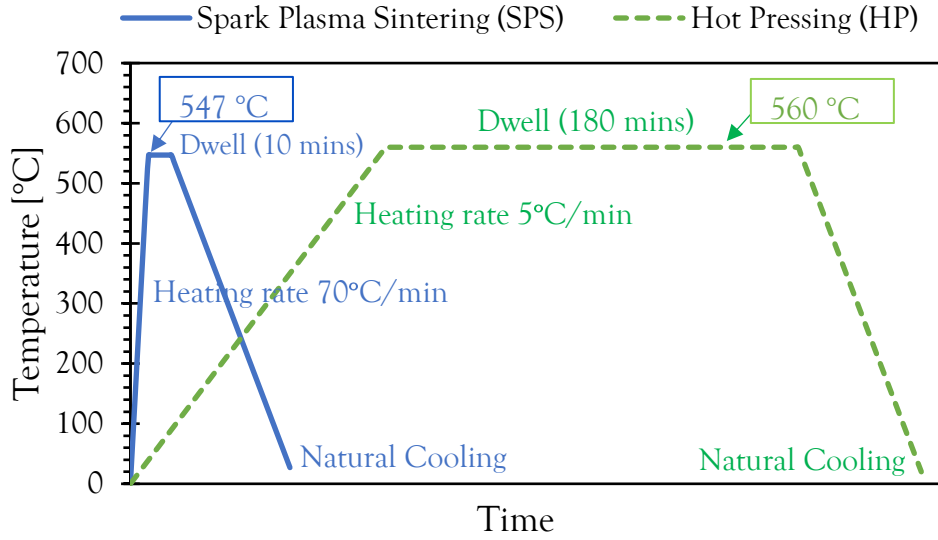
Fig.3.10 The process parameters for HP and SPS of AlSi12/SiC composites and FGMs.

3.2 Density measurement

The relative density of composite samples fabricated via HP and SPS was calculated as the ratio of the experimentally measured density to the theoretical density, expressed as:

$$\% \text{ Relative density} = \frac{\text{Measured density}}{\text{Theoretical density}} \times 100 \qquad (3.1)$$

The density of composite samples was evaluated using the Archimedes method. The theoretical density of the composites was defined for the given volume contents, using the density of AlSi12 = 2.656 g/cm^3 calculated assuming the density of Al and Si equal 2.7 g/cm^3, 2.33 g/cm^3, respectively. The density of Al$_2$O$_3$, and SiC was equal 3.95 g/cm^3 and 3.21 g/cm^3, respectively, as obtained from the experimental measurements on Al$_2$O$_3$ and SiC sinters. The immersion liquid was distilled water at a temperature of 22 °C, with a density of 0.9978 g/cm^3.

3.3 Microstructure characterization

One of the general scientific goals of this thesis is to explore the impact of material, microstructure on (i) thermal conductivity, (ii) processing–induced thermal residual stresses through experiments and microstructure–based numerical modeling. The effect of microstructure on the thermal conductivity and thermal residual stresses was examined by: (i) considering two different types of ceramic reinforcement Al$_2$O$_3$ and SiC, (ii) optimizing the sintering parameters (e.g., sintering temperature, sintering pressure, rate of heating, dwell time),

(iii) varying the volume fraction of the ceramic reinforcement in the composite layers, and (iv) employing two variants of sintering techniques (HP and SPS).

Characterization of the microstructure of the fabricated composites and FGMs was performed by (i) SEM analysis, and (ii) micro–XCT scanning. Micro–XCT scanning was used to reconstruct the 3D microstructure of the materials. The micro–XCT images were then used to build finite element meshes for the FEM simulations.

3.3.1   Scanning Electron Microscopy (SEM) analysis

To analyze the microstructure of the AlSi12/Al_2O_3 and AlSi12/SiC composites and FGMs by SEM, the samples were cut using a wire cutter at one–quarter of the diameter and along the thickness of the layer. Next, the samples were ground and polished (see **Fig.3.11**). Finally, the microstructure was analyzed using the ZEISS Crossbeam 350 system (**Fig.3.12**) with a secondary electron detector and 5kV voltage.
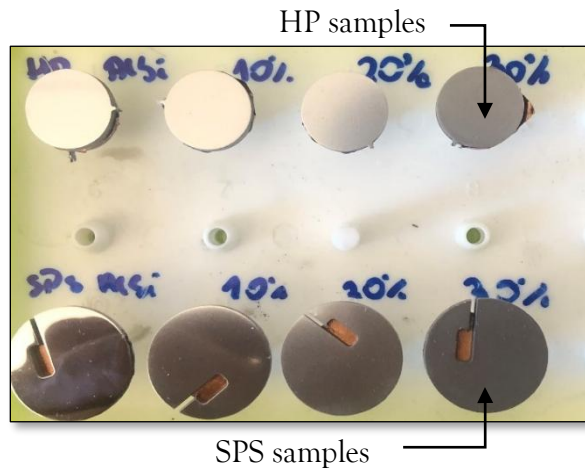
Fig.3.11 Polished HP and SPS (AlSi12/Al_2O_3) samples for SEM analysis.
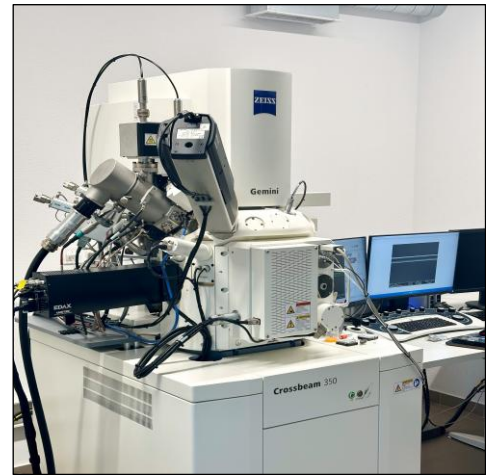
Fig.3.12 ZEISS Crossbeam 350 SEM system (IPPT PAN).

3.3.2   Micro–XCT analysis

The Nanotom M (Phoenix/GE) system was utilized to conduct X–ray micro–computed tomography (micro–XCT), a technique proven to deliver high–resolution images for metal–ceramic composite materials [118]. The micro–XCT experiments on a GE Phoenix Nanotom M device (**Fig.3.13**) were carried out at the Materials Center Leoben (Austria). The applied voltage was 160 kV, the current was 135 mA, the voxel size was optimized with respect to image contrast and was set to about 1 x 1 x 1 mm^3. For the 1 μm voxel size the source to target distance was 2.3 mm. It was crucial to capture the contours between the AlSi12 grains and the ceramic grains

accurately for the FE mesh generation. For example, segmented XCT data of AlSi12+vSiC (v = 10, 20, 30 vol.%) composites are shown in **Fig.3.14**. White color represents the AlSi12 matrix and black color represents the ceramic inclusions (SiC). The sample dimensions were 1 × 1 × 1 mm^3.

Fig.3.13 GE Phoenix Nanotom M tomograph used for micro–XCT scanning (MCL Leoben).

| 10 vol.% SiC+ 90 vol.% AlSi12 | 20 vol.% SiC+ 80 vol.% AlSi12 | 30 vol.% SiC+ 70 vol.% AlSi12 |
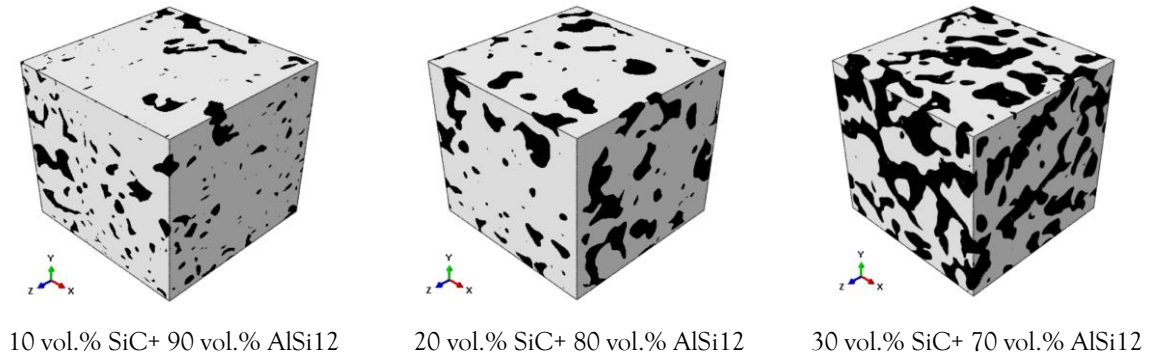
Fig.3.14 Examples of segmented micro–XCT data for AlSi12+vSiC (v = 10, 20, 30 vol.%) composites.

3.4 Thermal conductivity measurement

The thermal conductivity of the fabricated composites and FGMs was calculated as the product of the measured density, thermal diffusivity, and specific heat according to Eq. 3.2 [126]

$$\lambda = \rho \times C_p \times D \qquad (3.2)$$

where: λ is the thermal conductivity in W/mK, ρ is the density in g/cm^3, C_p is the specific heat in J/gK, and D is the thermal diffusivity in mm^2/s.

The flash method (also known as Parker's method) [127], which became an ASTM standard (E1461) [128], was used to measure thermal diffusivity. For this purpose, a modern laser flash instrument Netzsch LFA 457 (**Fig.3.15**) at Fraunhofer–IFAM Dresden was used for

non–contact measurement of thermal diffusivity on samples of approximately 3 mm in thickness. The samples were placed in the sample changer positioned at the center of the device. Throughout the experiment, a brief light pulse from a xenon lamp beneath the setup heated the underside of the sample. An infrared detector monitored the temperature increase on the opposite surface over time, allowing the calculation of the sample's thermal diffusivity (D). Schematic of the flash method is shown in **Fig.3.16**. Research studies [129,130] indicate that 175°C is appropriate for the temperature reached by pad materials during braking [123,131]. In our study, thermal diffusivity measurements were performed in the temperature range of 25–300 °C for the AlSi12/Al$_2$O$_3$ composite and in the temperature range of 25–500 °C for the AlSi12/SiC composite in an argon atmosphere to cover the entire brake operating temperature range.

Specific heat can be determined using a comparative approach, where measurements are taken sequentially on two samples under same conditions: the test sample being studied and a reference sample with known properties. Provided that the detection areas, as well as the absorption and emission coefficients of both samples, are equivalent, the specific heat (C_p) can be calculated from the following expression based on the ASTM E1461-07, Annex X2 [132]:

$$C_p = \frac{T_{ref}}{T} \times \frac{Q}{Q_{ref}} \times \frac{V}{V_{ref}} \times \frac{\rho_{ref}}{\rho} \times \frac{L_{ref}}{L} \times C_p^{ref} \qquad (3.2)$$

where: T is voltage increase of the detector signal (corresponding to the temperature increase on the back side of the samples) in V, Q is energy on the sample (integral of the laser pulse) in V, V is amplification factor, ρ is the density in g/cm^3, subscript *ref* refers to the reference sample.

The specific heat capacities (C_p, J/kgK) of the starting powders AlSi12, Al$_2$O$_3$ and SiC were measured using a differential scanning calorimeter (DSC 204 F1 Phoenix® at Netzsch thermal analysis lab, Fraunhofer–IFAM Dresden). It was measured for the temperature range of –10° C to 400° C. The measured specific heat values for AlSi12, Al$_2$O$_3$ and SiC were verified by comparison with the literature data [133]. For the AlSi12/Al$_2$O$_3$ and AlSi12/SiC$_3$ composites, the specific heat capacity values were calculated from the measured data for AlSi12, Al$_2$O$_3$ and SiC using the rule of mixtures (ROM).

It should be added that the accuracy of the calculated thermal conductivity (λ) values is estimated to be ±5% for the larger sample sizes (> 1.5 cm^3), and ± 10% for the smaller samples (< 0.9 cm^3). These estimates are obtained by calculating the measurement uncertainty based on the precision of the instruments used for the density, specific heat capacity, and thermal diffusivity measurements.

Fig.3.15 Thermal diffusivity measurement using Netzsch LFA 457 (Fraunhofer–IFAM Dresden).
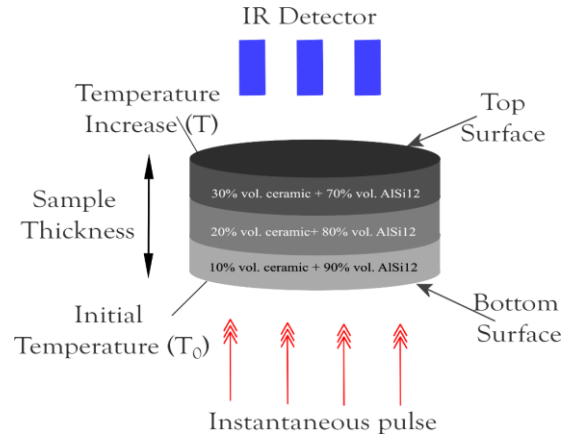
Fig.3.16 Schematic of the flash method.

3.5 Coefficient of thermal expansion (CTE) measurement

The dilatometric experiments (continuous three cycles of heating and cooling with intermediate holding for 30 mins) were performed using a thermal–mechanical analysis equipment (Netzsch DIL 402 Expedis Classic dilatometer) (see **Fig.3.17**). The test specimens were rectangular bars of about 15×5×3 mm^3 (see **Fig.3.18**). A total of five specimens were used, each with a different composition. For each test, the specimens were set upright on a quartz platform, with a movable measuring probe gently applied on top, exerting a minimal constant force of approximately 7 kPa. As the specimens were heated and cooled at a controlled rate of 3 K/min, their thermal expansion was monitored by a linear position transducer. The furnace enclosed both the specimen stage and the probe, and a continuous flow of nitrogen gas (100 ml/min) was maintained throughout the experiment. The temperature of the specimen was recorded using a thermocouple placed near the sample. The data collected consisted of curves showing the percent linear change (PLC) as a function of temperature. Using the standard Netzsch data analysis software, these curves were analyzed to determine the coefficient of thermal expansion for the tested composites. The coefficients of thermal expansion were measured for the temperature range of 25 °C to 500 °C, taking a reference temperature as 25 °C (RT). The CTE measurements were performed on the following AlSi12+vSiC samples[1]:

1. Ungraded composites AlSi12+vSiC (v= 10, 20, 30 vol.%).
2. Three–layer FGM (AlSi12+10%SiC/AlSi12+20%SiC/AlSi12+30%SiC)– longitudinal direction.
3. Three–layer FGM (AlSi12+10%SiC/AlSi12+20%SiC/AlSi12+30%SiC)– transverse direction.

---

[1] Due to a limited research stay of the author at Fraunhofer–IFAM in Dresden and budgetary constraints, the CTE measurements of the AlSi12+Al$_2$O$_3$ composites and FGMs were not conducted.

The direction parallel to the pressing direction is referred to as "longitudinal direction" and the direction perpendicular to it is called a "transverse direction" (see **Fig.3.18**).

Fig.3.17 Netzsch DIL 402 Expedis classic dilatometer used for the measurement of CTE at Fraunhofer–IFAM Dresden.
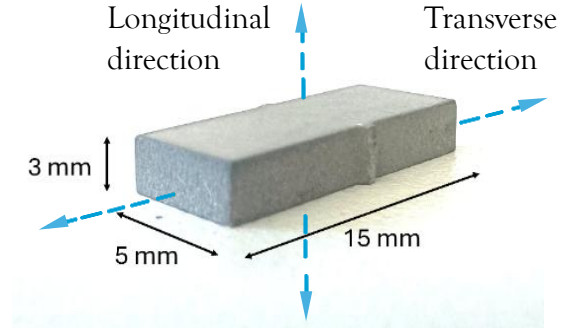
Fig.3.18 Dimensions of the specimens used to measure the CTE.

All the composite samples were cycled thrice instantaneously from –60 °C to 500 °C to detect any early effect of thermal cycling.

The coefficient of linear thermal expansion (CTE) at a specific temperature T can be determined by evaluating the change in the specimen's length, $\Delta L(T) = L(T) - L_0$, relative to its original length L_0 measured at room temperature:

$$CTE = \frac{1}{L_0} \cdot \frac{d\,(L(T)-L_0)}{dT} \qquad (3.3)$$

The instantaneous measuring uncertainty for the range of 50 °C to 500 °C was estimated to vary from ±0.4 × 10^{-6}/K (≈2% error) to ±0.07 × 10^{-6}/K (≈0.4% error) for a sample length of 3 mm and an applied smoothing range of ΔT = 50 K. To assess the reliability of the CTE measurements, a silica sample (99.9%) was evaluated at temperatures ranging from 25 to 300 °C. The measured CTE values were found to be in close agreement with the established literature values for silica [133].

3.6 Thermal residual stress measurement

Microscopic residual stresses induced in ungraded and graded AlSi12/Al_2O_3 and AlSi12/SiC composites after cooling from the sintering temperature to RT were mainly caused by the mismatch of the coefficients of thermal expansion (CTE) of the phase materials (see. **Table 3.2**). Especially, the ceramic phases (Al_2O_3 and SiC) in the investigated composites and FGMs are susceptible to unexpected cracking when subjected to local tensile stress fields. Therefore, it was reasonable to determine the residual stresses both in the AlSi12 matrix and the ceramic phases Al_2O_3 and SiC.

46

Table 3.2 Thermal expansion coefficients of the AlSi12 matrix and the reinforcements Al_2O_3 and SiC.

	AlSi12	Al_2O_3	SiC
CTE (1/deg)	23.7×10^{-6} (*)	6.5×10^{-6} (*)	4.0×10^{-6} (**)

* measured in–house on AlSi12 and Al_2O_3 sinters, ** data from the powder producer.

Neutron diffraction (ND) offers several advantages over other residual stress measuring techniques, including a significant penetration depth reaching up to a few hundred millimeters (e.g., 100 mm for Al) [134]. Additionally, ND offers good resolution and enables three–dimensional (3D) mapping of the internal micro–stresses within a material. Given these advantages, ND was used to evaluate the thermal residual stresses (TRS) present in the ungraded AlSi12/Al_2O_3 and AlSi12/SiC bulk composites, as well as the three–layer FGMs, each of which had a thickness of approximately 3 mm.

The residual stresses were measured using the pulse overlap time–of–flight diffractometer POLDI at the Swiss continuous spallation neutron source SINQ at the Paul Scherrer Institute, PSI in Villigen [135,136] as shown in **Fig.3.19**. The measurements were carried out at five central points on circular disc specimens, each about 35 mm in diameter and 1 mm thick. At each point, data were collected in three mutually perpendicular directions: one normal to the surface (radial–z) and two within the plane of the specimen (axial–x and transverse–y). The gauge volume used for these measurements was 5 mm³, ensuring precise assessment of the specimens' properties. The measurements were carried out for following samples:

(i)   AlSi12+vAl_2O_3 (v= 10, 20, 30 vol.%)– composites.
(ii)   AlSi12+vSiC (v= 10, 20, 30 vol.%)– composites.
(iii)   Each individual layer in the three–layer FGM sample of AlSi12+vAl_2O_3 (v= 10, 20, 30 vol.%).
(iv)   Each individual layer in the three–layer FGM sample of AlSi12+vSiC (v= 10, 20, 30 vol.%).
(v)   Powder measurements to obtain stress–free reference values.

In order to preserve the residual stress state present after the sintering process, the samples intended for neutron diffraction experiments did not undergo any subsequent machining or mechanical processing steps.

Fig.3.19 Mounting of samples for the measurement of residual stresses using neutron diffraction (ND) at Paul Scherrer Institute (PSI), Villigen. Switzerland.

By fitting Gaussian functions to the Bragg peaks in the reciprocal q–space, their precise positions were obtained. With these values, and using Bragg's law (λ = 2d sinθ) alongside the equation d = $2\pi/q$, the strain in the material was determined as follows:

$$\varepsilon_i = \frac{d_i + d_0}{d_0} = \frac{q_i}{q_0} - 1 \tag{3.4}$$

where d_0 is the unstrained interplanar distance of the considered lattice planes obtained from the neutron diffraction measurements of pure powders (AlSi12, Al_2O_3, SiC), q is the corresponding Bragg peak position in the reciprocal space determined by the Gaussian fit of the data obtained from the powder measurements, d_i are measured interplanar distances in x, y, z directions (axial, transverse and normal) , and q_i are the corresponding Bragg peak positions for those directions, respectively.

Strain measurement orientations using neutron diffraction along three perpendicular directions are shown in **Fig.3.20**.
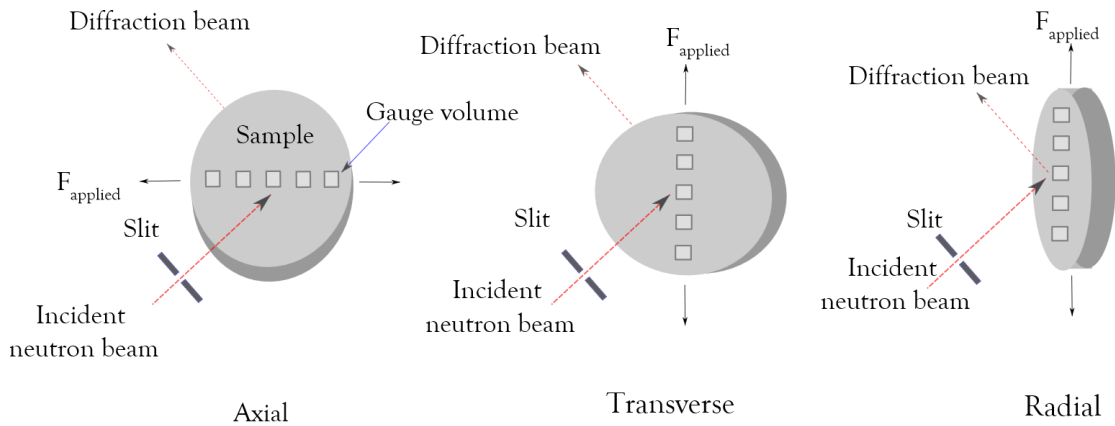
Fig.3.20 Measurement directions for neutron diffraction strain analysis in three orthogonal axes.

Once the deformations in the tested materials are determined from Eq. 3.4, the thermal residual stresses can be calculated using the Hooke's law, namely:

$$\sigma_x = \frac{E}{(1-2v)(1+v)}[(1-v)\varepsilon_x + v(\varepsilon_y + \varepsilon_z)] \tag{3.5}$$

$$\sigma_y = \frac{E}{(1-2v)(1+v)}[(1-v)\varepsilon_y + v(\varepsilon_x + \varepsilon_z)] \tag{3.6}$$

$$\sigma_z = \frac{E}{(1-2v)(1+v)}[(1-v)\varepsilon_z + v(\varepsilon_x + \varepsilon_y)] \tag{3.7}$$

3.7 Wear test

Materials choice for brake discs is significantly affected by their ability to withstand high friction and minimize abrasive wear at the contact surface of the disc to the brake pad. One significant issue encountered during high–speed braking is the formation of scratches appearing on the contact surface. This is due to the abrasive particles getting between the brake pad and the disc. This phenomenon necessitates the of investigating the tribological behavior of these materials to accurately assess their wear resistance.

As mentioned in Section 2.2, this thesis focuses on the thermal properties and thermal residual stresses of the AlSi12/Al_2O_3 and AlSi12/SiC FGMs, and the wear behavior is not the main focus here. However, since the resistance to frictional wear is an important issue for brake disc materials, some preliminary wear analysis of the fabricated AlSi12/Al_2O_3 and AlSi12/SiC FGMs was performed. To investigate the wear behavior of the outer surface of the FGM samples, a dry sliding wear test was performed using a flat–end cylindrical pin. This linear abrasive wear test was selected because of a larger contact surface area than in a conventional ball–on–disc test, which is more suitable for the intended application to brake discs. The measured wear resistance was compared to a reference material sample prepared from a serial Brembo brake disc.

The pin–on–flat wear test was performed using a Taber Linear Abraser Model 5750 with a 0.635 cm diameter flat end pin (H–10 Calibrade, Taber Industries) as shown in **Fig.3.21**. Prior to the wear test, the surfaces of the samples were polished to mirror finish. The samples were mounted in a special clamp to restrain any movement during the reciprocating stroking of the pin on the sample (see **Fig.3.22**). Before each subsequent measurement, the friction surface of the counter–sample (ceramic pin) was polished with 180-grit sandpaper. The parameters used for the wear test are shown in **Table 3.3**. The applied pressure was equal to 0.62 MPa and was constant during the test because of the flat-ended pin. This is approximately half the nominal

pressure exerted on brake pads in passenger cars [137]. The stroke length and speed were determined based on the sample dimensions and parameters of the Taber Linear Abraser 5750.

Fig.3.21 Taber Linear Abraser – Model 5750 (IPPT PAN).
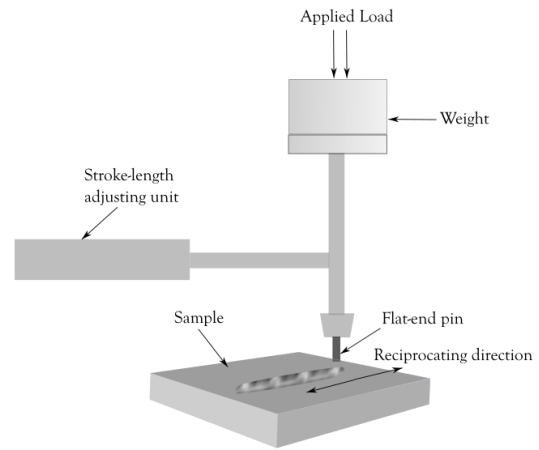
Fig.3.22 Scheme of the pin–on–flat wear set–up.

Table 3.3 The parameters of the pin–on–flat wear test using Taber Linear Abraser model 5750.

Type of movement	Stroke length (mm)	Frequency (cycles/min)	Testing time (hrs)	Total sliding distance (mm)	Normal force (N)
Reciprocating	25.4	60	2	365,760	19.61

The wear rate was initially evaluated using the mass loss. The difference in the sample mass measured before and after the test represents the mass loss due to wear. The specific wear rate (SWR) is defined as follows:

$$\text{SWR} = \frac{\text{Volume loss}}{\text{Sliding distance} \times \text{Normal force}} \ [\text{mm}^3/\text{Nm})] \tag{3.8}$$

where the volume loss is calculated from the measured mass loss and the material density.

In addition to evaluating the specific wear rate in the Taber test, the specimens were analyzed by SEM to identify the wear mechanisms. Energy dispersive X–ray spectroscopy (EDAX) analysis was also performed to determine the weight percentages of the elements present on the wear track surface.

3.8 Numerical modelling and simulation

The thermal conductivity and the thermal residual stresses of the $AlSi12+vAl_2O_3$ and $AlSi12+vSiC$ (v = 10, 20, 30 vol.%) composites and FGMs were modeled using the finite element method (FEM) for both HP and SPS samples. The FEM approach requires meshed models to perform numerical simulations. These mesh models were generated based on the actual microstructure of the materials obtained from micro computed X-ray tomography (micro-XCT). The process of building the FE mesh model for an FGM is shown schematically in **Fig.3.23**. The first step shows the FGM sample used for the computer X-ray tomography scanning, the second step shows the segmented XCT data capturing a volume of $100 \times 100 \times 100$ μm^3. The third step shows the meshing of graded material from micro-XCT scans. The fourth step shows the meshed data used for the modeling.

FGM sample   Segmented XCT data   Meshing of graded material   Meshed data for numerical simulations
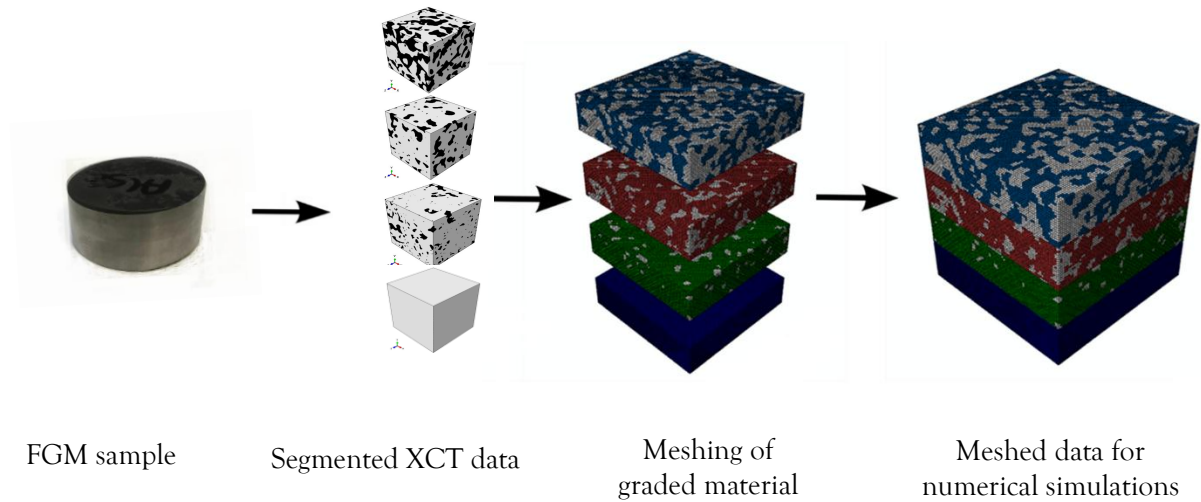
Fig.3.23 Workflow schematic for FGM microstructure reconstruction highlighting the image processing stages.

Micro-XCT enabled the direct reconstruction of the material's real microstructure, capturing the size, shape, and spatial arrangement of the reinforcing particles. The resulting digital micro-XCT data were then utilized to create finite element (FE) meshes that accurately replicated the samples' microstructure, using the commercial image processing software ScanIP/ScanFE (Simpleware Ltd., Exeter, UK) [138]. The tool builds a three-dimensional representative volume element (RVE) that replicates the composite microstructure, comprising the AlSi12 matrix and ceramic reinforcements (Al_2O_3 or SiC). The modeled phase volumes accurately reflect the actual proportions corresponding to the real material.

Meshes consisting of cubic and tetrahedral elements were generated based on the micro–XCT data for accurate representation. **Fig.3.24** shows that tetrahedral elements with additional smoothing allow for a more accurate reconstruction of the microstructure, while cubic elements lead to a poor representation of the actual composite microstructure. To accurately predict thermal properties and thermal residual stresses in composite materials through numerical modeling, it is essential to have a precise representation of the microstructure. Capturing the intricate details and features of the microstructural architecture is the basis to obtaining reliable simulation results and insights into the material's behavior. An improperly constructed finite element mesh can severely compromise the accuracy of numerical modeling results. In the context of thermal residual stress simulations, an incorrectly generated mesh can lead to the appearance of spurious stress concentrations at unsmoothed grain boundaries or other microstructural features. These stress concentrators can distort the calculation outcomes, rendering the model predictions unreliable and potentially misleading. Therefore, meticulous care must be taken during mesh generation, thereby ensuring the validity of the simulation results.

Material	Color
Ceramic (Al_2O_3)	
AlSi12	
Pores	
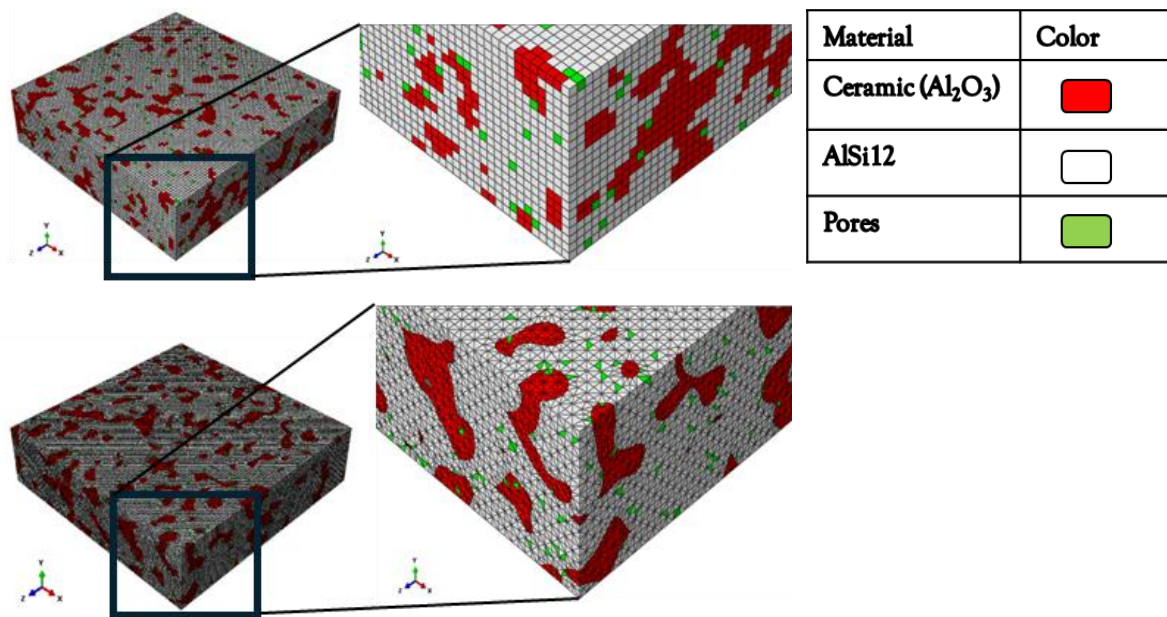
Fig.3.24 Exemplary finite element meshes based on the micro–XCT images of the AlSi12+20 vol.% Al_2O_3 composite microstructure: (a) cubic elements, (b) tetrahedral elements, created using the ScanIP/FE software.

Another important factor in representing the true microstructure is the accuracy of volume fraction estimation using micro–XCT data. An effective way to evaluate this is by

comparing the ceramic volume fraction in the composite sample to the volume represented by the finite elements assigned to the ceramic phase within the model.

This can be assessed by comparing the volume fraction of the ceramic in the actual composite with the volume occupied by the finite elements representing the ceramic material in that composite, as summarized in **Table 3.4**. The volume fractions of Al_2O_3 and SiC derived from the micro–XCT analyses closely match the nominal values of 10, 20, and 30 vol.% with only minor deviations.

Table 3.4 Quantified ceramic volume fractions in the FE models constructed using micro–XCT scans

	AlSi12+vAl$_2$O$_3$ (v = vol.%)			AlSi12+vSiC (v= vol.%)		
	v=10	v=20	v=30	v=10	v=20	v=30
Ceramic volume fraction in micro–XCT based FE mesh [%]	9.89	21.11	29.78	10.31	20.45	30.90

Selecting an appropriate RVE is a key challenge in thermal residual stress modeling. Several techniques for identifying the RVE are presented in [139]. Based on the definitions described therein, the following approach was proposed to determine the size of the RVE. A finite element (FE) mesh was constructed that was large enough to replicate the actual microstructure observed through SEM and micro–XCT imaging, ensuring that the phase volume fractions of the composite were accurately preserved. The effective elastic properties of the model, were then determined. Subsequently, smaller FE meshes were constructed, maintaining the same phase composition and verifying the calculated Young's modulus remained consistent with that obtained from the larger mesh. The smallest mesh that met these conditions was identified as the appropriate size for the RVE.

Using the above approach, the RVE was defined with dimensions of 50 × 50 × 50 elements, matching to a volume of 50 × 50 × 50 μm³. One voxel from a micro-XCT image was represented by one cubic finite element of 1 ×1 ×1 μm³. A similar approach and future applications of X-ray CT are reviewed in [140,141]. Finally, the FE model was implemented in Abaqus™ [142] to calculate the heat flux and thermal residual stresses.
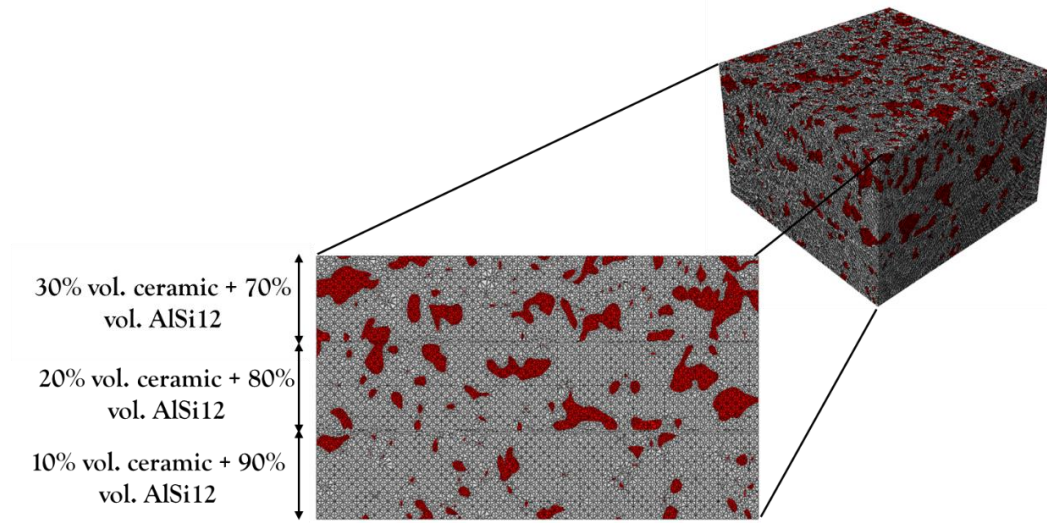
3.8.1   Thermal conductivity

The calculations of the thermal conductivity of the AlSi12+vAl$_2$O$_3$ and AlSi12+vSiC (v = 10, 20, 30 vol.%) ungraded composites and FGMs were performed with the FE models generated from micro–XCT scans of the microstructure of these samples using Abaqus™ [142]. **Fig.3.25** shows the mesh models for the AlSi12/Al$_2$O$_3$ three–layer FGM.

Eight-node hexahedral heat transfer elements were used for the cubic FE model, while four-node tetrahedral heat transfer elements were employed for the tetrahedral FE model to solve the linear Fourier heat conduction equation within a three-dimensional domain:

$$q = -\lambda_{eff}\, \Delta T \tag{3.9}$$

where: q is heat flux, λ_{eff} is effective thermal conductivity, and $\Delta T = T_{hot} - T_{cold}$.

The temperature on the two opposite faces of the specimen was kept constant, wherein one of the faces was assumed to be hot (e.g.,T_{hot}= 200), and the other face to be cold (e.g.,T_{cold}= 100). The remaining specimen's faces were characterized by the adiabatic state.

Fig.3.25 Tetrahedral mesh model of the three-layer FGM generated from micro-XCT images using ScanIP/FE software.

The effective thermal conductivity can be expressed as [143]:

$$\lambda_{eff} = -\frac{q}{A} \cdot \frac{L}{T_{hot} - T_{cold}} \tag{3.10}$$

where: L is the length of the specimen, A is the cross-sectional area, $(T_{hot} - T_{cold})$ is the temperature difference between the bottom layer and the top layer of the specimen, q is the overall heat flux obtained by integrating the fluxes across the inlet surface of the elements, expressed as:

$$q = \int_A -\lambda \frac{\partial t}{\partial z} dxdy \tag{3.11}$$

Equations 3.10 – 3.11 were used for all the elements to calculate the heat flux and the effective thermal conductivity. The thermal conductivities of the constituent materials, measured experimentally at room temperature, are provided in **Table 3.5**.

With the steady state heat transfer conditions, the FE model was implemented to compute the heat flux in each element. For the cubic element model, where all the elements are of same volume, the average heat flux is calculated as a sum of the heat fluxes in all elements divided by the number of elements (n) as shown in the Eq. (3.12).

$$q_{ii}^{avr} = \sum_{j=1}^{n} \frac{q_{ii}^{j}}{n} \tag{3.12}$$

where n is the number of elements and q_{ii}^{j} denote the components of the heat flux vector q_{xx}, q_{yy} and q_{zz} in the jth element.

For tetrahedral element model where the volume of every element is different, the average heat flux is calculated from the following formula:

$$q_{ii}^{avr} = \frac{\sum_{j=1}^{n} v^{j} \cdot q_{ii}^{j}}{\sum_{j=1}^{n} v^{j}} \tag{3.13}$$

where v^{j} is the volume of jth element and q_{ii}^{j} are the thermal fluxes q_{xx}, q_{yy} and q_{zz} in the jth element. The average heat flux q_{zz} in the direction Z (thickness direction of the model/sample) is considered in order to resemble the experimental measurements.

Table 3.5 Thermal conductivities of the constituent materials used in the numerical models.

Processing route	Thermal conductivity (W/mK)			
	AlSi12	Al$_2$O$_3$	SiC	Pores (Air)
Hot pressing (HP)	204.8*	33.0*	–	0.025
Spark plasma sintering (SPS)	188.0*	–	240*	0.025

* measured in-house on AlSi12, Al$_2$O$_3$ and SiC sinters.

3.8.2   Porosity

Porosity has a significant detrimental effect on the effective thermal conductivity and strength of metal matrix composites. Pores or voids act as barriers to heat flow, reducing the cross–sectional area available for heat conduction. This results in a lower effective thermal conductivity compared to a fully dense AlSi12/SiC composite [144]. The size, shape, and

distribution of the pores also influence thermal conductivity, with larger and more interconnected pores having a greater effect [145]. Analytical models like the Hasselman–Johnson, Maxwell model, and their modifications account for the effect of porosity by treating pores as a second phase with very low thermal conductivity [144,146] In order to study the effect of porosity on the effective thermal conductivity of the composite layers and the FGMs, the porosities obtained from the experimental measurements for Al_2O_3, SiC, ungraded AlSi12+v Al_2O_3 composites and AlSi12+vSiC (v = 10, 20, 30 vol.%) composites were implemented in the finite element models. The FE meshes were generated from the micro–XCT scans of the actual microstructure of the composites. Generally, micro–computed tomography can be used for the identification of pores, but in the case of nanopores, voxel size is a limiting factor in identifying the location of pores in segmented XCT data. Therefore, in numerical modeling, matrix elements were selected randomly with the total volume of the porosity calculated from the relative densities derived from the measured and theoretical densities of the corresponding composites. It was assumed that pores were evenly dispersed throughout the AlSi12 matrix and filled with air, with assumed thermal conductivity of 0.025 W/mK [147]. One of the assumptions that pores were present only in the AlSi12 matrix, which was used in the finite element modeling of thermal conductivity, was supported by the pore volume distribution obtained by the gas adsorption method [148]. The results are discussed in detail in Section 4.1.

3.8.3 Interfacial thermal conductance

The imperfect interface between metal and ceramic phases in a composite material can significantly influence its effective thermal conductivity. At the interface between metal and ceramic, there exists an interfacial thermal resistance (ITR) or Kapitza resistance. Thermal resistance at interfaces can occur in two distinct scenarios. When two phases do not make perfect contact, the resulting resistance is termed "thermal contact resistance." However, even when the contact between phases is perfect, some resistance still exists. In this case, the resistance is referred to as "thermal boundary resistance." This resistance impedes heat flow across the interface due to phonon scattering and electronic properties [149]. Determining the interfacial thermal conductance at the microscopic scale for FGMs pose significant experimental challenges, necessitating the use of sophisticated and specialized equipment [150].

The analytical estimation of the thermal conductivity of two–phase materials was derived by Maxwell [85] using mean–field theory and has been frequently referenced by other researchers thereafter. These studies are based on the assumption of perfect contact between the particles and the matrix phase. Hasselman and Johnson [151] advanced the concept of interfacial thermal barrier resistance, modifying Maxwell's formula, found the interfacial thermal conductance between Al and SiC particles in a 40% volume fraction composite to be 147 MW/m²K [47]. As an alternative approach, the interfacial thermal conductance can be estimated through

theoretical and analytical models and schemes like the Nan–Birringer model [152], and its modifications account for the ITR by introducing an interfacial resistance parameter. These models predict a reduction in the effective thermal conductivity with increasing ITR. Other analytical scheme include the differential effective medium (DEM) scheme developed by Bruggeman [153]. These theoretical frameworks provide a means to approximate the interfacial thermal conductance without relying on complex experimental setups, although with inherent assumptions and limitations. Numerical studies and finite element simulations have also demonstrated that increasing ITR between the metal and ceramic phases leads to a decrease in the overall effective thermal conductivity of the composite [91,154].

The calculations, based on the phonon incident on the interface and the energy carried by the phonon, were performed using two models: the acoustic mismatch model (AMM) [155] and the diffuse mismatch model (DMM) [156]. These calculations estimated the interfacial thermal resistance between aluminum (Al) and aluminum oxide (Al_2O_3), as well as between Al and silicon carbide (SiC), to be in the range of 10^{-8} to 10^{-9} m^2 K/W. Based on the AMM [157], the interfacial thermal conductance (h_c) can be calculated as:

$$h_c \cong \frac{1}{2} \, C_p(\rho_{in} \times c_{in}) \left(\frac{c_{in}}{c_{tran}}\right)^2 \frac{\rho_{in} \times c_{in} \times \rho_{tran} \times c_{tran}}{(\rho_{in} \times c_{in} + \rho_{tran} \times c_{tran})^2} \tag{3.14}$$

where C_p is the specific heat of matrix, ρ is the density, c is the phonon velocity. The subscripts *in* and *tran* denote the incident side (i.e. matrix) and transmission side (i.e. ceramic), respectively.

Using the Eq. 3.14, the interfacial thermal conductance (h_c) between AlSi12 and Al_2O_3 was calculated. Taking, ρ_{tran}=3950 kg/m^3, c_{tran}=7038 m/s, the interfacial thermal conductance is $h_{c(AlSi12/Al_2O_3)}$=1.18×10^8 W/m^{2}K. Similarly, the interfacial thermal conductance between AlSi12 and SiC was calculated taking ρ_{tran}= 3190 kg/m^3 and c_{tran} = and 8519 m/s [158], which gives $h_{c(AlSi12/SiC)}$=1.06×10^8 W/m^{2}K. For both cases the matrix was assumed as pure Al, and the following values were adopted ρ_{in}= 2656 kg/m^3, c_{in} = 3040 m/s [157], C_p = 899 J/kg.K;

In the FE simulations, the interfacial thermal conductance between two phases can be easily implemented in Abaqus™ First, the contact between two surfaces (i.e., metal and ceramic) must be defined by assigning the surface names to a contact interaction. In Abaqus™/Standard simulations, this functionality is provided through the "Interactions" module [142]. **Fig.3.26** displays yellow marks that visually indicate the contacts between the metal (AlSi12) and ceramic (Al_2O_3 or SiC) phases, representing the spots where specific contact properties were applied within Abaqus™.
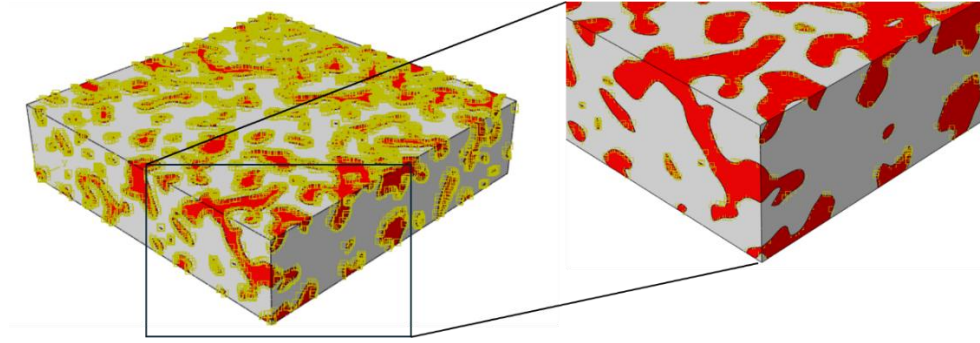
Fig.3.26 Abaqus™ FE model illustrating the interfacial contacts between AlSi12 matrix and Al_2O_3 reinforcement.

3.8.4 Thermal residual stress

Residual stresses arising during the cooling stage of HP and SPS sintering in both ungraded $AlSi12/Al_2O_3$ and AlSi12/SiC composites, as well as FGMs, were evaluated using numerical models built upon reconstructed real microstructures derived from micro-XCT data, following the approach detailed in Section 3.8.3.

In the numerical simulations, the ceramic reinforcements were modeled as linear elastic materials, whereas the AlSi12 matrix was represented using an elastic–plastic material model. The material properties employed in the calculations are summarized in **Table 3.6**, with the plasticity parameters for the AlSi12 elastic–plastic model listed in **Table 3.7** sourced from Ref.[159].

Table 3.6 Elastic constants and thermal expansion coefficients of the AlSi12 matrix and the ceramic reinforcement Al_2O_3 and SiC applied in the FEM analysis.

Material constant	AlSi12	Al_2O_3	SiC
E (GPa)	70 [*]	380 [*]	410 [**]
Poisson's ratio	0.35[***]	0.22 [**]	0.15 [**]
CTE (1/deg)	$23.7×10^{-6}$ [*]	$6.5×10^{-6}$ [*]	$4.0×10^{-6}$ [*]

* measured in–house on AlSi12 and Al_2O_3 sinters, ** data provided by the powder producer, *** adopted from [29].

To simulate the cooling process from 500°C to room temperature (20°C) within the mold, boundary conditions were established where initially all surfaces were fixed and a pressure of 30 MPa (for HP) or 40 MPa (for SPS) was applied on the top surface at a uniform temperature of 500°C. Subsequently, while maintaining fixed surfaces, the applied pressure was removed, and the temperature was set to 20°C to represent the cooling phase. Finally, all surfaces except

the bottom were released to simulate sample removal after cooling. These conditions were incorporated into the finite element model to calculate the resulting thermal residual stresses in each element.

Table 3.7 Elastic–plastic properties of the AlSi12 matrix used in the simulations [159].

Stress [MPa]	300	310	330	350	360	370	375	379	382
Plastic strain	0	0.01	0.02	0.03	0.04	0.05	0.06	0.07	0.08

In the cubic element model, the average thermal residual stress is determined by averaging the stress values across all elements, as shown in Eq. (3.15).

$$\sigma_{ii}^{avr} = \sum_{j=1}^{n} \frac{\sigma_{ii}^{j}}{n} \tag{3.15}$$

where n is the number of elements and σ_{ii}^{j} are the stress components σ_{xx}, σ_{yy}, and σ_{zz}, in the jth element.

For the tetrahedral element model the average thermal residual stress is calculated from the Eq.3.16

$$\sigma_{ii}^{avr} = \frac{\sum_{j=1}^{n} v^{j} \times \sigma_{ii}^{j}}{\sum_{j=1}^{n} v^{j}} \tag{3.16}$$

where v^{j} is the volume of jth element and σ_{ii}^{j} are the stress components σ_{xx}, σ_{yy}, and σ_{zz}, in the jth element.

RESULTS for AlSi12/Al$_2$O$_3$ COMPOSITES and FGMs

4.1 Density measurements and porosity

The densities of the composite samples fabricated by HP and SPS were determined using the Archimedes method (see Section 3.2). The relative densities were determined by taking the ratio of the measured density of the composite sample to the theoretical density. Theoretical density, measured density, resulting relative density and porosities of AlSi12/Al$_2$O$_3$ composites consolidated by HP and SPS are listed in the **Table 4.1**.

Table 4.1 Densities and porosities of AlSi12/Al$_2$O$_3$ composites consolidated by HP and SPS.

Material	HP				SPS		
	Theoretical density [g/cm^3]	Measured density [g/cm^3]	Relative density [%]	Porosity [%]	Measured density [g/cm^3]	Relative density [%]	Porosity [%]
AlSi12	2.656	2.654	99.940	0.060	2.653	99.902	0.098
AlSi12+10 vol.% Al$_2$O$_3$	2.787	2.778	99.676	0.324	2.771	99.424	0.576
AlSi12+20 vol.% Al$_2$O$_3$	2.918	2.913	99.812	0.188	2.906	99.572	0.428
AlSi12+30 vol.% Al$_2$O$_3$	3.050	3.038	99.609	0.391	2.974	97.511	2.489
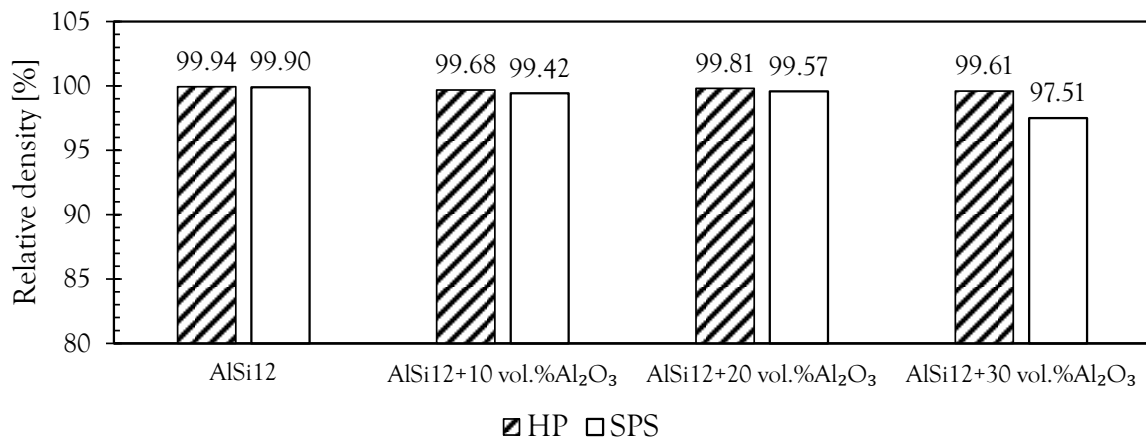
Fig.4.1 Relative densities of AlSi12/Al$_2$O$_3$ composites fabricated by HP and SPS.

The relative densities of the HP samples with 10, 20, and 30 vol.% Al$_2$O$_3$ exceeded 99.6%, while the SPS samples had slightly lower densities than the corresponding HP samples (see **Fig.4.1**). This is due to the precisely optimized HP process parameters. A DSC analysis of

the AlSi12 powder confirmed its melting point to be near 590 °C. Hence, the selection of a sintering temperature of approximately 560 °C for the HP process just below the melting threshold promoted an effective densification of the composite without melting.

On the other hand, the sintering temperature in the SPS process, set at 502 °C, was significantly lower than that of the HP process in order to avoid melting of AlSi12 powder at a much higher SPS heating rate of 70 °C/min compared to HP (5 °C/min). Higher heating rate causes a higher temperature gradient during heating facilitated by a pulsed direct current passing through the center of the material. As a result, the heat transfer begins at the center of the sample and progresses outward, potentially melting the AlSi12. Additionally, while the SPS process applied a higher pressure of 40 MPa compared to 30 MPa in the HP process, the relative densities of the SPS samples with 10, 20, and 30 vol.% Al_2O_3 were slightly lower than those of the corresponding composites produced by the HP. The sample with 30 vol.% Al_2O_3 (SPS), could not achieve a density comparable to that of the other samples. This was because the higher amount of ceramic content, the lower sintering temperature, and rapid exposure to temperature created voids between the densely packed ceramic particles (see **Fig.4.5 (c)**). As a result, the relative density reached only 97.5% as shown in **Fig.4.1**. However, the relative densities of the FGMs were approximately 99.7% for both HP and SPS samples.

To assess the nano–porosity within the sintered powders, the initial AlSi12 and Al_2O_3 powders were characterized using the gas adsorption method. Measurements carried out with the AutoSorbiQ Quantachrome analyzer verified the presence of nanopores in both powders. The total pore volumes per unit mass, measured across a diameter range of 0.35 to 375 nm (close to the instrument's limits), are presented in **Table 4.2**. Notably, the total nanopore volume in the matrix is approximately fivefold greater than in the Al_2O_3 phase. This finding supports the assumption made in the numerical modeling of thermal conductivity (refer to Section 3.8.2).that pores were primarily present in the AlSi12 matrix (HP).

Table 4.2 Nanopore volume and mean pore size in AlSi12 and Al₂O₃ powders as determined by the gas adsorption analysis.

| Sample	Total pore volume (cm^3/g)	Average pore diameter (nm)
AlSi12 (HP)	0.078	4.40
Al₂O₃	0.015	5.82

4.2 Microstructure analysis

The microstructure of AlSi12/Al_2O_3 composites and FGMs was analyzed using scanning electron microscopy (SEM) and micro–computed X-ray tomography (micro–XCT) as described in Section 3.3. Additionally, Energy Dispersive X-ray Spectroscopy (EDS) was employed to analyze the chemical composition of the unreinforced aluminum alloy (AlSi12). To facilitate

comprehensive observation, samples were sectioned both parallel and perpendicular to the gradient direction. Microscopic examination was performed with the primary objective of evaluating the overall quality of the microstructure. Key areas of focus included the interface quality (assessing the integrity of the bond between the metallic and ceramic phases) and defect identification (detect and characterize various microstructural imperfections, such as residual porosity, cracks, grain size, etc.). These defects were of particular interest due to their potential negative impact on the thermal conductivity and their influence on the thermal residual stresses induced during the processing. A comprehensive evaluation of the cross–section of the gradient material was performed to assess the continuity of connections between adjacent composite layers, examining the transition zones between gradient material compositions.

4.2.1 Microstructure analysis of unreinforced AlSi12 samples sintered by HP and SPS

SEM analysis was performed on unreinforced AlSi12 samples sintered by HP and SPS to examine differences in their microstructure. The analysis revealed significant variations in the grain sizes of Al and Si in the unreinforced AlSi12 matrix sintered by HP and SPS (see **Fig.4.2**). The observed differences in the microstructure of the AlSi12 (HP) and AlSi12 (SPS) samples were due to different process conditions, the heating rates, and the maximum sintering temperature being the most important factors (refer to **Fig.3.9** and **Fig.3.10**).

Additionally, the interface between silicon (Si) and aluminum (Al) grains in ungraded AlSi12 sample was examined in high–magnification SEM observation. The results showed that a well–defined and smooth interface between the Si and Al grains was observed in pure AlSi12 sintered by HP (**Fig.4.3**).

(a)   (b)
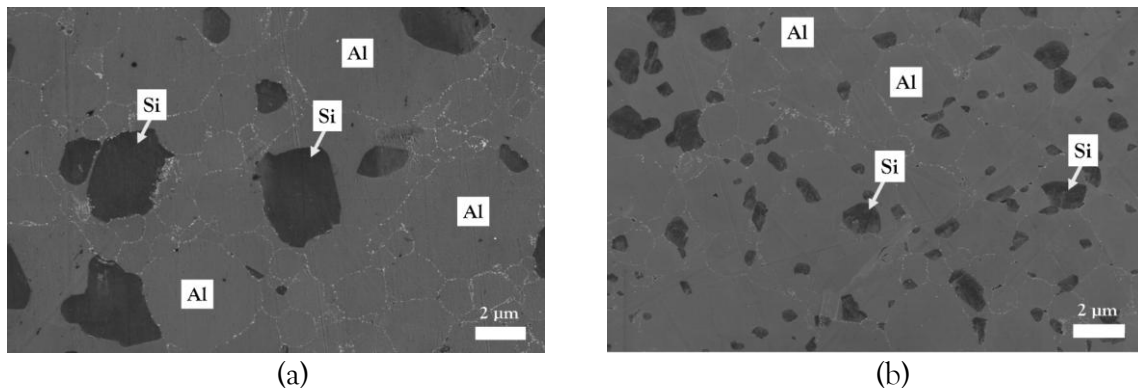
Fig.4.2 SEM images of AlSi12 alloy samples consolidated via (a) HP and (b) SPS without ceramic reinforcement.
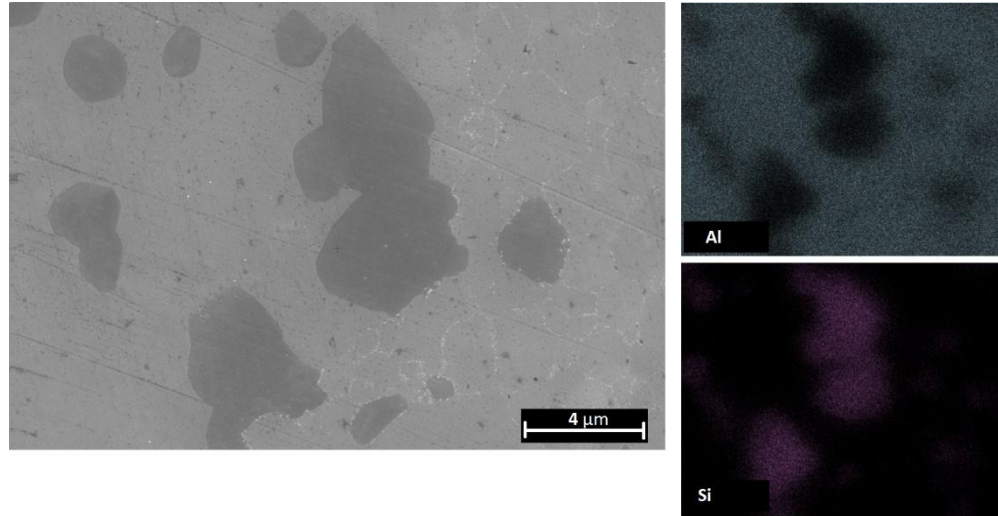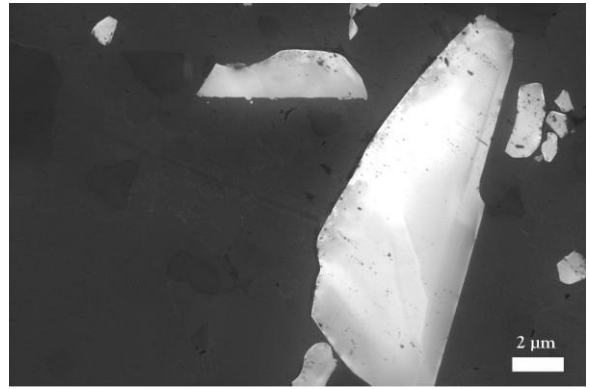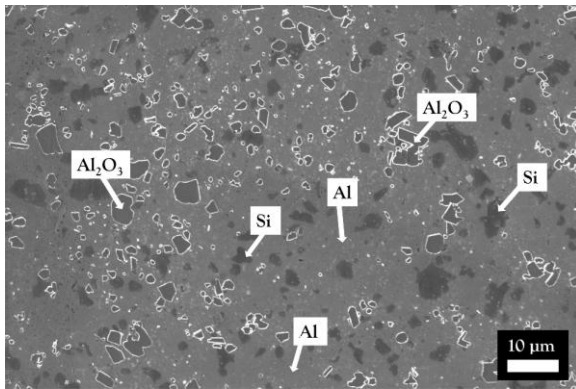
Fig.4.3 Microstructure of hot–pressed AlSi12 showing Si and Al grain boundaries (left) and the corresponding EDS mapping (right).

4.2.2 Microstructure analysis of AlSi12/Al$_2$O$_3$ composites and FGMs

The SEM micrographs of the single layer composites fabricated by HP and SPS are presented in **Fig.4.4 a–c** and **Fig.4.5 a–c**, respectively. All of the micrographs reveal a homogeneous microstructure characterized by an even distribution of ceramic grains (light phase) within the AlSi12 matrix (dark phase). The interface between the ceramic and metallic phases is smooth indicating good bonding. The SEM images on the right side of Figs 4.4 and 4.5 show nearly perfect adhesion. This adhesion is used as a perfect–contact assumption at the interfaces for modeling purposes. However, the observation also uncovered the presence of occasional voids between the densely packed Al$_2$O$_3$ grains (see **Fig.4.5 (c)**), which lead to a lower sintered density and material properties of the SPS samples. In particular, some protrusions are visible on the surface, which are attributed to scratches on the AlSi12 matrix due to polishing during sample preparation for SEM analysis. No micropores or voids or cracks were observed in the microstructure of the HP samples. However, the experiment on finding the volume distribution of nanometric pores by the gas adsorption method showed that there exists certain volume of nanopores in the AlSi12 matrix (more details are provided in Section 4.1).

The seamless transition between the composite layers shown in **Fig.4.6 a–d**, which occurs during the sintering of the FGMs, accounts for the development of a metallurgical bond. This bond ensures structural integrity between layers with a stepwise gradient of the ceramic (Al$_2$O$_3$) content in the continuous matrix (AlSi12).

(a) AlSi12+10 vol.% Al$_2$O$_3$
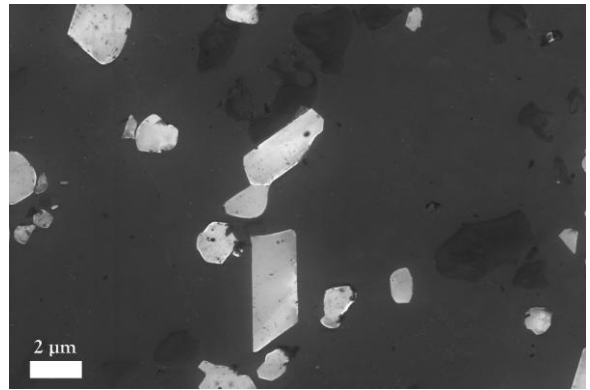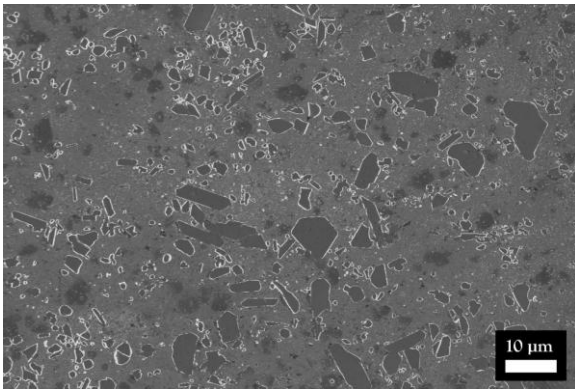
(b) AlSi12+20 vol.% Al$_2$O$_3$
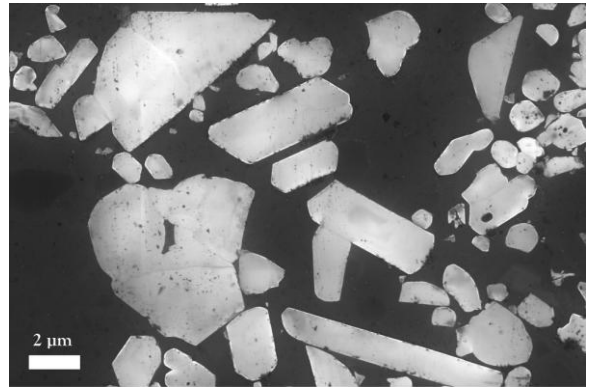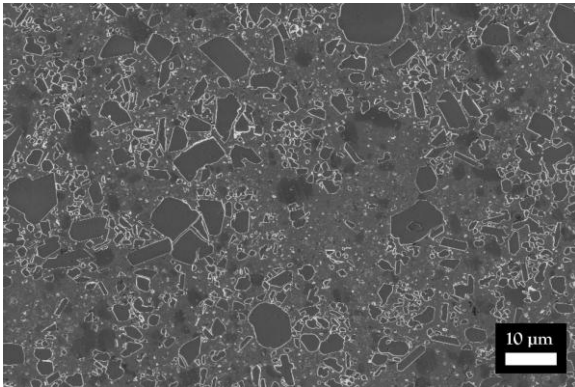
(c) AlSi12+30 vol.% Al$_2$O$_3$

Fig.4.4 Microstructures of the etched surface of hot–pressed (HP) AlSi12–Al$_2$O$_3$ composites: (a) AlSi12+10 vol.% Al$_2$O$_3$, (b) AlSi12+20 vol.% Al$_2$O$_3$, (c) AlSi12+30 vol.% Al$_2$O$_3$.
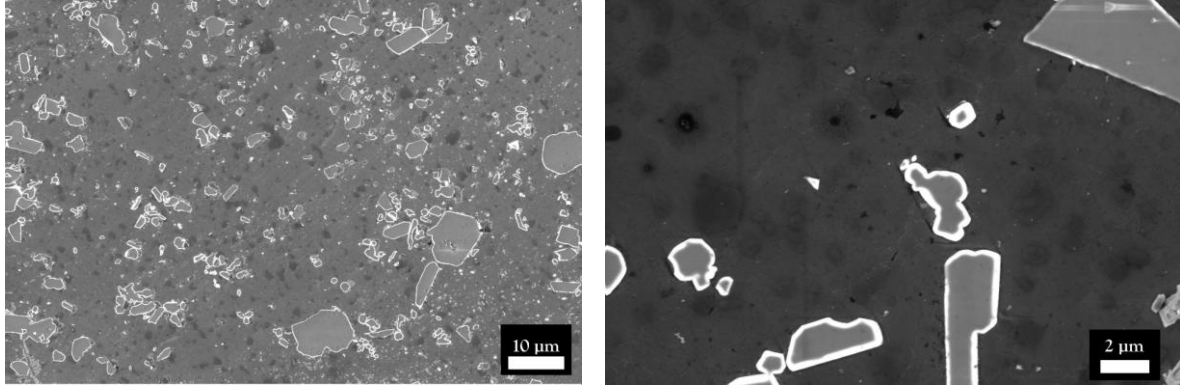
(a) AlSi12+10 vol.% Al_2O_3
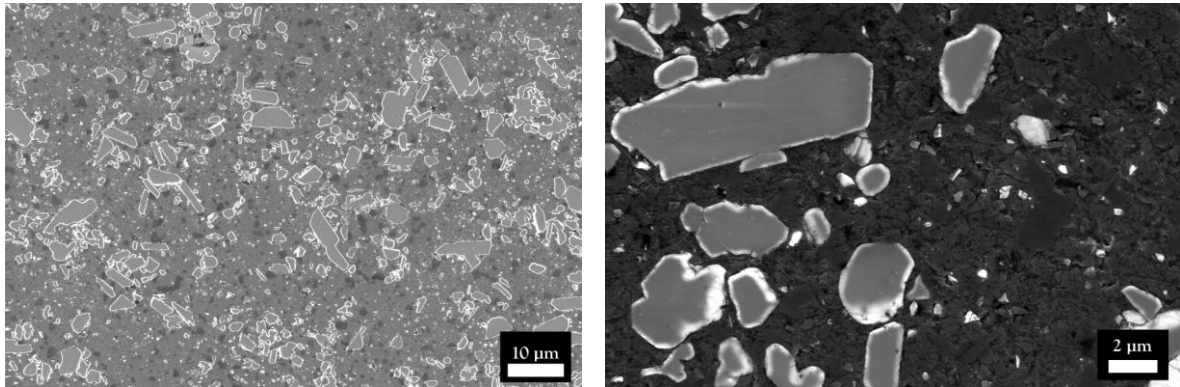
(b) AlSi12+20 vol.% Al_2O_3
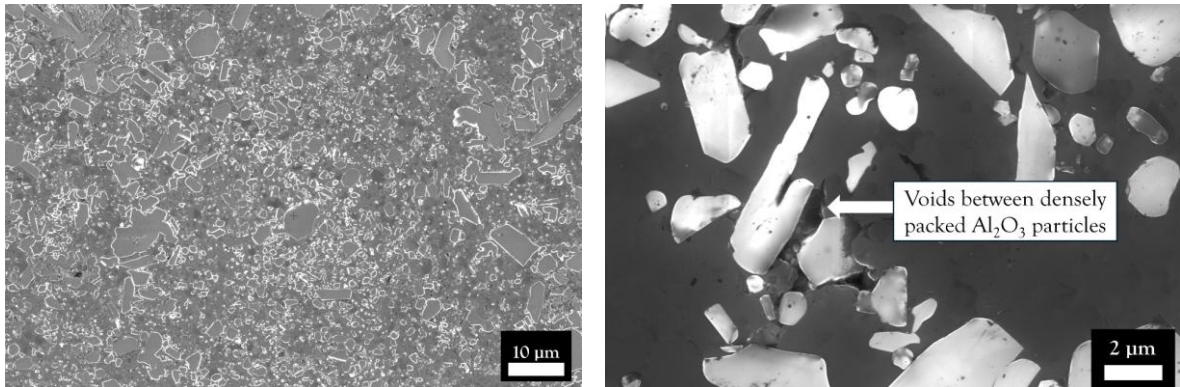
(c) AlSi12+30 vol.% Al_2O_3

Fig.4.5 Microstructures of the etched surface AlSi12/Al_2O_3 composites produced by SPS: (a) AlSi12+10 vol.% Al_2O_3, (b) AlSi12+20 vol.% Al_2O_3, (c) AlSi12+30 vol.% Al_2O_3.
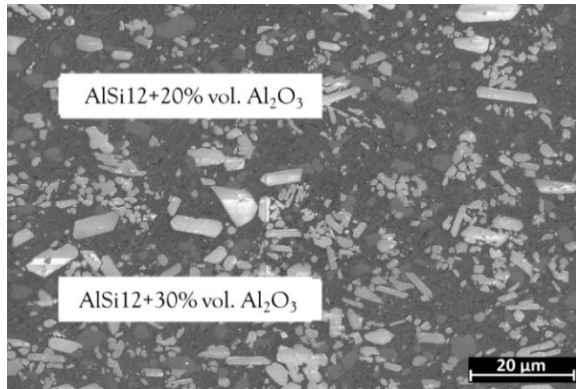
(a) 2–layer FGM (AlSi12+20 vol.% Al$_2$O$_3$/AlSi12+30 vol.% Al$_2$O$_3$)
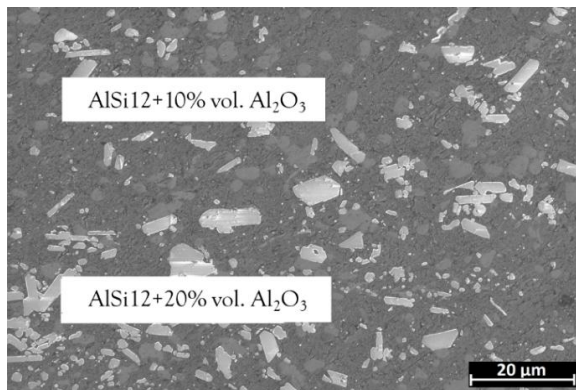
(b) 2–layer FGM (AlSi12+10 vol.% Al$_2$O$_3$/AlSi12+20 vol.% Al$_2$O$_3$)
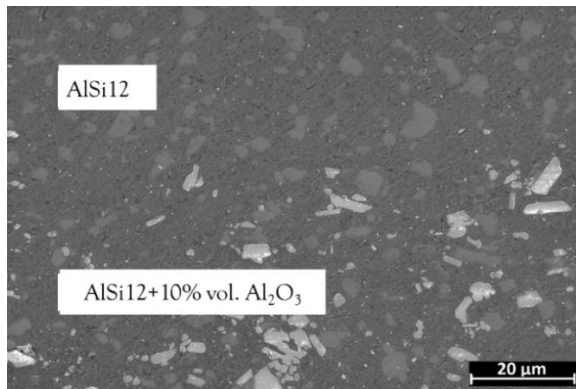
(c) 2–layer FGM (AlSi12/AlSi12+10 vol.% Al$_2$O$_3$)
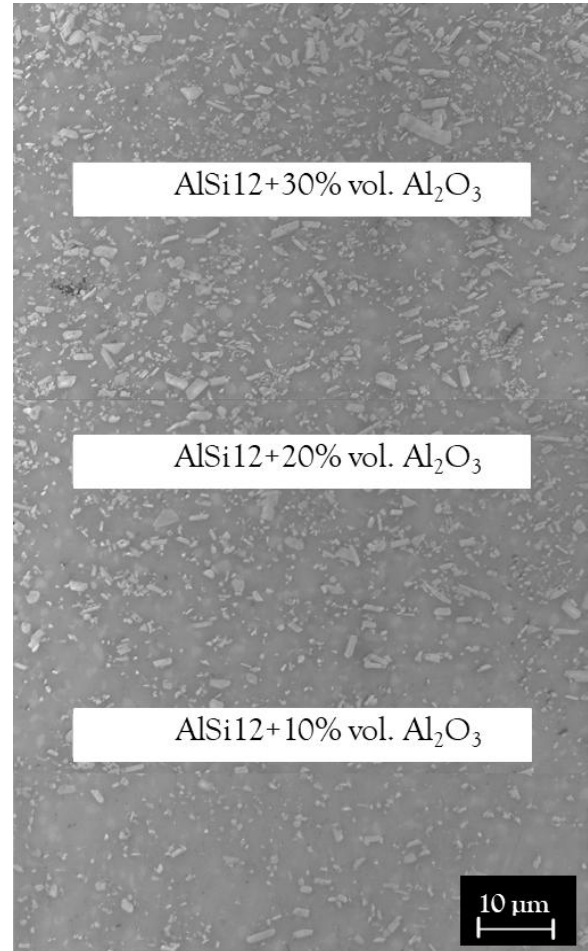
d) 3–layer FGM (AlSi12–10/20/30 vol.% Al$_2$O$_3$)

Fig.4.6 SEM micrographs of the interlayer regions in the HP–consolidated AlSi12/Al$_2$O$_3$ composites. (a)–(c) show the microstructure of two–layer FGMs, and (d) the microstructure of the three–layer FGM.

4.3 Thermal conductivity of AlSi12/Al$_2$O$_3$ composites and FGMs

4.3.1 Experimental evaluation of thermal conductivity

Thermal conductivity was determined from the measured thermal diffusivity, specific heat capacity, and the density of the fabricated ungraded composites layers and the FGMs. The detailed methodology is presented in Section 3.4. The thermal conductivity of the AlSi12 sinter was measured using the flash method over the temperature range from RT to 300 °C. A noticeable discrepancy was observed in the thermal conductivity measurements at room temperature (RT) between pure AlSi12 sintered by HP (204.8 W/mK) and pure AlSi12 sintered by SPS (188.0 W/mK). As illustrated in **Fig.4.7**, this difference is particularly significant at RT but diminishes progressively, disappearing entirely as the temperature exceeds 250°C.
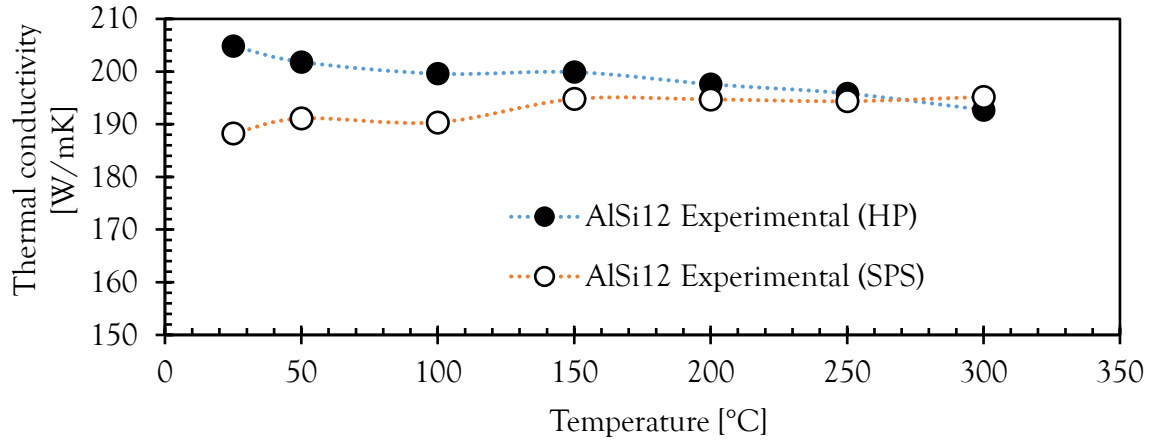
Fig.4.7 Temperature–dependent thermal conductivity of unreinforced AlSi12 consolidated via HP and SPS, measured between RT and 300 °C.

The discrepancy in thermal conductivity between the HP samples and the SPS samples of AlSi12 can be attributed to the following reasons:

1. *Larger grain sizes*. The SEM analysis revealed that the HP–sintered AlSi12 samples had a larger average grain size (2.80 µm) compared to the SPS samples (1.69 µm) (refer **Fig.4.2**). The grain size measurement procedure followed the ASTM E112 standard [128]. Larger grains produced by HP have higher intrinsic thermal conductivity than finer grains [160]. In addition, finer grains in the SPS samples necessarily produce more grain boundaries, resulting in increased grain boundary resistance, which in turn reduces thermal conductivity.

2. *Smoother interfacial bonds*. The interfaces between Al and Si grains in the HP–consolidated AlSi12 samples are smooth and free of defects or pores (see **Fig.4.3**). This contributes to enhancing interfacial bond strength, which in turn increases the thermal conductivity of the sample [161].

It is noteworthy that the porosities of both AlSi12 samples are comparable (0.060% for the HP sample and 0.098% for the SPS sample, as det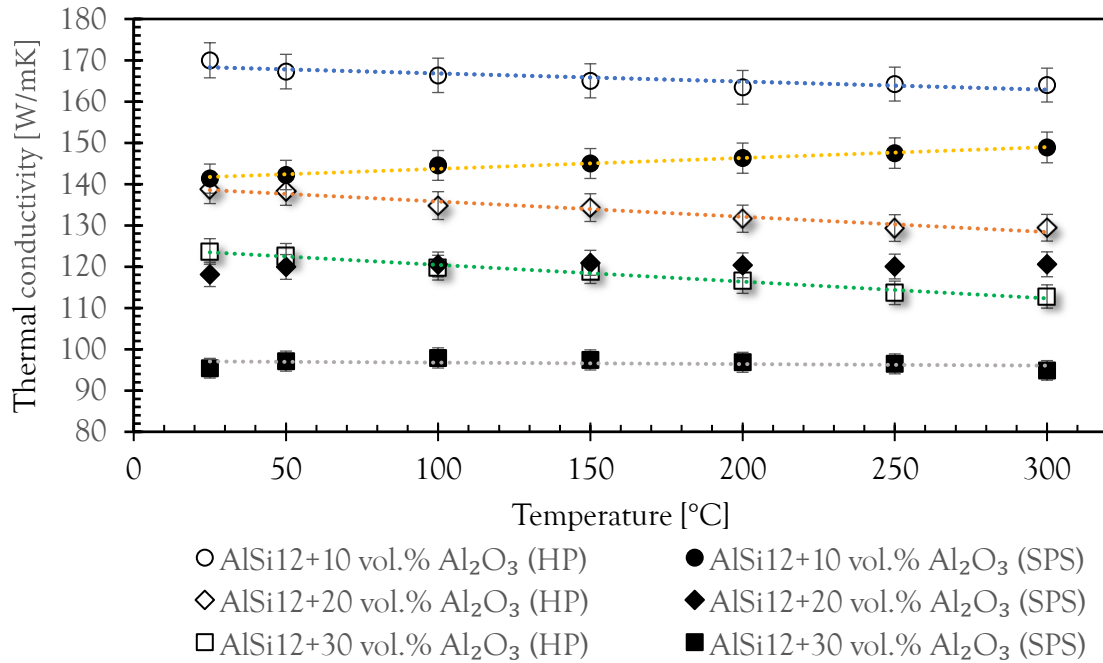ailed in **Table 4.1**). This observation indicates that porosity is not the primary factor contributing to the observed discrepancy in thermal conductivity between the two AlSi12 samples, as illustrated in **Fig. 4.7**.

Table 4.3 shows the thermal conductivity measurements of the AlSi12/Al_2O_3 composite samples and the FGMs produced by HP and SPS, with different Al_2O_3 volume fractions. These measurements were obtained using the flash method over the temperature range from RT (25°C) to 300°C.

Table 4.3 Thermal conductivity (λ) measurements of AlSi12/Al_2O_3 composites and FGMs reinforced with different volume fractions of alumina: sample A (AlSi12+10%Al_2O_3), sample B (AlSi12+20%Al_2O_3), sample C (AlSi12+30%Al_2O_3), sample D (two–layer FGM: 100%AlSi12/AlSi12+10%Al_2O_3), sample E (two–layer FGM: AlSi12+10%Al_2O_3/AlSi12+20%Al_2O_3), sample F (two–layer FGM: AlSi12+20%Al_2O_3/AlSi12+30%Al_2O_3), sample G (three–layer FGM: AlSi12+10%Al_2O_3/AlSi12+20%Al_2O_3/AlSi12+30%Al_2O_3).

Thermal conductivity of **HP** samples, λ [W/mK]						
Single layer			Two–layer (FGM)			Three–layer (FGM)
T [°C]	Sample A	Sample B	Sample C	Sample D	Sample E	Sample F	Sample G
25	169.99	138.75	123.69	180.86	162.31	136.73	147.09
50	167.25	138.32	122.55	181.11	160.07	136.13	146.72
100	166.34	134.80	119.76	178.01	159.27	133.58	143.54
150	165.02	134.30	118.91	176.93	157.62	132.42	142.73
200	163.44	131.62	116.45	175.25	155.02	129.62	140.45
250	164.22	129.36	113.66	175.09	155.69	127.14	138.11
300	163.98	129.43	112.78	175.54	154.32	126.84	137.51

Thermal conductivity of **SPS** samples, λ [W/mK]						
Single layer			Two–layer (FGM)			Three–layer (FGM)
T [°C]	Sample A	Sample B	Sample C	Sample D	Sample E	Sample F	Sample G
25	141.33	118.14	95.41	165.04	133.05	110.58	119.89
50	142.21	119.94	97.13	166.04	133.30	110.55	118.90
100	144.53	120.54	97.90	165.02	134.42	110.17	119.34
150	144.99	120.94	97.42	168.53	138.07	110.66	117.86
200	146.29	120.34	96.84	169.12	138.11	109.97	116.44
250	147.51	120.04	96.46	170.02	139.29	109.62	117.34
300	148.89	120.58	94.88	171.31	140.72	108.78	116.42

As the volume fraction of Al_2O_3 increases, the thermal conductivity of the composite samples A, B, and C decreases. This trend is consistent for both HP and SPS samples across the entire temperature range, with a more pronounced effect at lower temperatures (see **Fig.4.8**) It also shows that the thermal conductivity of samples sintered via HP is consistently higher than that of their SPS samples. This disparity can be attributed to two factors: (i) the lower thermal conductivity of the AlSi12 matrix material in SPS compared to HP (as shown in **Fig.4.7**), and (ii) the higher porosity of SPS samples relative to HP samples, as indicated in **Table 4.1**. It should also be noted from **Fig.4.8** that the graded composites fabricated by hot pressing exhibit nearly stable thermal conductivity throughout the temperature range from room temperature to 300°C.

○ AlSi12+10 vol.% Al_2O_3 (HP)   ● AlSi12+10 vol.% Al_2O_3 (SPS)
◇ AlSi12+20 vol.% Al_2O_3 (HP)   ◆ AlSi12+20 vol.% Al_2O_3 (SPS)
□ AlSi12+30 vol.% Al_2O_3 (HP)   ■ AlSi12+30 vol.% Al_2O_3 (SPS)

Fig.4.8 Results of thermal conductivity measurements of the single layer composite samples with 10, 20, and 30% of Al_2O_3 (samples A, B, and C in **Fig. 3.4**) fabricated by HP and SPS in temperature range from RT to 300°C.

The trend observed in single-layer composites (samples A, B, and C) is also seen in the two-layer FGMs (samples D, E, and F in **Fig. 3.4**) sintered by HP and SPS, as shown in **Fig. 4.9**. Importantly, the two-layer samples D (100%AlSi12/AlSi12+10%Al_2O_3) fabricated by HP and SPS, manifested the highest thermal conductivities among all the tested AlSi12/Al_2O_3 samples.
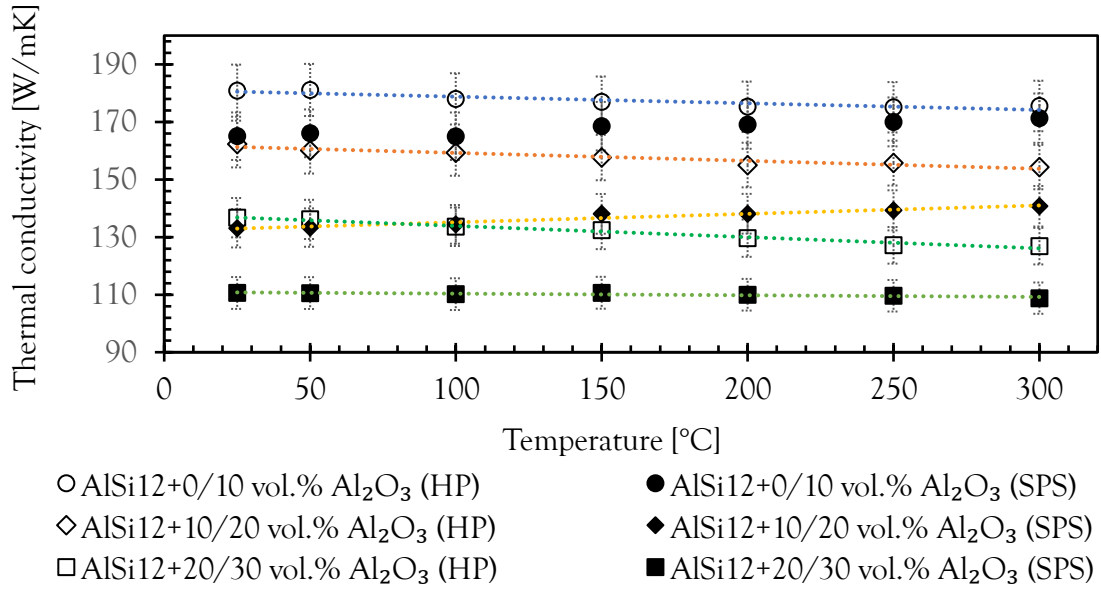
Fig.4.9 Results of thermal conductivity measurements of two-layer FGMs (sample D, sample E, and sample F in **Fig.3.4**) fabricated by HP and SPS in the temperature range from RT to 300 °C.

A key observation was made for the three-layer FGM sample G, having compositions of 10, 20 and 30 vol.% Al_2O_3, produced using both HP and SPS methods, when compared to the two-layer sample F, which contained 20 and 30 vol.% Al_2O_3. Throughout the entire temperature range tested, the three-layer FGM demonstrated a consistently greater thermal conductivity than the two-layer FGM (see **Fig.4.10**).
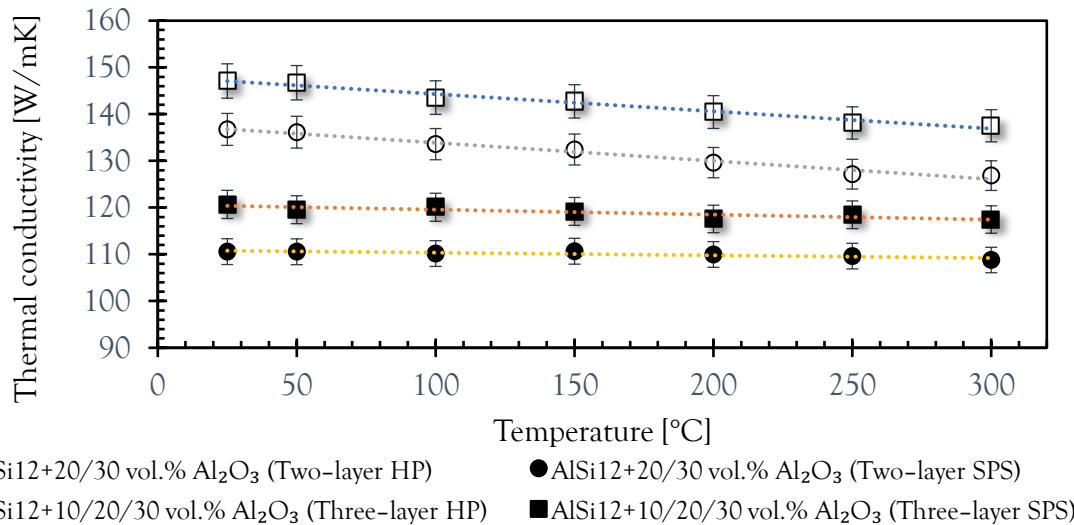
Fig.4.10 Comparison of thermal conductivity measurements for the two-layer FGM (sample F) and the three-layer FGM (sample G in **Fig.3.4**) fabricated by HP and SPS over the temperature range from RT to 300 °C.

4.3.2 Analytical estimation of thermal conductivity

Numerous analytical and empirical models have been proposed to predict the macroscopic thermal conductivity properties of the heterogeneous medium, knowing the thermal conductivity and volume fraction of the constituents. These are known as effective medium theories (EMT) or effective medium approximations (EMA) which belong to the class of mean–field theories. These include the Maxwell model [85], the Rayleigh model [162], the Lewis–Nielsen model [88], the Woodside–Mesmer model [163], Bruggeman's general effective medium theory [164], the Hashin–Shtrikman bounds [165], Voigt's bounds [98], Reuss's bounds [99], the Hasselman–Johnson model [151], and more. In this study, the following well-known models were selected to analytically determine the effective thermal conductivity of composites with varying inclusion volume fractions.

1.   The Voigt and Reuss bounds

The Voigt and Reuss bounds based on the general rule of mixtures, provide the simplest estimates of effective material properties, yet they remain the most widely used. They apply a weighted average to provide the upper and lower bounds of a composite material's thermal conductivity. The Voigt bound is generally used to calculate the effective thermal conductivity when heat flows parallel to the layers (Eq. (4.1)), while the Reuss bound is used when heat flows perpendicular to the layers (Eq. (4.2)):

$$\lambda_{eff} = \frac{\lambda_m \lambda_c}{\lambda_m V_m + \lambda_c V_c}$$

$$(4.1)$$

$$\lambda_{eff} = V_m \lambda_m + V_c \lambda_c \qquad (4.2)$$

where V_m, V_c denote volume fraction of matrix, volume fraction of ceramic, while λ_m and λ_c stand for thermal conductivity of matrix and thermal conductivity of ceramic, respectively.

2.   The Hashin–Shtrikman bounds

Hashin and Shtrikman [165] formulated their bounds using variational principles of thermomechanics to derive the narrowest bounds for the effective thermal conductivity of materials, assuming homogeneity and isotropy. These bounds represent a significant improvement over earlier models such as the Voigt and Reuss bounds. The effective thermal conductivity for the lower and upper bounds are expressed as:

$$\lambda_{eff}^{lower\ bound} = \lambda_m + \left[\frac{V_c}{\left(\frac{1}{\lambda_c - \lambda_m}\right) + \left(\frac{3V_m}{3\lambda_m - 4G_m}\right)}\right] \quad (4.3)$$

$$\lambda_{eff}^{upper\ bound} = \lambda_c + \left[\frac{V_m}{\left(\frac{1}{\lambda_m - \lambda_c}\right) + \left(\frac{3V_c}{3\lambda_c - 4G_c}\right)}\right] \quad (4.4)$$

3. The self-consistent method

The self-consistent scheme approximates the effective thermal conductivity of a heterogeneous composite material when it is treated as a homogeneous equivalent medium. It assumes each phase in the composite is embedded in an effective medium whose thermal conductivity needs to be determined. This effective medium is considered self-consistent ensuring that the thermal behavior of each phase (e.g., heat conduction) matches the overall response of the composite when averaged over the entire material. Based on the assessment of the self-consistent approximation the evaluation of conductivity of particulate composite λ_{eff} is expressed as [166]:

$$\lambda_{eff} = \left[\frac{V_c(\lambda_c - \lambda_{eff})}{\lambda_c(\lambda_c + 2\lambda_{eff})}\right] + \left[\frac{V_m(\lambda_m - \lambda_{eff})}{\lambda_m(\lambda_c + 2\lambda_{eff})}\right] = 0 \quad (4.5)$$

The results derived from the analytical models basically do not account for porosity. The experimental thermal conductivities of the ungraded $AlSi12/Al_2O_3$ composites with 10, 20 and 30 vol.% Al_2O_3 fraction fabricated by HP lie between the Hashin–Shtrikman bounds. They are closer to the upper bound and the self-consistent estimate (see **Fig.4.11**). The experimental thermal conductivities of the ungraded $AlSi12/Al_2O_3$ composites with 10, 20 and 30 vol.% Al_2O_3 fabricated by SPS lie well within the Voigt–Reuss bounds. However, they are aligned with the Hashin–Shtrikman lower bound and deviate significantly from the self-consistent model (see **Fig.4.12**). This difference is primarily due to the higher porosity of the SPS samples compared to the HP samples, as shown in **Table 4.1**.
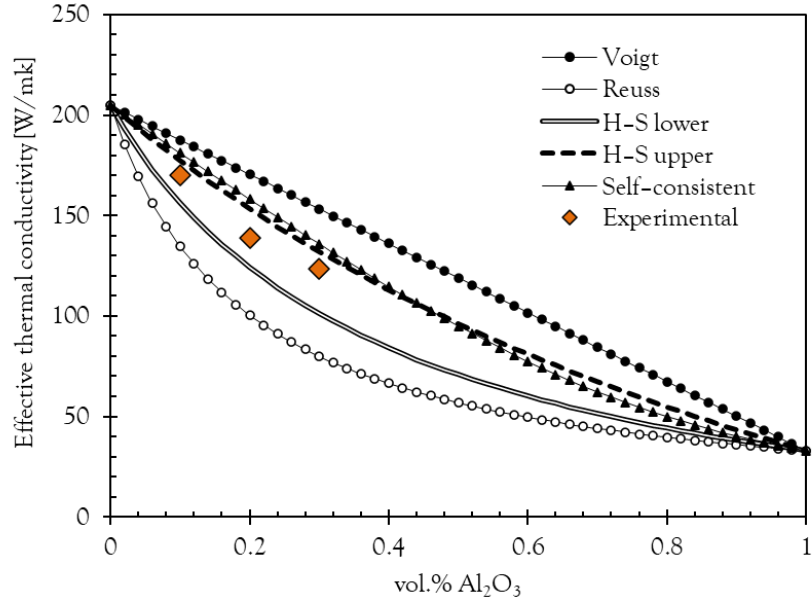
Fig.4.11 Comparison of the analytical approximations and experimental data of the effective thermal conductivity of ungraded AlSi12/Al$_2$O$_3$ composites with different Al$_2$O$_3$ volume fraction, fabricated by HP.
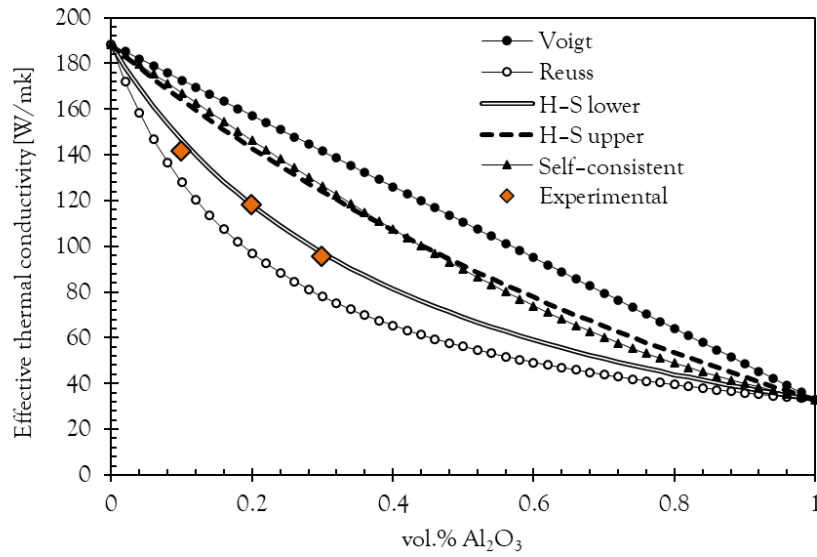
Fig.4.12 Comparison of the analytical approximations and experimental results of the effective thermal conductivity of ungraded AlSi12/Al$_2$O$_3$ composites with different Al$_2$O$_3$ volume fractions, fabricated by SPS.

For the analytical estimation of effective thermal conductivity of FGMs, the following models were considered.

4. The Mori–Tanaka method

The Mori–Tanaka method [167] is an analytical approach to predict the effective thermal conductivity by modeling a composite as a matrix containing multiple inclusions. It begins with a single spheroidal inclusion under far–field heat flow, then extends to multiple inclusions with perfect thermal contact. Orientation averaging is applied for randomly oriented inclusions, allowing the system to be approximated as one with equivalent spherical inclusions. This approach enables accurate estimation of effective thermal conductivity, even in complex, multidisperse systems. The effective thermal conductivity of multilayered materials can be evaluated as shown in the expression (4.6), [168]:

$$\lambda_{eff} = \lambda_c + (\lambda_m - \lambda_c) + \left[\frac{V_m}{1 + V_c + \left(\frac{\lambda_m - \lambda_c}{3\lambda_c} \right)} \right] \qquad (4.6)$$

5. The Reuss approximation

The Reuss approximation [99] gives the simple analytical estimation of the thermal conductivity of layered composite structures, which assumes no interactions between adjacent layers. The maximum effective thermal conductivity was derived from the experimentally measured thermal conductivities of the individual layer materials. The formula for calculating the effective thermal conductivity of n layers arranged in series and oriented perpendicular to the thermal conductivity measurement direction is provided in the following equation:

$$\lambda_{eff} = \frac{t_{eff}}{\left[\frac{t_1}{\lambda_1} + \frac{t_2}{\lambda_2} + \frac{t_3}{\lambda_3} + \cdots + \frac{t_n}{\lambda_n} \right]} \qquad (4.7)$$

The comparison of the Mori-Tanaka method and the Reuss approximation of the effective thermal conductivity of the two–layer and three–layer AlSi12/Al$_2$O$_3$ FGMs fabricated by HP and SPS with the experimental results is shown in **Fig.4.13** and **Fig.4.14**, respectively. It can be seen that the Reuss approximations align very well with the experimental data, both for the HP and SPS samples. Consequently, the Reuss model, which assumes composite layers connected in series, emerges as a reliable and efficient tool for approximating the thermal conductivity of layered FGMs.
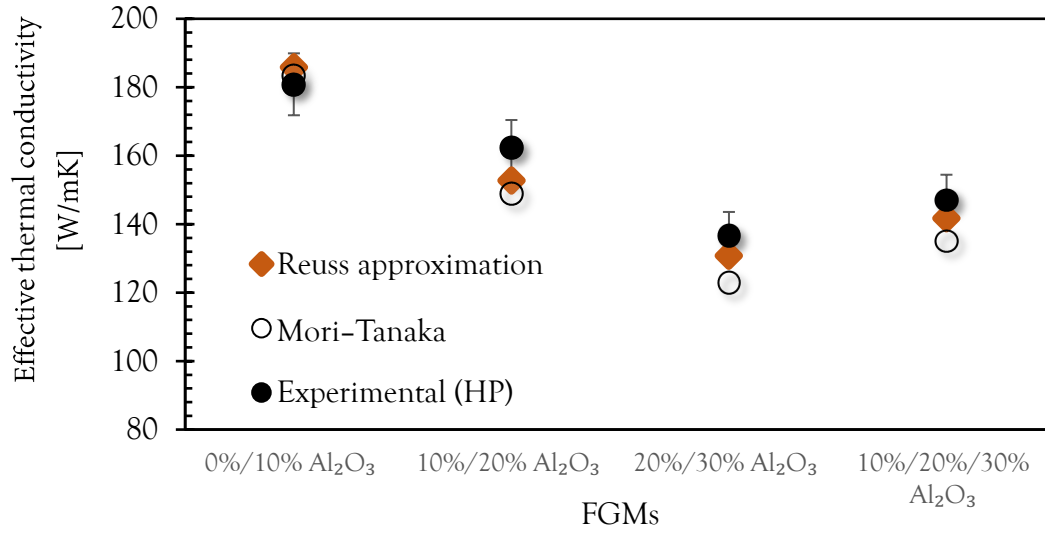
Fig.4.13 Comparison of the analytical approximations and experimental results of the effective thermal conductivity of two and three layer AlSi12/Al$_2$O$_3$ FGMs fabricated by HP, with different volume fractions of Al$_2$O$_3$ in each layer.
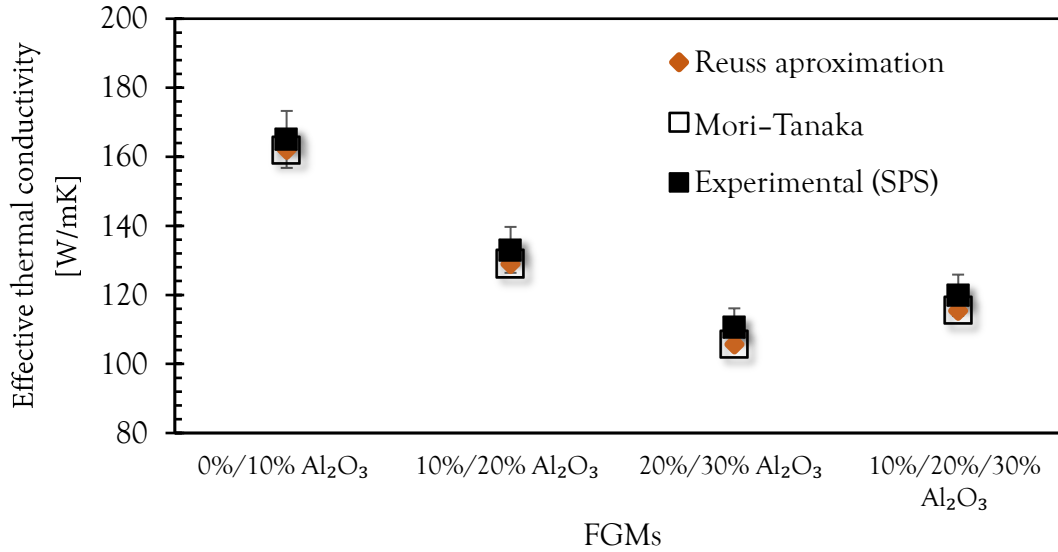
Fig.4.14 Comparison of the analytical approximations and experimental results of the effective thermal conductivity of two and three layer AlSi12/Al$_2$O$_3$ FGMs fabricated by SPS, with different volume fractions of Al$_2$O$_3$ in each layer.

4.3.3   Numerical evaluation of thermal conductivity

The thermal conductivity of the ungraded AlSi12+vAl$_2$O (v = 10, 20, 30 vol.%) composites and two and three–layer FGMs was evaluated numerically by FEM using micro–XCT images of the actual material microstructure to generate mesh models. The complete details on

mesh generation and numerical simulations are provided in Section 3.8. The micro–XCT–based FEM model was used to calculate the heat flux in each element. Both cubic and tetrahedral elements were employed to numerically analyze the effect of the element type on the effective thermal conductivity of the ungraded composites and the FGMs. From the graphical representation in **Fig.4.15**, the tetrahedral elements used in the FE model provide more accurate numerical results for λ_{eff} in both HP and SPS composites. Consequently, the cubic model was excluded from further simulations of the effective thermal conductivity. All subsequent numerical results presented in the following were derived from the tetrahedral mesh model.
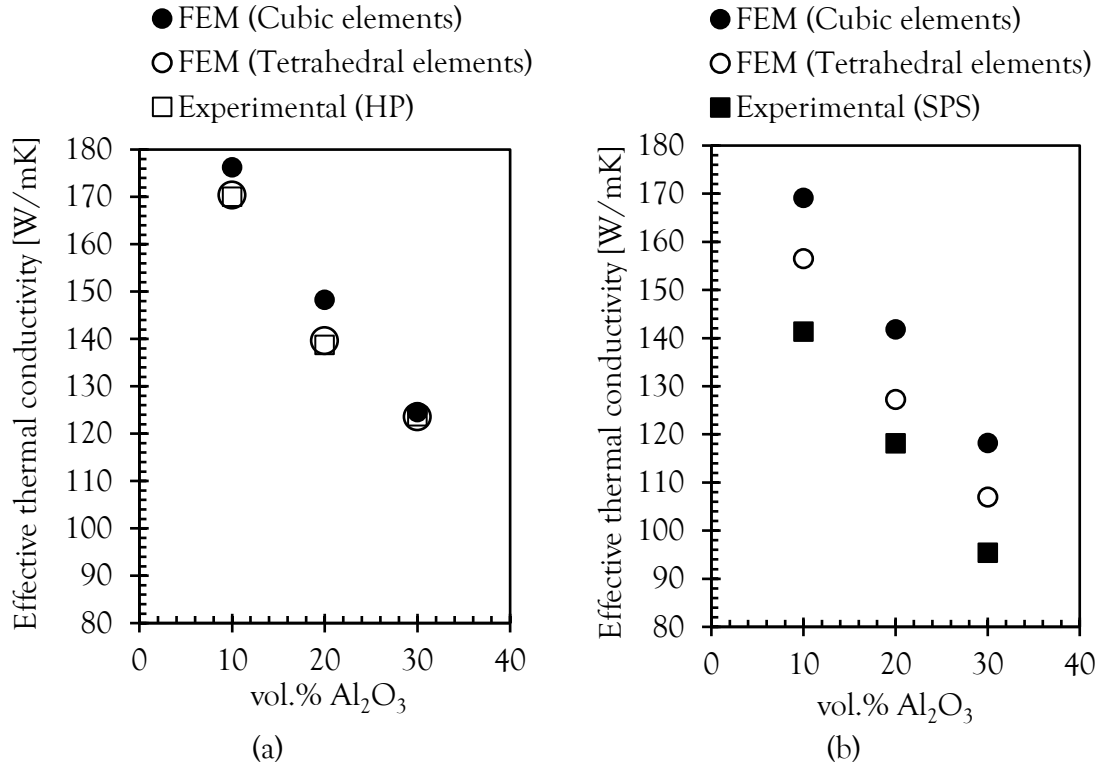
Fig.4.15 Comparison of the predictive capability of the cubic element vs. the tetrahedral element micro–XCT–based FEM models used to calculate the effective thermal conductivity of ungraded AlSi12/Al_2O_3 composite layers with different alumina volume fractions, fabricated by (a) HP and (b) SPS.

To accurately evaluate the thermal conductivity (TC), interfacial thermal conductance was considered at the interface between the matrix and the inclusions in the micro–XCT FEM model. Implementation of interfacial thermal conductance (h_c) in the FE model was explained in Section 3.8.3.

In the modeling, an interfacial thermal conductance value of 1.80×10^8 W/m^2K was used for the interface between Al and Al₂O₃, as reported in [169]. This value was obtained using interfacial conductance modal analysis (ICMA) and the atomistic Green's function (AGF) method. The results were validated by comparing them with experimental data from time–

domain thermoreflectance (TDTR) measurements [170, 171], as well as with predictions from the diffuse mismatch model (DMM) [172].

The comparison of the thermal conductivity obtained from the micro–XCT–based FEM model with the experimental data for the ungraded AlSi12+vAl$_2$O (v = 10, 20, 30 vol.%) composites is shown in **Fig.4.16**. For the two–layer and three–layer FGMs fabricated by HP and SPS the comparisons with the experimental data are shown in **Fig.4.17** and **Fig.4.18**, respectively. In the case of ungraded composites (**Fig 4.16**), the micro–XCT–based FEM model demonstrates exceptional accuracy in predicting the experimental data for all the samples, with a relative error of less than 4%. Also, for the two–layer and three–layer FGMs, a good agreement is observed between the numerical simulations and the experimental results, with a relative error of less than 6%. The error bars shown in **Fig.4.16**, **Fig.4.17** and **Fig.4.18** indicate a 5% margin of error, representing the uncertainty of measurements and precision of the instruments and used to measure thermal diffusivity by the flash method.
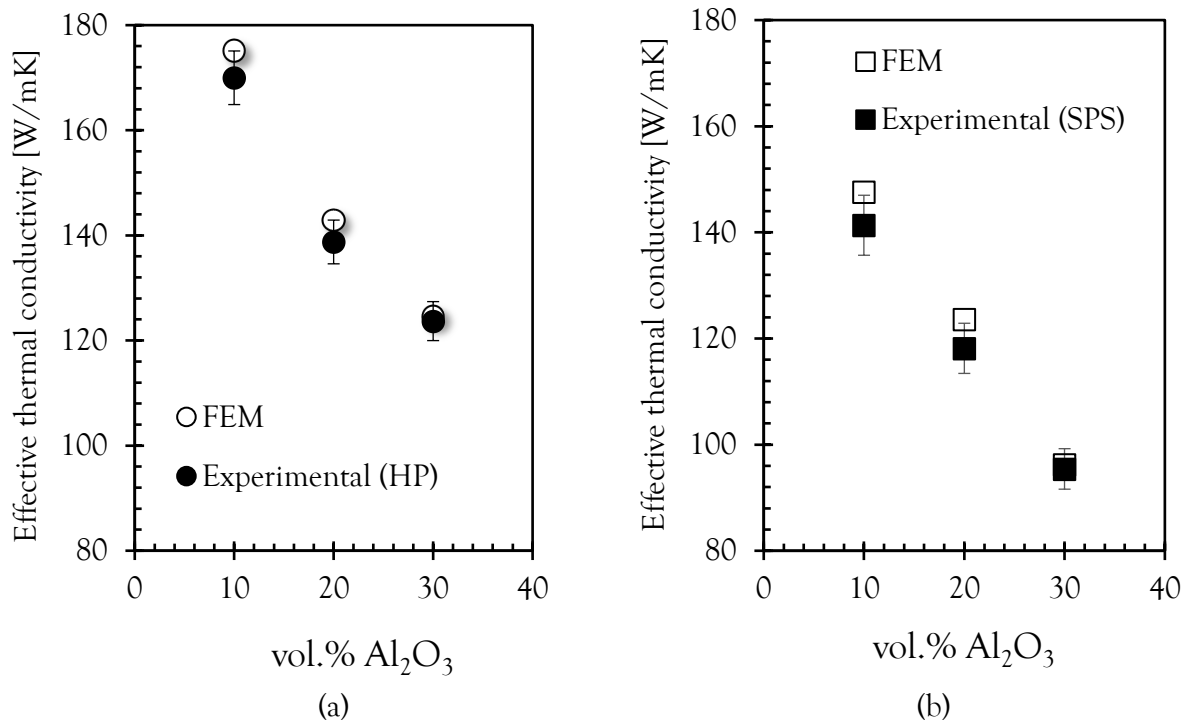
Fig.4.16 Comparison of the micro–XCT–based FEM model with the experimental results of the thermal conductivity at RT of AlSi12+vAl$_2$O (v = 10, 20, 30 vol.%) composites fabricated by (**a**) HP and (**b**) SPS.
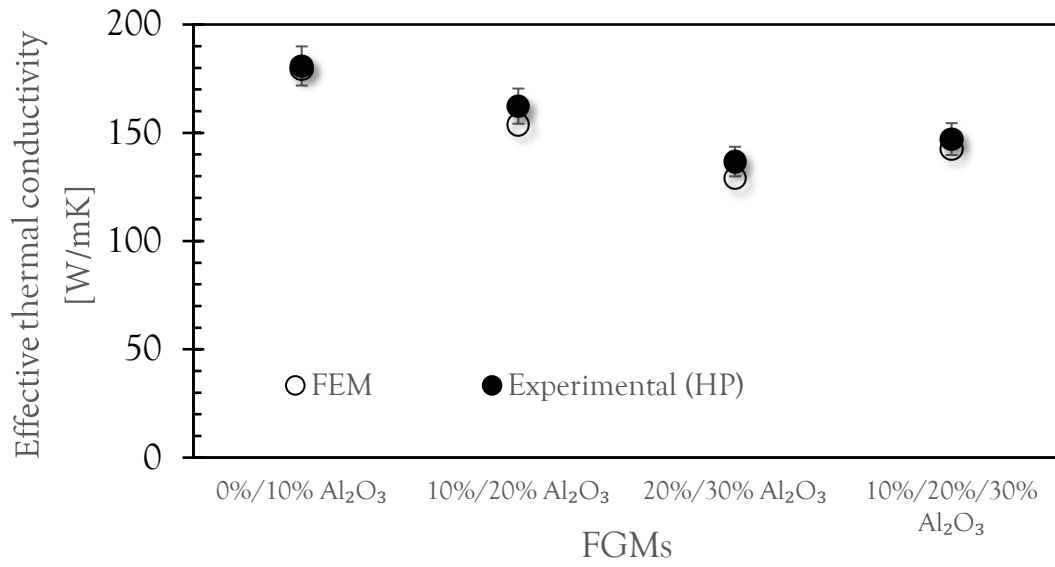
Fig.4.17 Comparison of the thermal conductivity at RT obtained from the micro–XCT–based FEM model with the experimental data for the two–layer and three–layer AlSi12/Al$_2$O$_3$ FGMs produced by HP.
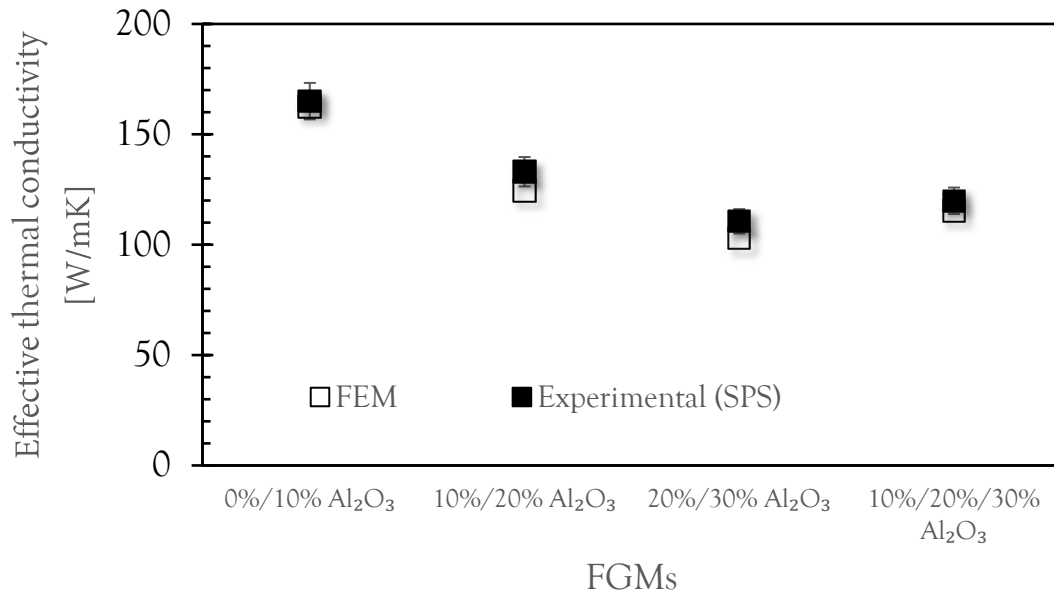
Fig.4.18 A comparison of the thermal conductivity at RT obtained from the micro–XCT–based FEM model with the experimental data for the two–layer and three–layer AlSi12/Al$_2$O$_3$ FGMs produced by SPS.

4.4 Thermal residual stresses in AlSi12/Al$_2$O$_3$ composites and FGMs

4.4.1 Measurement of thermal residual stresses

The samples used for measurement of the thermal residual stresses (TRS) were the ungraded AlSi12+vAl$_2$O$_3$ (v = 10, 20, 30 vol.%) composites and the three–layer FGM (AlSi12+10%Al$_2$O$_3$/AlSi12+20%Al$_2$O$_3$/AlSi12+30%Al$_2$O$_3$). Neutron diffraction (ND) was used to evaluate the TRS. The measurements were conducted at the Paul Scherrer Institute (PSI), Villigen, Switzerland. The TRS generated during the cooling phase of the HP or SPS sintering process were primarily due to the mismatch in the coefficients of thermal expansion (CTE) between the metal and ceramic. The coefficients of thermal expansion (CTE) of metal matrix (AlSi12) and ceramic reinforcement (Al$_2$O$_3$) are listed in **Table 3.6**.

The results of the TRS measurements in the ungraded composites and FGM are depicted in **Fig.4.19** as average stresses for (a) the metal matrix (AlSi12), and (b) Al$_2$O$_3$ reinforcement. In the case of the FGM, each TRS data point in **Fig.4.19 a–b** represents the average stress within a particular layer of the graded structure. The measurements indicate that the average stresses in the reinforcing phase (Al$_2$O$_3$) are compressive (negative sign), while the stresses in the AlSi12 matrix are tensile (positive sign). The data for the Al$_2$O$_3$ phase in the ungraded composites and FGMs with 10 vol.% Al$_2$O$_3$ content are not included due to the poor quality of the Bragg peaks in this case caused by the low ceramic phase content.
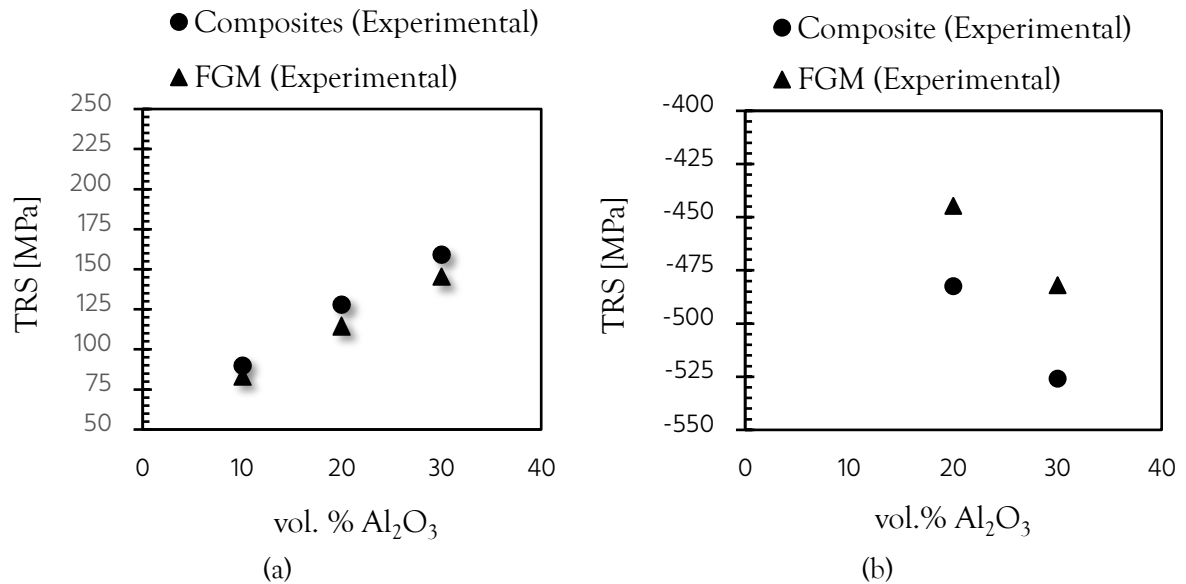
Fig.4.19 The average TRS from the neutron diffraction measurements for: **(a)** the AlSi12 matrix in the ungraded AlSi12+vAl$_2$O$_3$ (v = 10, 20, 30 vol.%) composites and the three–layer FGM AlSi12+10%Al$_2$O$_3$/AlSi12+20%Al$_2$O$_3$/AlSi12+30%Al$_2$O$_3$; **(b)** the Al$_2$O$_3$ reinforcement in the ungraded AlSi12+vAl$_2$O$_3$ (v = 10, 20, 30 vol.%) composites and the FGM. The data points for the FGM (triangles) represent the average TRS in AlSi12 or Al$_2$O$_3$ in each layer of the FGM.

From the neutron diffraction measurements of TRS in AlSi12/Al$_2$O$_3$ composites and three-layer FGM, the following key observations can be made:

1. As the volume fraction of the ceramic particles (Al$_2$O$_3$) in the composites and FGM increases, the average tensile TRS in the metal matrix and the average compressive TRS in the ceramic reinforcement increase.

2. The average TRS in the layers of the FGM is lower than that of the corresponding ungraded composites with the same ceramic volume fraction. This trend is observed for both the AlSi12 matrix and the Al$_2$O$_3$ reinforcement.

3. The average TRS in the AlSi12 matrix demonstrates a nearly linear increase with the rising volume fraction of Al$_2$O$_3$ (10, 20, 30 vol.%) for both ungraded composites and the three-layer FGM.

4.4.2 Numerical evaluation of thermal residual stresses

The FE mesh models based on the actual microstructure of the materials obtained from micro-XCT were prepared for all the ungraded composites and the FGM in which the thermal residual stresses were measured by neutron diffraction. The size of the RVE was chosen to be 50 x 50 x 50 elements, which corresponds to a volume of 50 x 50 x 50 μm^3. The mesh models used for the composite materials and the three-layer FGM are shown in **Fig.4.20** and **Fig.4.21**, respectively. The thermal residual stresses in the ASi12 matrix and Al$_2$O$_3$ reinforcement were calculated for cooling from 500 °C to room temperature (20 °C). The side displacements and other constraints were assumed to replicate the conditions of the cooling process in the mold, as described in Subsection 3.1.2.2. The details of the TRS numerical modeling are presented in Section 3.8.4.

| AlSi12+10%Al$_2$O$_3$ | AlSi12+20%Al$_2$O$_3$ | AlSi12+30%Al$_2$O$_3$ |
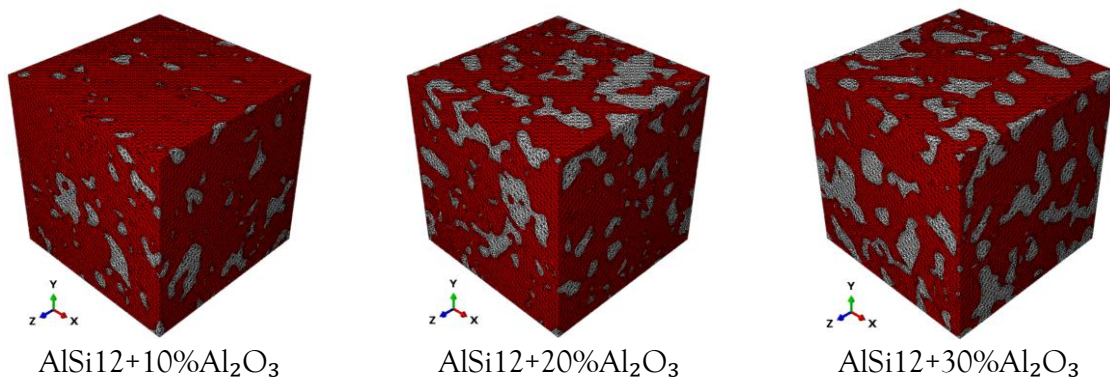
Fig.4.20 The micro-XCT-based FE meshes used in the numerical simulations of TRS in the ungraded composites AlSi12+vAl$_2$O$_3$ (v = 10, 20, 30 vol.%). Red represents the AlSi12 matrix, while white represents the reinforcing alumina grains.
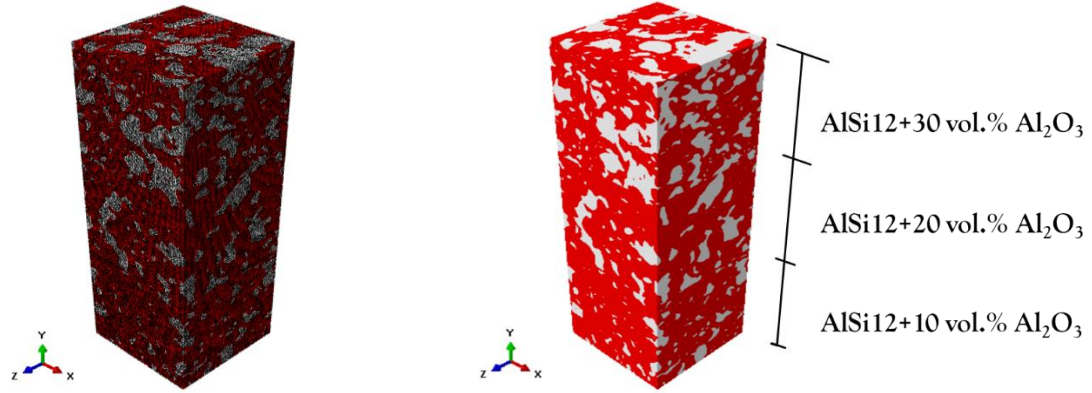
Fig.4.21 The micro–XCT–based FE mesh model used in the numerical simulations of TRS in the AlSi12 and Al_2O_3 phases of the AlSi12+10%Al_2O_3/AlSi12+20%Al_2O_3/AlSi12+30%Al_2O_3.) FGM. Red represents the AlSi12 matrix, while white represents the reinforcing Al_2O_3 grains.

A comparison between the TRS results obtained from the numerical model based on the actual material microstructure (micro-XCT-based FEM model) and the results from the neutron diffraction measurements shows that the model predicts the experimental TRS data with remarkable accuracy (see **Fig.4.22**). This confirms the efficacy of using micro–XCT images to create FE meshes in the numerical models of TRS behavior in the ungraded AlSi12/Al_2O_3 composites and the FGM. Analyzing the experimental results in **Fig.4.22 a–b**, it is evident that the average TRS in the FGM layers are approximately 10% lower than the residual stresses in the corresponding ungraded composites. It should be noted that the uncertainty of the neutron diffraction measurement was less than 5% for all the materials that were tested. Consequently, it can be concluded that, on a macroscopic level, the average TRS due to cooling in the graded composite was consistently lower than that in the ungraded bulk composite. The reduced thermal residual stress in the AlSi12/Al_2O_3 FGM compared to the corresponding ungraded composites offers significant advantages for the material's mechanical performance. Lower residual stresses can enhance key mechanical properties such as flexural strength and fracture toughness. This is achieved by minimizing the probability of stress–induced cracking, thus improving the material's ability to withstand mechanical loads. Furthermore, the mitigation of residual stress resulting from graded composite architecture is a notable benefit for potential applications of the AlSi12/Al_2O_3 composites in automotive brake discs, where materials are exposed to cyclic thermal and mechanical stresses.
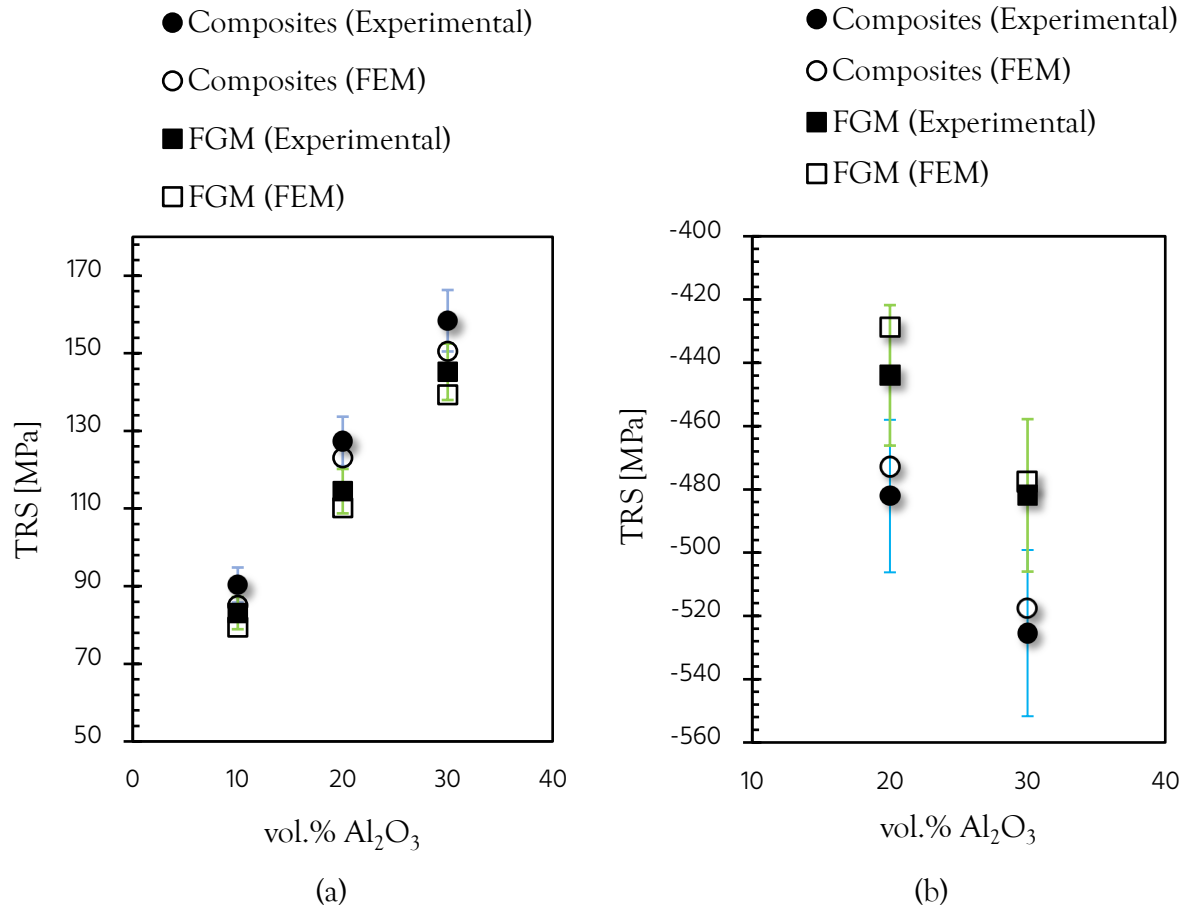
Fig.4.22 A comparison of the average thermal residual stress from the ND measurements with the micro–XCT–based FEM results for: **(a)** the AlSi12 matrix of ungraded composites AlSi12+vAl$_2$O$_3$ (v= 10, 20, 30 vol. %) and the FGM; **(b)** the Al$_2$O$_3$ reinforcement of the ungraded AlSi12+vAl$_2$O$_3$ (v= 20, 30 vol.%) composites and the FGM. The data for the 10 vol.% Al$_2$O$_3$ in figure (b) are not included due to the poor quality of the Bragg peaks caused by the low ceramic content.

RESULTS for AlSi12/SiC COMPOSITES and FGMs

5.1 Density measurements and porosity

Two fabrication programs were conducted to produce AlSi12/SiC samples for specific tests: one set for thermal conductivity measurements and another set for evaluating thermal residual stresses. The powder blends were consolidated using cylindrical graphite molds with different inner diameters adapted to the respective tests. To produce samples designated for thermal residual stress measurements, molds with an inner diameter of 33 mm were used, while for samples prepared for thermal conductivity measurements, molds of 20 mm inner diameter were taken. This variation of mold diameters was essential to ensure that the sample dimensions met the requirements of the corresponding measuring devices.

The relative density of the HP and SPS composite samples was evaluated using the Archimedes method (see Section 3.2). The theoretical density of the composites was determined using the density of AlSi12 = 2.656 g/cm^3, and the density of SiC = 3.21 g/cm^3 The latter was obtained from the measurements on pure SiC powder that was sintered in a hot press at 1450°C for one hour under 30 MPa, which resulted in a pore–free material. The theoretical density, measured density, relative density and porosity of AlSi12/SiC composites consolidated by HP for TRS measurements are listed in **Table 5.1**. The data for AlSi12/SiC composites consolidated by HP and SPS for the thermal conductivity measurements are displayed in **Table 5.2**.

Table 5.1 The relative density of AlSi12/SiC samples consolidated by HP (for TRS measurements).

Material	Theoretical density [g/cm^3]	Measured density [g/cm^3]	Relative density [%]	Porosity [%]
AlSi12+10 vol.% SiC	2.706	2.698	99.704	0.296
AlSi12+20 vol.% SiC	2.762	2.750	99.566	0.434
AlSi12+30 vol.% SiC	2.818	2.804	99.503	0.497

Table 5.2 The relative density of AlSi12/SiC samples consolidated by HP and SPS (for TC measurements).

Material	HP			SPS	
	Theoretical density [g/cm^3]	Measured density [g/cm^3]	Relative density [%]	Measured density [g/cm^3]	Relative density [%]
AlSi12+10 vol.% SiC	2.724	2.680	98.368	2.598	95.383
AlSi12+20 vol.% SiC	2.778	2.726	98.116	2.661	95.806
AlSi12+30 vol.% SiC	2.832	2.776	98.009	2.710	95.694

The relative density of the hot–pressed samples fabricated in 33 mm diameter molds was above 99.5% (see **Table 5.1**). This achievement is due to the well–tuned hot–pressing (HP) parameters that facilitated flawless sintering. In contrast, the relative densities of the hot–pressed samples sintered using molds with a 20 mm inner diameter, which also contained 10, 20, and 30 vol.% SiC, were around 98%. This small difference between the two sets of samples is primarily due to slight variations in the HP process parameters caused by differing climate conditions and thermocouple calibration.

The relative densities of the SPS samples using molds with an inner diameter of 20 mm, containing 10, 20, and 30 vol.% SiC, were around 95.0%, which is significantly lower than the approximately 98% achieved by HP samples. This disparity is due to two reasons: (1) the insufficient densification of the AlSi12 and SiC powder blends during the SPS process, where the sintering temperature was set at 547 °C (lower than the HP sintering temperature of 560 °C), and (2) the SPS process employed a much higher heating rate of 70 °C/min compared to the slower rate of 5 °C/min used in HP. While the temperature of 547 °C was adequate for neck formation during the diffusion process between the soft metal particles (AlSi12), it was insufficient to complete the expected bonding between the metal and hard ceramic (SiC) particles. This limitation arises from the significant difference in melting temperatures between these materials: AlSi12 has a melting point of approximately 590 °C, as confirmed by differential scanning calorimetry (DSC) measurements on the AlSi12 powder, while SiC has a much higher melting temperature exceeding 2,830 °C [125]. It is interesting to note that, despite the SPS process employing a higher pressure of 40 MPa compared to the 30 MPa used in the HP method, the resulting composites with 10, 20, and 30 vol.% SiC exhibited lower relative densities than their HP–processed counterparts (see **Table 5.2**).

5.2 Microstructure analysis

5.2.1 SEM analysis

The microstructure of ungraded AlSi12+vSiC (v=10, 20, 30 vol.%) composites and the three-layer FGM was analyzed using scanning electron microscopy (SEM) and micro–computed tomography (micro–XCT). The methodology is described in Section 3.3. To enable thorough observation, samples were sectioned both parallel and perpendicular to gradient direction. This approach facilitated examination of the composite surface in the longitudinal section and observation of the gradient material' layered structure in the transverse section.

The SEM micrographs of the ungraded composites and FGMs fabricated by HP and SPS are shown in **Fig.5.1**. They reveal a homogeneous microstructure characterized by an even

distribution of ceramic grains (light phase) within the AlSi12 matrix (dark phase). The interface between the ceramic and metallic phases exhibits coherent connections, indicating good bonding. Some protrusions are visible on the surface, which are attributed to scratches on the AlSi12 matrix caused during the polishing process in preparation for SEM analysis. Few micro pores and cracks are observed in both HP and SPS samples.

The seamless transition between the composite layers in the FGMs shown in **Fig.5.2** and **Fig.5.4** which occurs during the sintering of the FGMs, accounts for the development of a metallurgical bond. This bond ensures structural integrity between layers that have stepwise graded ceramic (SiC) content in the continuous matrix (AlSi12).

(a) AlSi12+10%SiC

(b) AlSi12+20%SiC
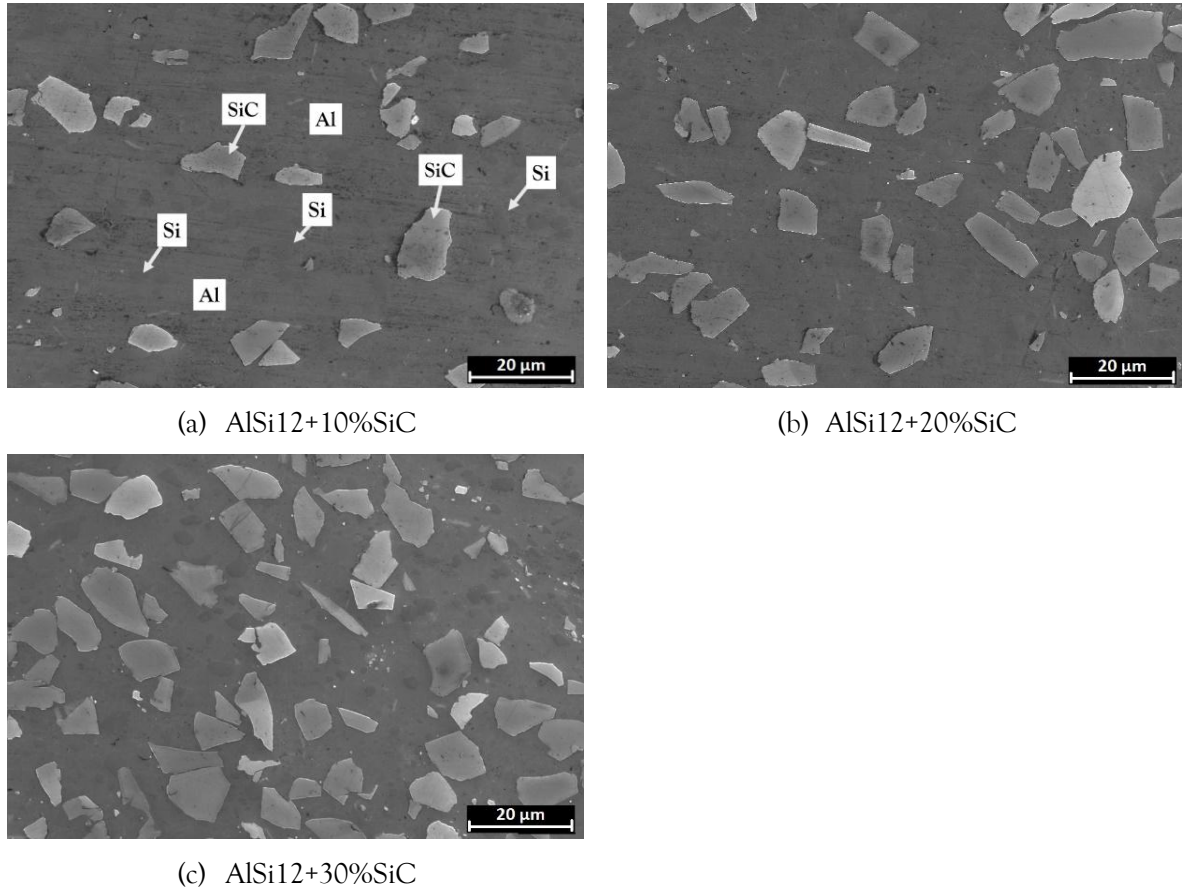
(c) AlSi12+30%SiC

Fig.5.1 SEM micrographs of the etched surface of the ungraded AlSi12/SiC samples sintered by HP: **(a)** AlSi12+10%SiC, **(b)** AlSi12+20%SiC, **(c)** AlSi12+30%SiC.

(a)

(b)

(c)
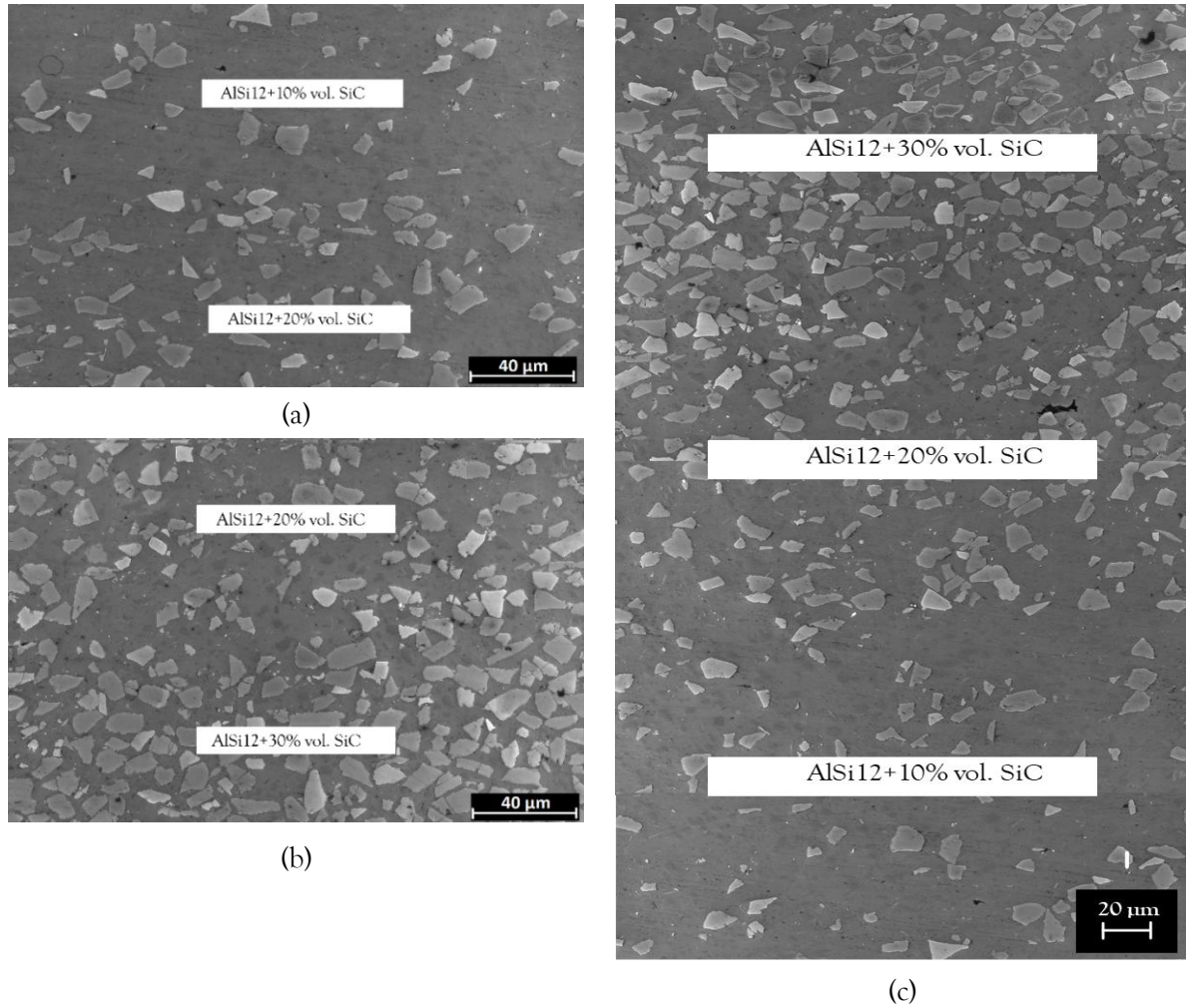
Fig.5.2 SEM micrographs of the interlayer regions in the HP–consolidated two–layer and three–layer AlSi12/SiC FGMs: (**a**) AlSi12+10%SiC/AlSi12+20%SiC, (**b**) AlSi12+20%SiC/AlSi12+30%SiC, and (**c**) AlSi12+10%SiC/AlSi12+20%SiC/AlSi12+30%SiC.

(a) AlSi12+10%SiC   (b) AlSi12+20%SiC
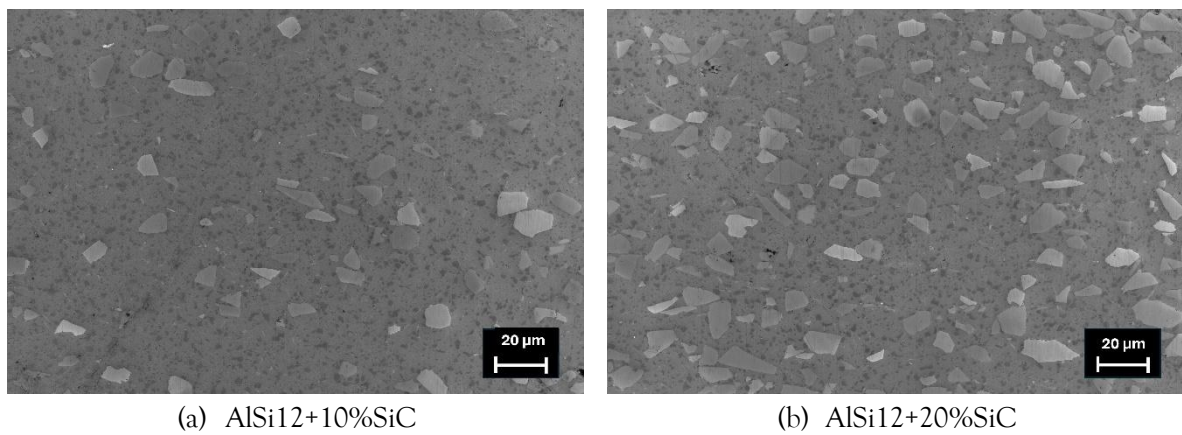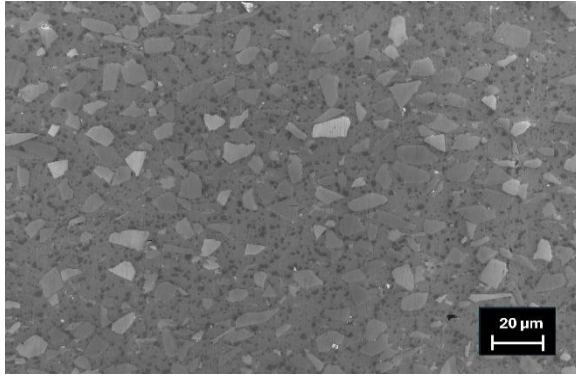
(c) AlSi12+30%SiC

Fig.5.3 SEM micrographs of the etched surface of the ungraded AlSi12/SiC samples sintered by SPS: **(a)** AlSi12+10%SiC, **(b)** AlSi12+20%SiC, **(c)** AlSi12+30%SiC.
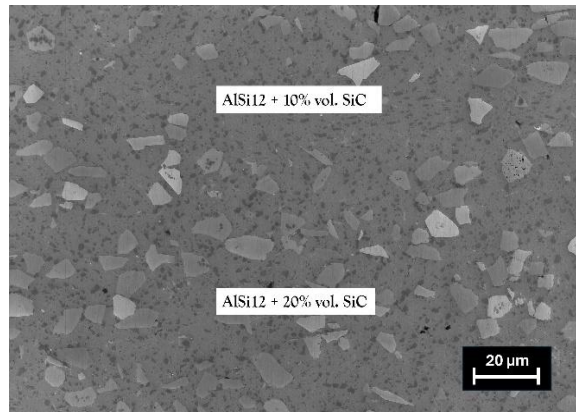
(a)
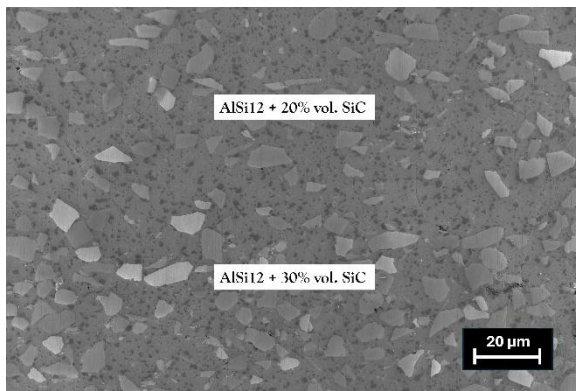
(b)
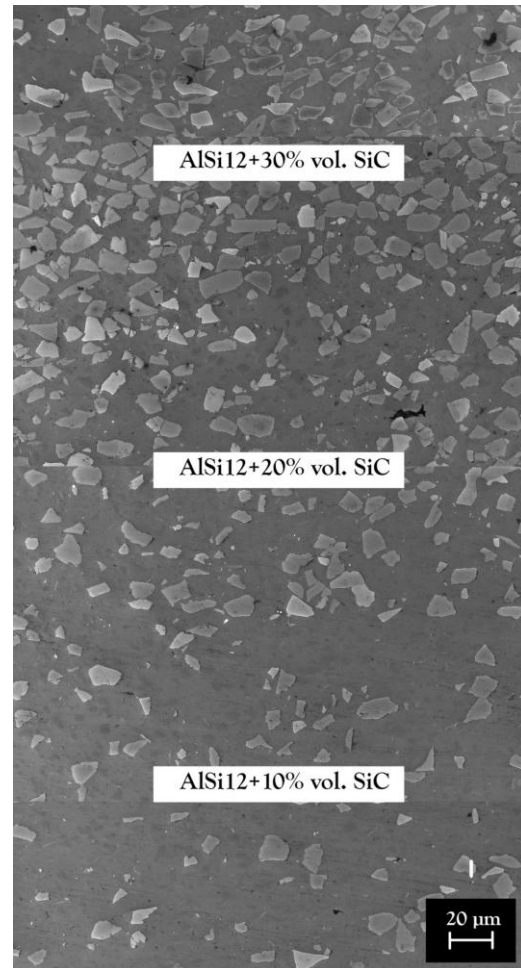
(c)

Fig.5.4 SEM micrographs of the interlayer regions in the SPS–consolidated two–layer and three–layer AlSi12/SiC FGMs: **(a)** AlSi12+10%SiC/AlSi12+20%SiC, **(b)** AlSi12+20%SiC/AlSi12+30%SiC, and **(c)** AlSi12+10%SiC/AlSi12+20%SiC/AlSi12+30%SiC.

5.2.2 XRD and TEM analysis

A phase composition analysis of the composite containing 30 vol.% SiC was conducted using X-ray diffraction (XRD). The analysis revealed the presence of the following phases: Al, Si, Al_2O_3, and Al_4C_3. (see **Fig. 5.5**). The most intense diffraction peaks corresponded to Al, Si, and SiC. The peaks corresponding to Al_2O_3 and Al_4C_3 matched those reported in the literature, indicating their possible presence at the interfaces between the Al–Si and AlSi–SiC phases. However, due to the limitations inherent in the XRD dataset, the formation of these compounds could not be definitively confirmed. Therefore, the TEM experiments were needed to get a conclusive identification of compounds present.
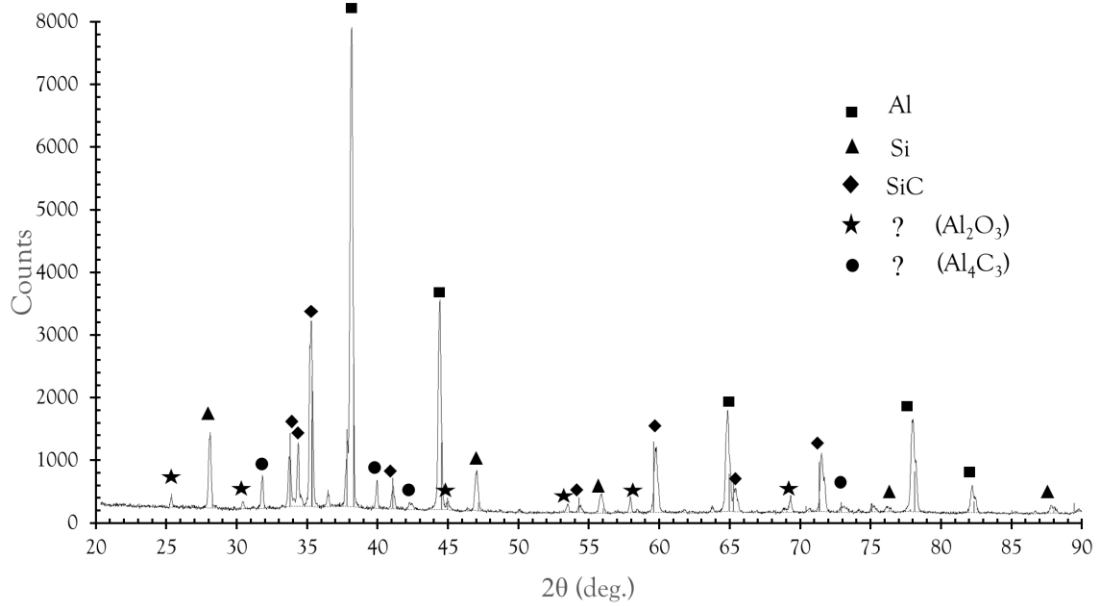
Fig.5.5 XRD spectrum for AlSi12+30 vol.% SiC fabricated by hot pressing with possible peaks of Al_2O_3 and Al_4C_3 (to be confirmed by TEM).

In the SPS process, oxides and carbides form due to local temperature increases caused by sparks hitting the particle surfaces and the heat released from allotropic phase transformations of Al_2O_3, where it changes from one crystal structure to another at high temperatures [42]. According to the results of the TEM analysis, a thin layer of alumina is present in the microstructure of the AlSi12+30 vol.% SiC that was fabricated by HP. These are primarily located at the aluminum grain boundaries and also at the interface of Al and SiC (see **Fig. 5.6**).
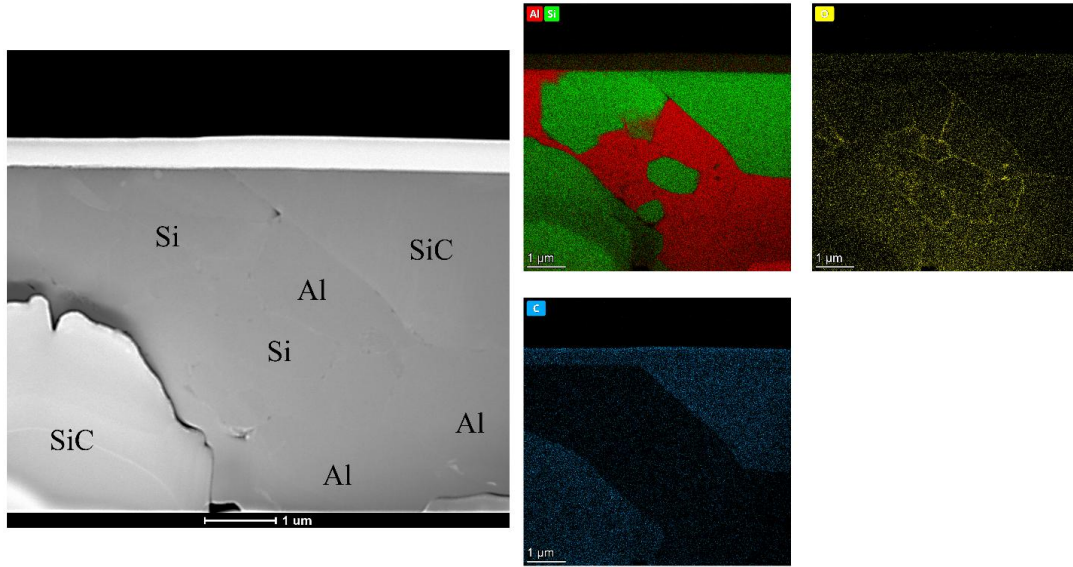
Fig.5.6 TEM micrograph of AlSi12+30 vol.% SiC and EDS elemental maps showing the distribution of Al, Si, C, and O.

The composition of the thin layer of oxide has been analyzed in detail. **Figure 5.7** illustrates the microstructure featuring a Al_2O_3 thin layer ($\approx$20 nm), accompanied by EDS mapping and area–specific elemental analysis to reveal its composition.
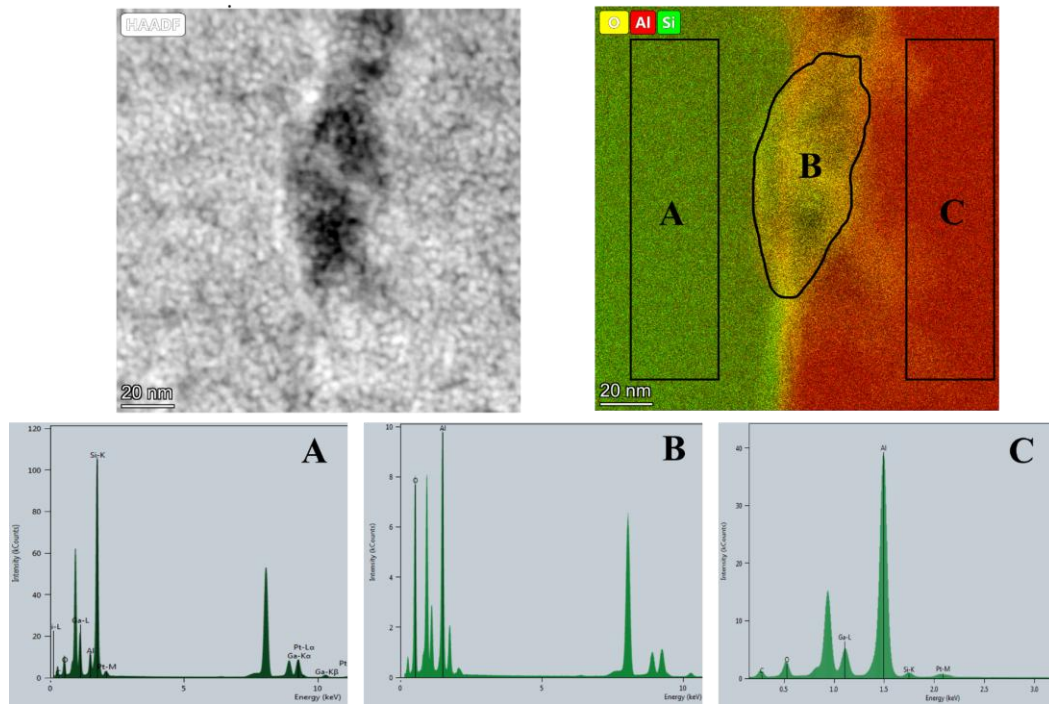
Fig.5.7 TEM image, EDX elemental maps, and spot analyses of the Al_2O_3 layer in the AlSi12+30% SiC composite. Spectra (A), (B), and (C) correspond to EDX area analyses conducted in zones A, B, and C, respectively.

Important conclusions can be drawn from this analysis:

1. A higher content of Al and O in the selected area B (**Fig.5.7**) confirms the presence of the oxide layer (Al_2O_3). This is evident from the EDS map and EDX area B. This finding aligns with earlier studies on the composites produced via hot pressing of Al–SiC nanocomposites [51].

2. The presence of an oxide layer (Al_2O_3) surrounding the aluminum (Al) grains and at the interface between aluminum (Al) and silicon carbide (SiC) is evident, as indicated by the yellow color in **Fig.5.6.**

3. There was no silicon (Si) in the aluminum (Al) grains (area C in **Fig.5.7**) and no aluminum (Al) in the silicon (Si) grains (area A in **Fig.5.7**).

4. No indication of aluminum carbide (Al_4C_3) was observed through the TEM analysis.

5.3 Thermal conductivity of AlSi12/SiC composites and FGM

5.3.1 Experimental evaluation of thermal conductivity

Similarly as for $AlSi12/Al_2O_3$ composites, the thermal conductivity was determined from the measured thermal diffusivity, specific heat capacity, and the density of the fabricated ungraded composite samples and the FGMs. The detailed methodology is presented in Section 3.4. The thermal conductivity measurements for ungraded AlSi12+vSiC (v = 10, 20, 30 vol.%) composites and three–layer FGM, obtained using the flash method in the temperature range from RT to 500 °C, are summarized in **Table 5.3**.

The experimentally determined thermal conductivities of AlSi12 and SiC are 204.8 W/mK and 240 W/mK, respectively. Therefore, according to the rule of mixtures (ROM), the thermal conductivity of AlSi12/SiC composites was expected to increase with the volume fraction of SiC. However, contrary to this expectation, the experimental results revealed a decreasing trend in thermal conductivity with increasing SiC content. Similar observations have been reported by other researchers [46,52,173,174]. As illustrated in **Fig.5.8**, an increase in SiC volume fraction – 10% in sample A, 20% in sample B, and 30% in sample C – corresponds to a decrease in thermal conductivity of the composite. This trend is consistent for both HP and SPS samples across the full temperature range, with a more pronounced effect at higher temperatures.

Table 5.3 Thermal conductivity (λ) measurements of the HP and SPS sintered ungraded AlSi12+vSiC (v = 10, 20, 30 vol.%) composites and three–layer FGM in the temperature range of 25 °C (RT) –500 °C. Sample labels (A, B, C, G) denote: sample A (AlSi12+10%SiC), sample B (AlSi12+20%SiC), sample C (AlSi12+30%SiC), sample G (three–layer FGM AlSi12+10%SiC/AlSi12+20%SiC/AlSi12+30%SiC).

T [°C]	Thermal conductivity of HP samples, λ [W/mK]			
	Ungraded composites			Three–layer FGM
	Sample A	Sample B	Sample C	Sample G
25	178.140	129.336	120.517	141.653
50	174.760	129.852	119.612	141.381
100	168.002	130.954	115.564	137.063
150	160.728	129.967	112.474	136.327
200	157.204	128.521	108.566	132.627
250	152.033	127.853	105.837	129.282
300	147.595	126.426	102.513	128.730
350	144.701	124.373	100.175	125.696
400	140.348	122.759	97.578	121.942
450	135.814	119.495	94.366	120.461
500	131.813	115.297	91.925	116.166
T [°C]	Thermal conductivity of SPS samples, λ [W/mK]			
25	153.523	148.469	137.206	142.757
50	154.009	147.180	135.813	142.268
100	152.610	144.182	132.648	139.226
150	151.844	142.169	128.238	137.589
200	149.007	139.213	125.205	134.794
250	148.404	136.315	121.423	132.042
300	147.139	135.235	118.818	131.271
350	146.768	132.654	117.376	128.378
400	143.980	129.902	114.185	124.371
450	140.536	127.572	110.765	123.124
500	137.535	123.632	108.363	119.073
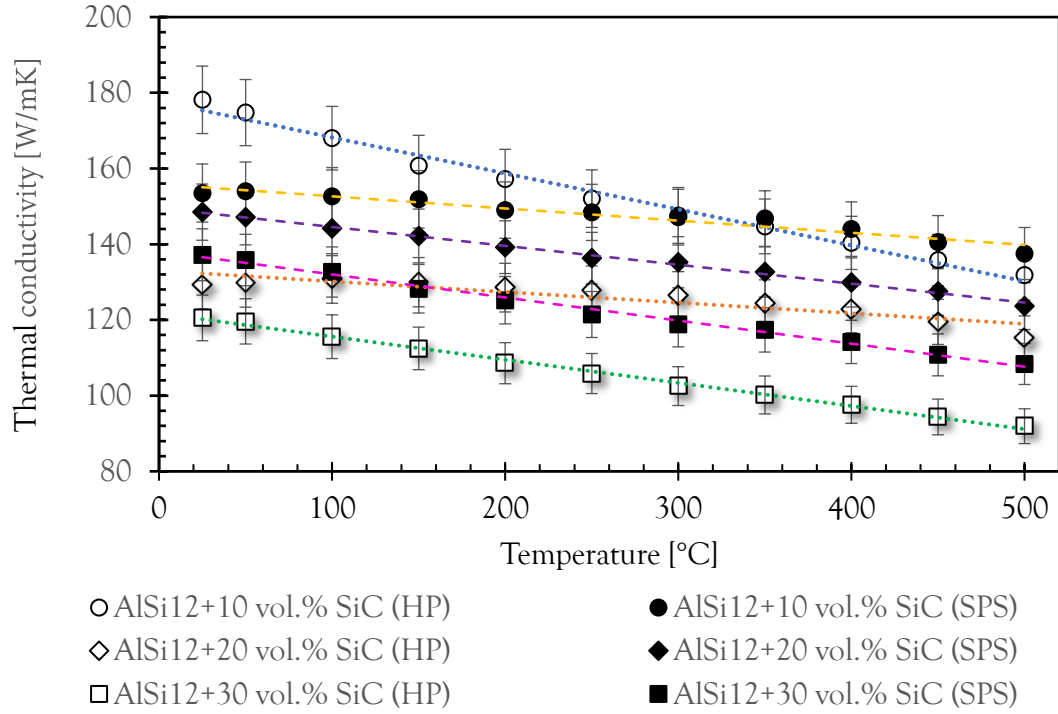
Fig.5.8 Results of thermal conductivity measurements for the ungraded composites AlSi12 +vSiC (v = 10, 20, 30 vol.%) fabricated by HP and SPS, in the temperature range RT to 500°C.

The reduction in thermal conductivity can be primarily attributed to the following factors:

1. The presence of residual porosity of approximately 5% for SPS and 2% for HP (see Section 5.1) acts as a thermal insulator and increases the overall thermal resistance of the composite.

2. Thin aluminum oxide (Al_2O_3) layers are observed around the grain boundaries of the aluminum matrix and on the surfaces of the dispersed SiC particles. These layers form during the composite fabrication process due to oxidation, and their presence was confirmed by TEM analysis (refer to Section 5.2.2). These oxide films act as thermal barriers, impeding efficient heat transfer across grain boundaries thus reducing the thermal conductivity.

It is noteworthy that for the three-layer FGMs (sample G in **Table 5.3**) fabricated using both the HP and SPS methods, the thermal conductivity results are highly comparable for the HP and SPS samples over the entire temperature range RT–500 °C (see **Fig.5.9**).
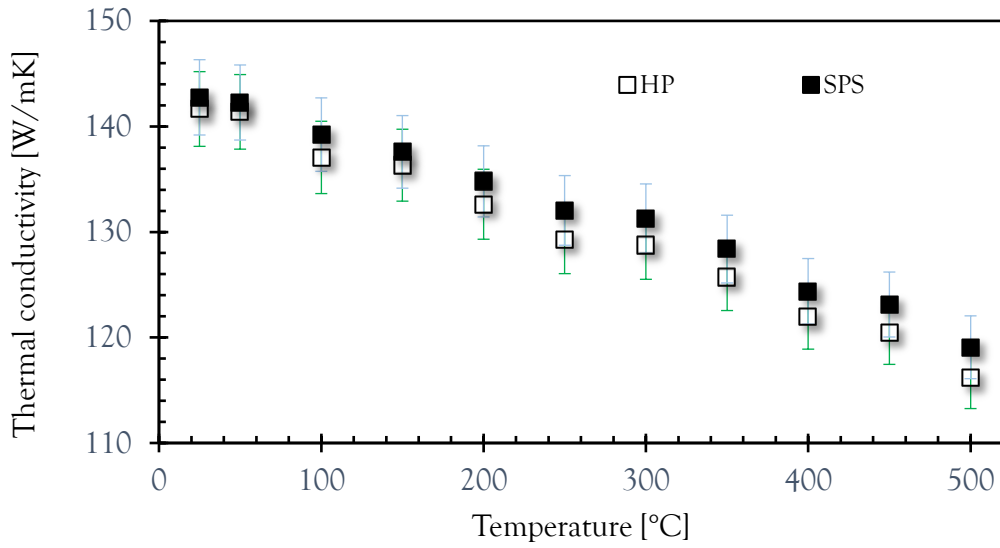
Fig.5.9 Results of thermal conductivity measurements for the three–layer FGMs (samples G in Table 5.3) fabricated by HP and SPS in the temperature range from RT to 500°C.

5.3.2   Analytical estimation of thermal conductivity of AlSi12/SiC three–layer FGM

For the analytical estimation of thermal conductivity of the three–layer FGM (AlSi12+10%SiC/AlSi12+20%SiC/AlSi12+30%SiC), the Reuss approximation was used. The results for the FGM samples sintered by HP and SPS are presented in **Fig.5.10** and **Fig.5.11**, respectively.
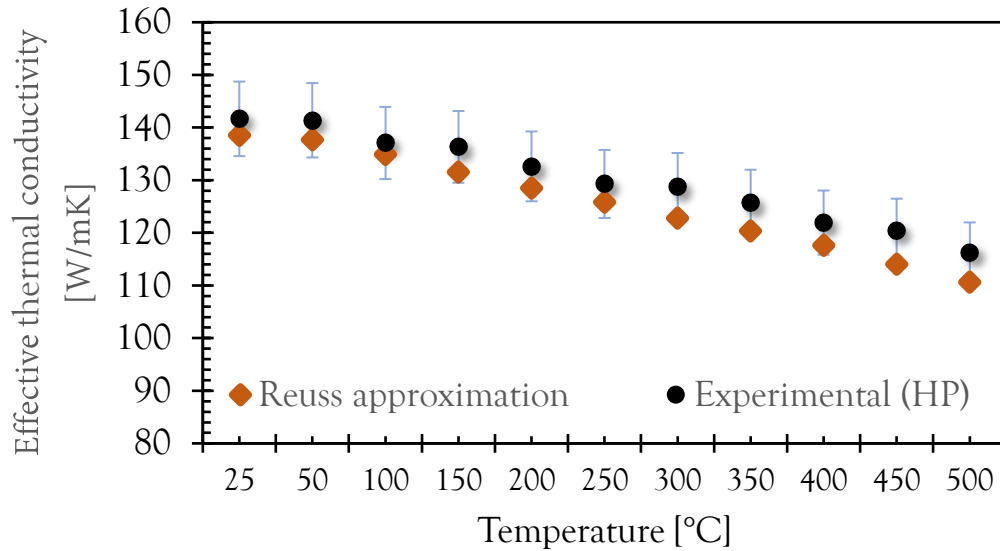
Fig.5.10 Comparison of the Reuss approximations with experimental results of the effective thermal conductivity of three–layer AlSi12/SiC FGM fabricated by HP.

93
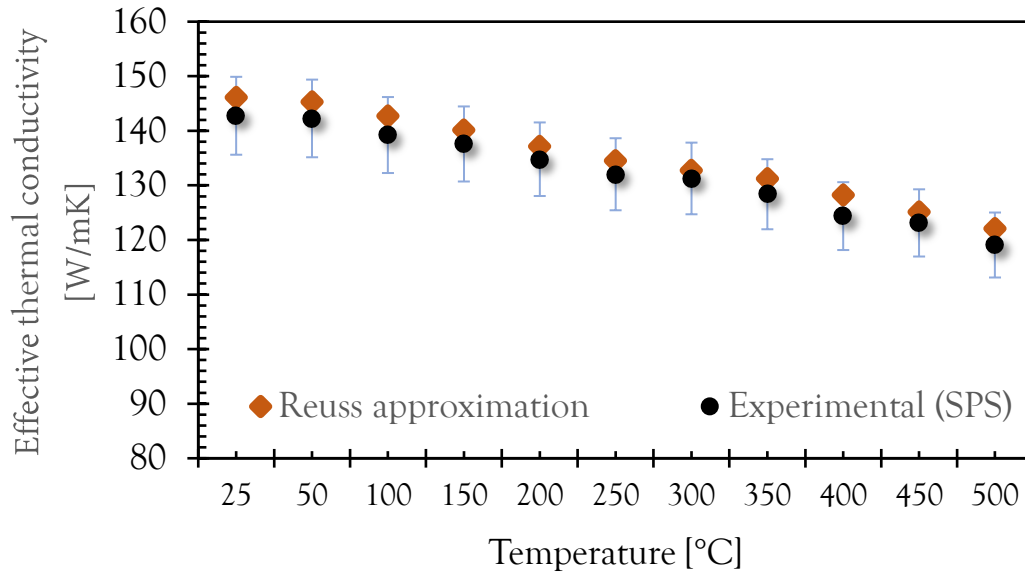
Fig.5.11 Comparison of the Reuss approximations and experimental results of the effective thermal conductivity of three-layer AlSi12/SiC FGM fabricated by SPS.

It is observed that the Reuss approximation of the effective thermal conductivity of AlSi12/SiC three-layer FGM fabricated by both HP and SPS was very close to the results obtained from the experimental measurements by the flash method. Therefore, it can be concluded that the Reuss approximation provides a quick and precise estimation of the effective thermal conductivity of the FGMs examined in this thesis.

5.3.3   Numerical evaluation of thermal conductivity

Modeling of the thermal conductivity of the AlSi12/SiC composites and FGMs was performed mainly to investigate the influence of interfacial thermal resistance caused by the Al_2O_3 layers surrounding the AlSi12 and SiC grains on the overall thermal conductivity. This was achieved by comparing two models: one that accounted for the interfacial thermal resistance offered by the Al_2O_3 layers (see **Fig.5.12 (b)**), and another that did not consider any thermal resistance at the AlSi12–SiC interface (see **Fig.5.12 (a)**).

It is recalled that a thin film of Al_2O_3 surrounding the AlSi12 and SiC grains in the AlSi12/SiC microstructure was identified through TEM analysis; however, these films were too thin to be captured by micro–XCT. To account for these layers, contact interfaces were defined between AlSi12 and SiC, with the contact thickness proportional to the Al_2O_3 film thickness of about 10 nm (refer to **Fig.5.7**). An appropriate interfacial thermal conductance value of 38.46 MW/m²K [175], measured using a transient thermoreflectance technique, was assigned. Implementation of the interfacial thermal conductance (h_c) in the FE model is explained in Section 3.8.3.

94

<div align="center">(a)   (b)</div>
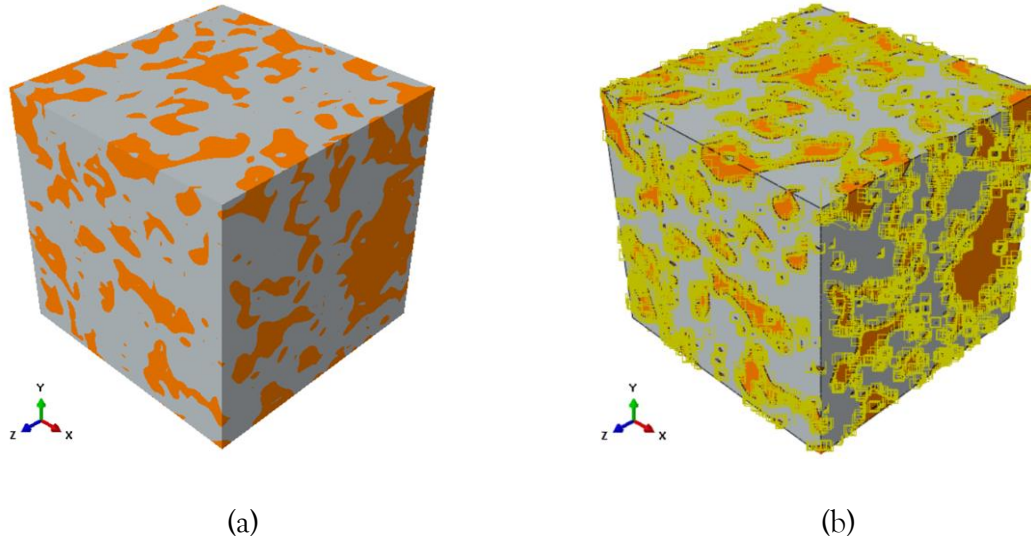
Fig.5.12 The micro–XCT FEM model of AlSi12+30vol.%SiC composite fabricated by HP: (a) with the interfacial thermal resistance at the at the AlSi12–SiC interface included; (b) without the interfacial thermal resistance.

Figure 5.13 presents a comparison of the results for the thermal conductivity at room temperature of the AlSi12/SiC composite samples fabricated by HP, obtained from the FEM model with and without the interfacial thermal resistance (ITR) accounted for, with the experimental measurements by the flash method. The same comparison for the AlSi12/SiC composite samples fabricated by HP is plotted in **Fig.5.14**.

As shown in **Fig.5.13** and **Fig.5.14**, the FEM model, which does not consider the interfacial thermal resistance of the Al_2O_3 layer at the SiC grains, generates results that significantly deviate from the experimental data and demonstrates an increasing trend as the SiC content rises, which contradicts the experimentally observed trend. In contrast, the FEM model which accounts for the interfacial thermal resistance of the Al_2O_3 layer, shows a declining trend in thermal conductivity with increasing SiC content, and closely matches the experimental data for 10, 20 and 30 vol% of SiC. This indicates that the interfacial thermal resistance of the Al_2O_3 layer plays a significant role in limiting the heat transfer. This trend also holds true for the three–layer FGM (refer to **Fig.5.15**) where interfacial thermal resistance is a key factor influencing thermal conductivity.
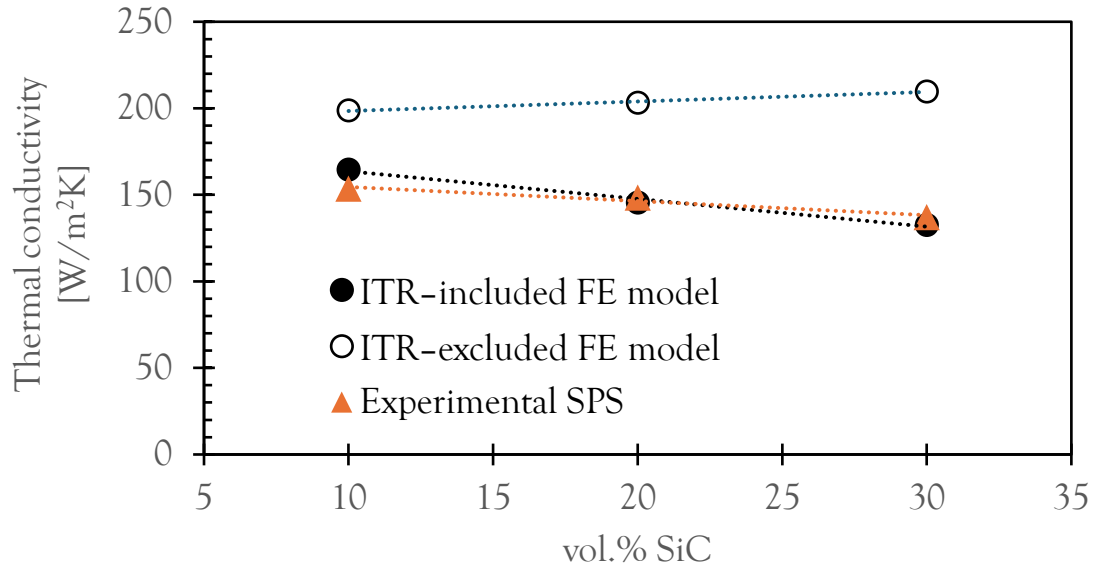
Fig.5.13 Influence of the interfacial thermal resistance (ITR) of the Al₂O₃ layer on the thermal conductivity at room temperature (RT) of the AlSi12/SiC composites fabricated by SPS as a function of the SiC volume fraction.
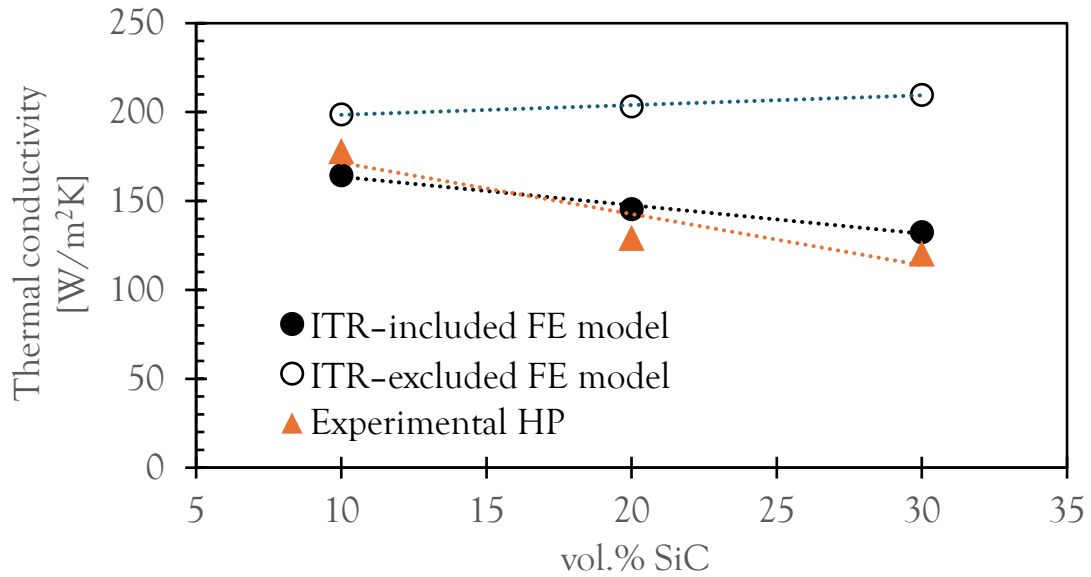
Fig.5.14 The influence of interfacial thermal resistance (ITR) of the Al₂O₃ layer on the thermal conductivity at RT of the AlSi12/SiC composites fabricated by HP as a function of the SiC volume fraction.
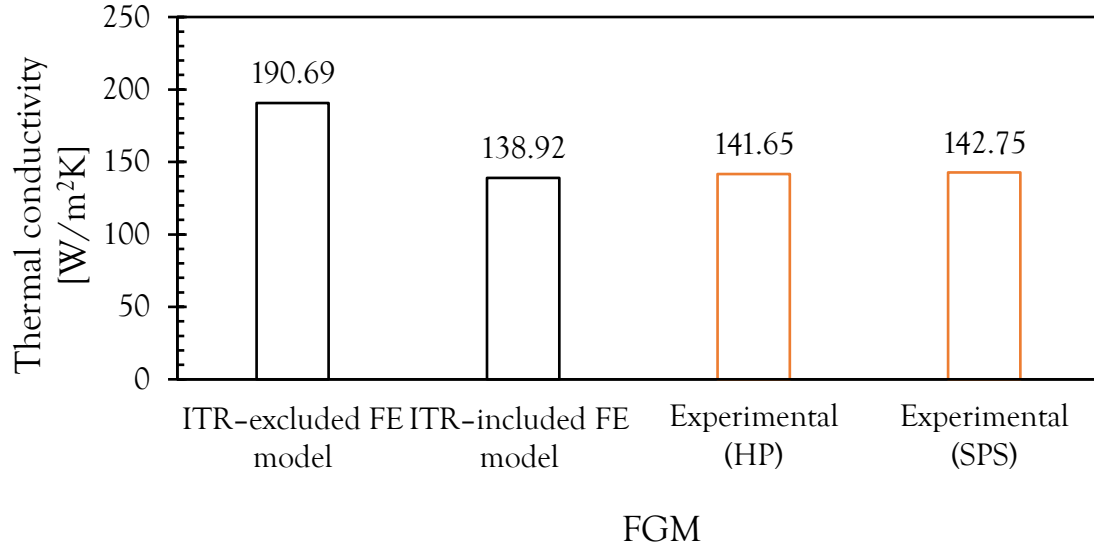
Fig.5.15 The influence of the interfacial thermal resistance (ITR) of the Al$_2$O$_3$ layer on the thermal conductivity at RT of the AlSi12/SiC three-layer FGMs produced by HP and SPS.

5.4 Thermal residual stresses in AlSi12/SiC composites and FGMs

5.4.1 Measurement of thermal residual stresses

To assess thermal residual stresses in ungraded AlSi12+vSiC (v = 10, 20, 30 vol%) composites and the three-layer FGM, neutron diffraction (ND) measurements were conducted at the Paul Scherrer Institute (PSI) in Villigen, Switzerland.

The samples were fabricated by hot pressing at 560 °C, with a heating rate of 5 °C/min, applying 30 MPa pressure, and held for 3 hours. Samples were allowed to cool freely in the furnace from the sintering temperature (560 °C) to room temperature without any load. The resulting residual stress field during the cooling was primarily due to the mismatch in the coefficients of thermal expansion (CTE) between the AlSi12 and SiC. The coefficients of thermal expansion (CTE) of metal (AlSi12) and ceramic (SiC) are listed in **Table 3.6**.

The average residual stress from the ND measurements in the ungraded composites and FGM are depicted in **Fig.5.16** for (a) the AlSi12 matrix, and (b) SiC reinforcement. For the FGM, each TRS data point in **Fig.5.16 a–b** represents the average stress within a particular layer of the graded structure. Similarly as in AlSi12/Al$_2$O$_3$ composites and FGMs, the average TRS in are compressive in the reinforcing phase (SiC) and tensile in the AlSi12 matrix. Measurements from the 10 vol.% SiC in **Fig.5.11 (b)** are not included as a result of the insufficient resolution of the Bragg peaks.

97

TRS [MPa]

250
225
200
175
150
125
100
75
50

0   10   20   30   40
vol. % SiC

(a)

TRS [MPa]

-400
-425
-450
-475
-500
-525
-550
-575

0   10   20   30   40
vol.% SiC

(b)
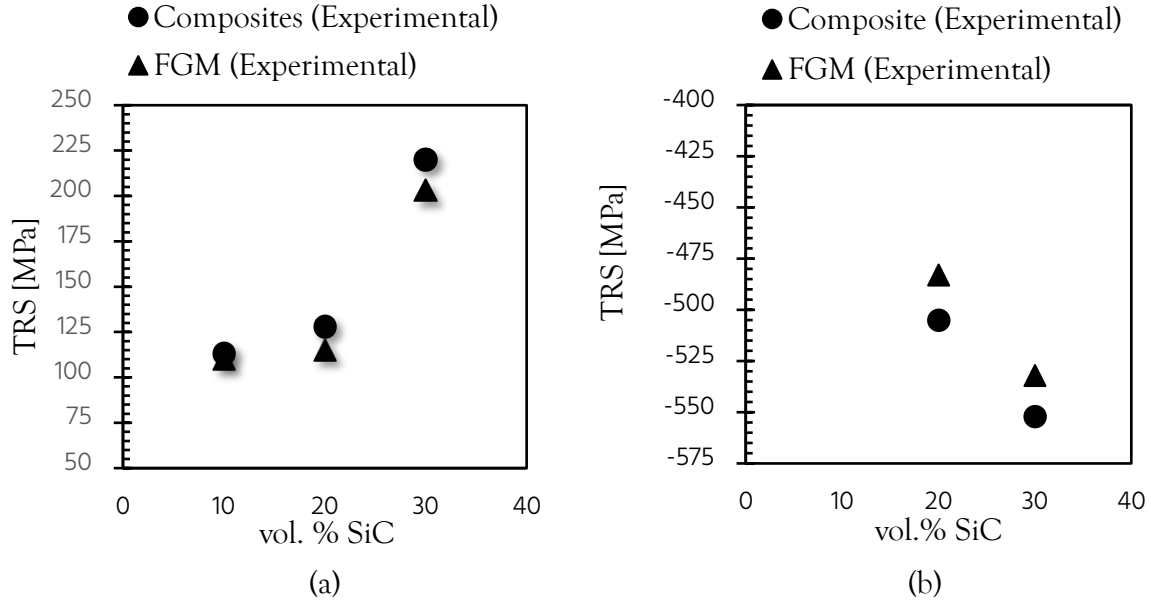
Fig.5.16 The average TRS from the ND measurements for: **(a)** the AlSi12 matrix in the ungraded composites AlSi12+vSiC (v = 10, 20, 30 vol.%) and the three–layer FGM AlSi12+10%SiC/AlSi12+20%SiC/AlSi12+30%SiC; **(b)** the SiC reinforcement in the ungraded AlSi12+vSiC (v = 10, 20, 30 vol.%) composites and the FGM. The data points for the FGM (triangles) represent the average TRS in AlSi12 or SiC in each layer of the FGM.

Three key observations were made from the neutron diffraction measurements of TRS in AlSi12/SiC composites and three–layer FGM:

1. As the volume fraction of the SiC reinforcement increases, the residual stress in the AlSi12 matrix exhibits higher tensile stress, while the ceramic phase SiC experiences higher compressive stress.

2. The average residual stresses in the layers of the FGM are reduced in comparison with the average TRS in the ungraded composite having the same SiC volume fraction. This effect is observed for both the AlSi12 matrix and the SiC reinforcement.

3. The average TRS in the AlSi12 matrix of the AlSi12/SiC ungraded composites increases nonlinearly as the volume fraction of SiC increases (see. **Fig.5.16 (a)**). This is at variance with the AlSi12/Al_2O_3 case, where this relationship was nearly linear (see **Fig.4.19** (a)).

5.4.2   Numerical evaluation of thermal residual stresses

The FE mesh models were prepared from the micro–XCT experiments for all the AlSi12+vSiC (v = 10, 20, 30 vol%) composites as well as the three–layer FGM. Residual stresses in these materials were measured using neutron diffraction (ND). The dimension of the RVE was chosen to be 50 x 50 x 50 elements, which represents to a volume of 50 x 50 x 50 μm^3. The numerical mesh models used for the AlSi12+SiC composites and the three–layer FGM are

shown in **Fig.5.17** and **Fig.5.18**, respectively. To conduct the numerical simulation, the thermal stress within the material was calculated for a temperature range of 500 °C to room temperature (20 °C). The side displacements and other constraints were considered to replicate the conditions during the sintering process using the mold and die, as described in the materials and methods Subection 3.1.2.2. The numerical modeling of the computation of TRS are presented in details in the Section 3.8.4.

| AlSi12+10%SiC | AlSi12+20%SiC | AlSi12+30%SiC |
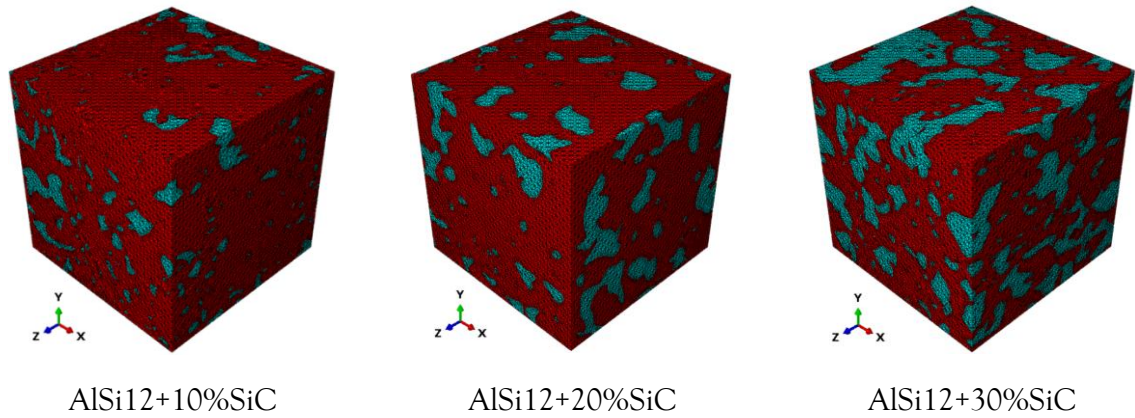
Fig.5.17 The micro–XCT–based FE meshes imported to numerical simulations of TRS in the ungraded composites AlSi12+vSiC (v = 10, 20, 30 vol.%).
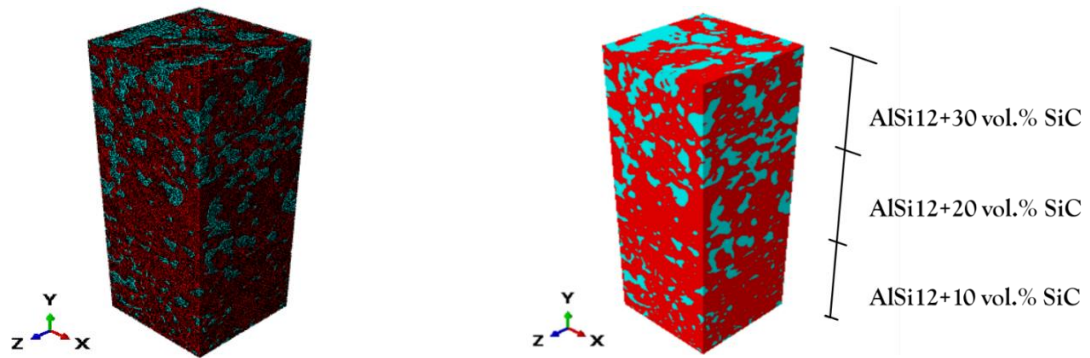
Fig.5.18 The micro–XCT–based FE mesh used in the numerical simulations of TRS in the AlSi12/SiC three–layer FGM.

The micro–XCT–based FEM model was used to simulate thermal residual stress distributions. The ceramic reinforcement was modeled as linear elastic, and the AlSi12 matrix was modeled as elastic–plastic (see Section 3.8.4 for details). Exemplary results of the TRS numerical simulations in the ungraded AlSi12/SiC composites are shown in **Fig.5.19 a–f**.

(a)   TRS distribution in the AlSi12 phase of AlSi12+10% SiC composite

(b)   TRS distribution in SiC phase of AlSi12+10% SiC composite

(c)   TRS distribution in the AlSi12 phase of AlSi12+20% SiC composite

(d)   TRS distribution in the SiC phase of AlSi12+20% SiC composite

(e)   TRS distribution in the AlSi12 phase of AlSi12+30% SiC composite

(f)   TRS distribution in the SiC phase of AlSi12+30% SiC composite

Fig.5.19 Distributions of the thermal residual stress (σ_{xx}) in the AlSi12 matrix (a, c, e), and the SiC reinforcement (b, d, f), obtained from the micro–XCT–based FEM simulations for the AlSi12+vSiC (v= 10, 20, 30 vol.%) ungraded composites.
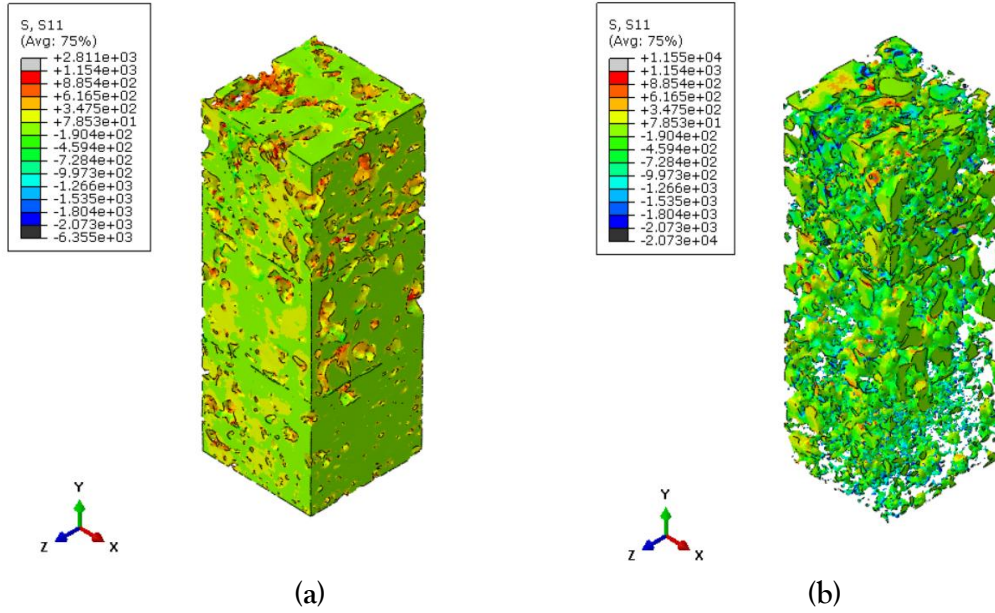
Fig.5.20 Distributions of thermal residual stress (σ_{xx}) in the AlSi12 phase **(a)** and the SiC phase **(b)**, obtained from the numerical simulations for three–layer FGM (AlSi12+10%SiC/AlSi12+20%SiC/AlSi12+30%SiC).

The excellent agreement between the numerical predictions from micro–XCT–based FEM models and the neutron diffraction measurements as shown in **Fig.5.21**. validates the accuracy of the microstructure–based simulation approach. This highlights the central role of the micro–XCT based FE meshes in the numerical models of the TRS behavior in the ungraded AlSi12+vSiC (v= 20, 30 vol.%) composites and the FGM. It is evident that the TRS in the FGM layers are approximately 10% lower than the TRS in the corresponding ungraded composites, considering the neutron diffraction measurement uncertainty error is less than 5% for all materials. Moreover, the micro–XCT–based FEM model successfully captured both the nonlinear behavior of average TRS in the AlSi12 matrix for the ungraded composites with 20 vol.%SiC (as shown in **Fig.5.18a**), and the linear TRS response observed for the 30 vol.%SiC (**Fig.5.18b**), further demonstrating the model's capability to accurately predict TRS in the AlSi12 matrix of ungraded composites across different ceramic contents.
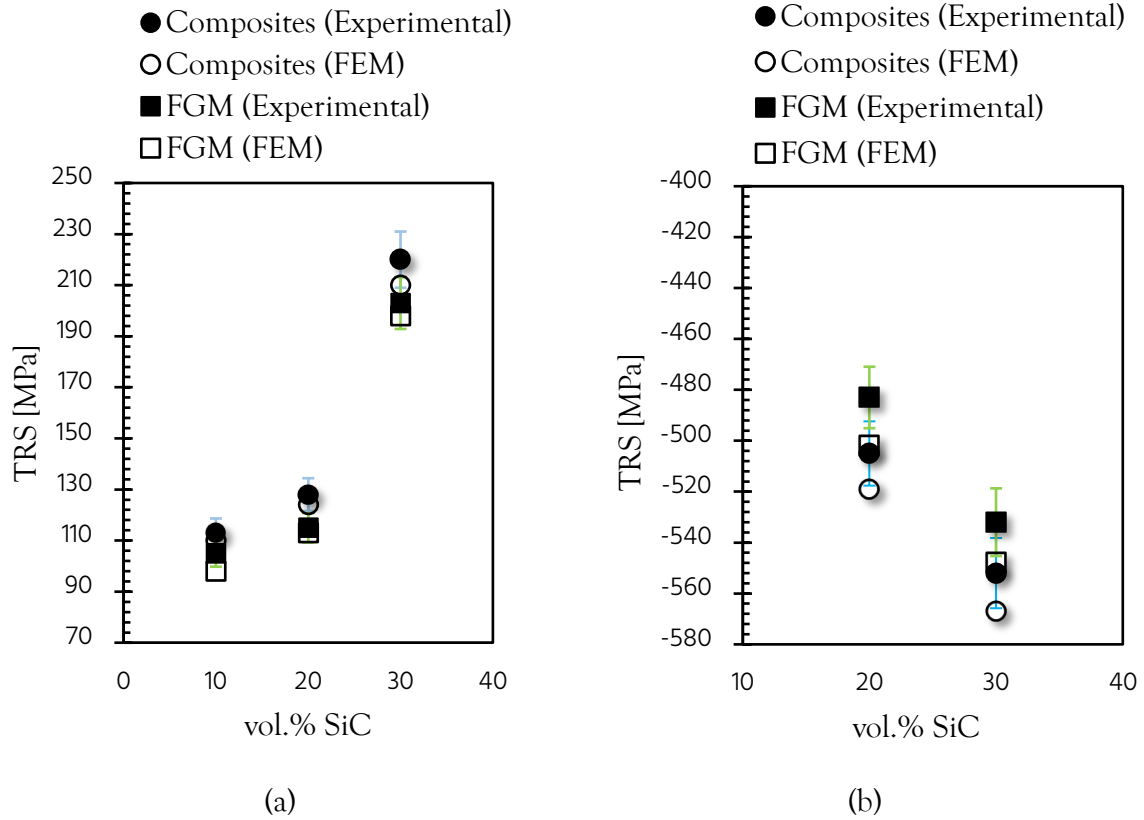
Fig.5.21 Thermal residual stress comparison between experimental data and FEM results for (a) the AlSi12 matrix in ungraded AlSi12+vSiC (v = 10, 20, 30 vol.%) and FGM, and (b) the SiC reinforcement in ungraded AlSi12+vSiC (v = 20, 30 vol.%) composites and FGM.

5.5 Coefficient of thermal expansion of AlSi12/SiC composites and FGMs

As mentioned in Section 3.5 The dilatometric experiments were carried out for three continuous cycles of heating and cooling with an intermediate holding for 30 mins from −60 °C to 500 °C using a thermal–mechanical analysis equipment. For example, a relative change in specimen length and a temperature vs time plot for the hot pressed ungraded AlSi12+20%SiC composite is shown in **Fig.5.22**.
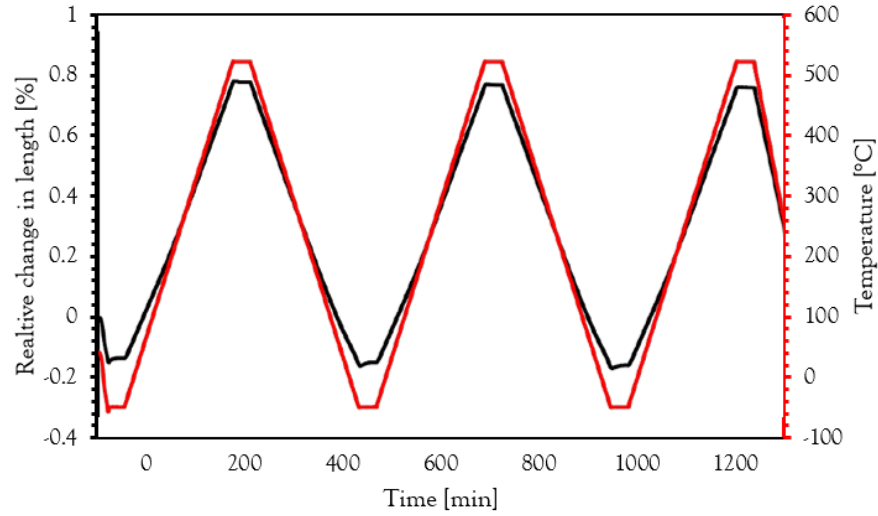
Fig.5.22 Relative change in the length of sample and temperature vs time during the dilatometric experiments of hot–pressed ungraded AlSi12+20%SiC composite.

As already mentioned in Section 3.5, the measurements were performed in the longitudinal and transverse directions on the following samples:

1. Ungraded composites AlSi12+vSiC (v= 10, 20, 30 vol.%)

2. Three-layer FGM (AlSi12+10%SiC/AlSi12+20%SiC/AlSi12+30%SiC) along the longitudinal direction

3. Three-layer FGM (AlSi12+10%SiC/AlSi12+20%SiC/AlSi12+30%SiC) along the transverse direction.

The direction along which pressure is applied during consolidation is called the longitudinal direction, while the direction perpendicular to this pressing axis is termed the transverse direction (see **Fig. 3.14).**

The CoE measurements for the ungraded and graded AlSi12/SiC samples sintered by HP and SPS are shown in **Fig.5.23** and **Fig.5.24**, respectively. They show that the CTE of the ungraded composites decreases as the volume fraction of the metal matrix (AlSi12) gradually decreases due to the increasing ceramic content. The measurements taken in the longitudinal direction in the three-layer FGM closely align with those of the composite reinforced with 20 vol.% SiC. Conversely, in the transverse direction, the CTE of the three-layer FGM slightly exceeds that of the 30 vol.% SiC–reinforced composite beyond 100 °C, for both HP and SPS samples as shown in **Fig.5.23** and **Fig.5.24**, respectively.
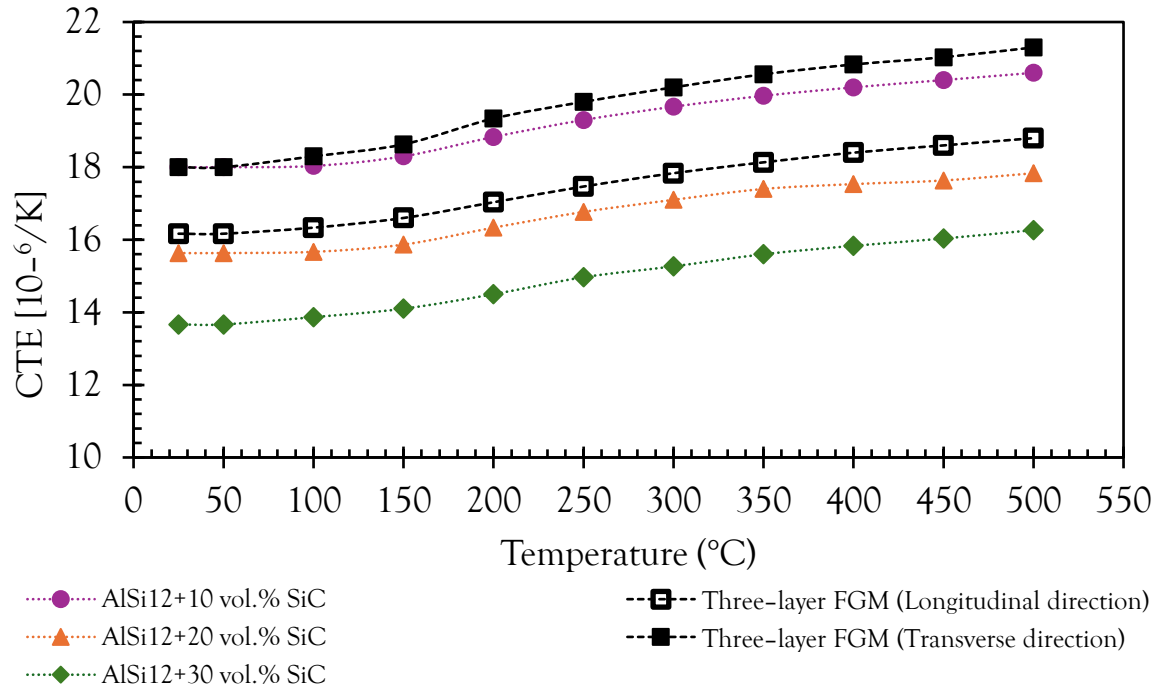
Fig.5.23 Results of CTE measurements of the **HP** ungraded AlSi12+vSiC (v= 10, 20, 30 vol. %) composites in the longitudinal direction and the three–layer FGM in both the longitudinal and transverse directions.
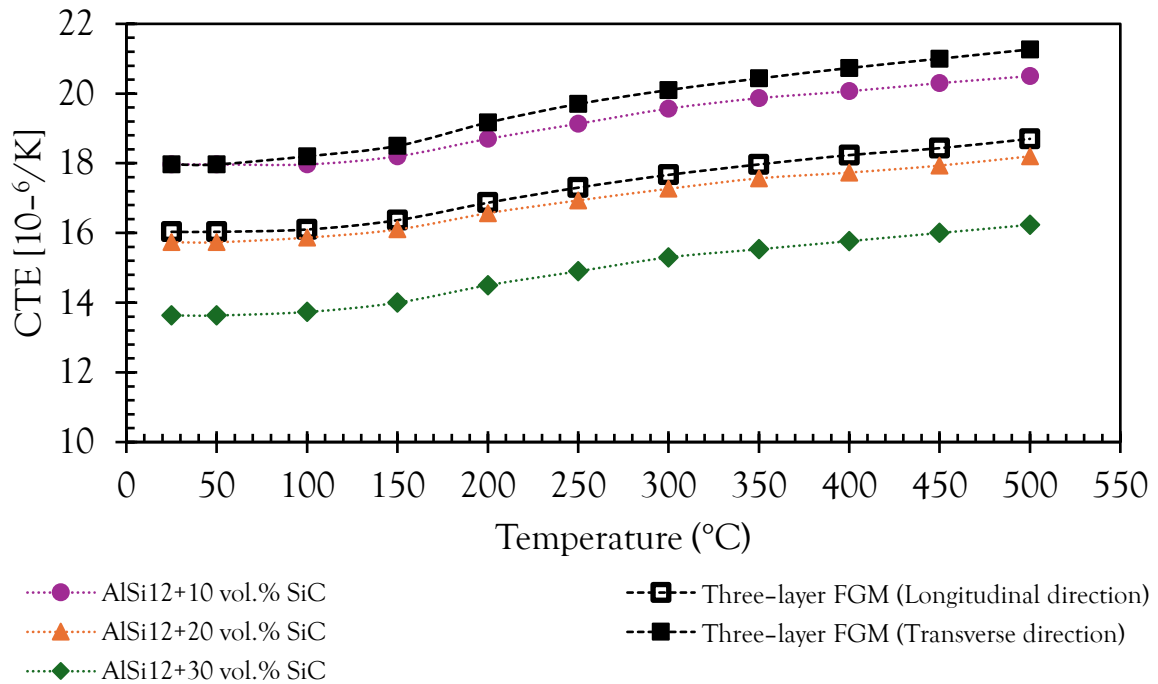
Fig.5.24 Results of the CTE measurements of the **SPS** ungraded AlSi12+vSiC (v= 10, 20, 30 vol. %) composite samples in the longitudinal direction and the three–layer FGM in both transverse direction and longitudinal direction.

WEAR TEST RESULTS

It should be recalled that the wear behavior of the produced composites was not the main focus of this thesis. Nevertheless, for the sake of completeness a preliminary wear study was carried out on representative samples of two ungraded composites, AlSi12+30%Al_2O_3 and AlSi12+30%SiC, produced by hot pressing, by means of a linear abrasion test using the Taber apparatus (see Section 3.7). These two samples were chosen as the ceramic–rich outer layers of the FGM in contact with the brake pads. The measured wear resistance was compared with composites with a higher ceramic content, AlSi12+40%Al_2O_3 and AlSi12+40%SiC, and with the grey cast iron (GCI) from a standard Brembo brake disc used in serial cars.

Earlier investigations [176–178] indicate that AMMCs reinforced with ceramic materials typically demonstrate superior wear resistance compared to their respective unreinforced alloy. However, under specific conditions, the wear performance of AMMCs may be comparable to or even lower than that of pure Al alloys [179,180]. Largely, AMMCs reinforced with hard ceramic into the Al alloy offer good wear resistance, ultimately enhancing the overall wear performance of the tribo–system [181]. However, many investigations suggest, comparing AMMCs with GCI, that the GCI shows better wear resistance. For instance, it was found in [182] that the loss of weight was 0.0116 g in a cast iron brake disc, while AMMC experienced 0.0063 g weight loss which is 46% lower than the cast iron brake disc. However, AMMCs can achieve weight reduction of 30–60% as compared with GCI rotors [183].

Fig.6.1 shows the linear abrasion worn surfaces of samples with AlSi12 + 30%Al_2O_3, AlSi12 + 40%Al_2O_3, AlSi12 + 30%SiC, and AlSi12 + 40%SiC as the outermost layer of FGM samples, along with a GCI sample prepared from a standard Brembo brake disc.

AlSi12+30%Al_2O_3 AlSi12+40%Al_2O_3 AlSi12+30%SiC

AlSi12+40%SiC   GCI (grey cast iron)
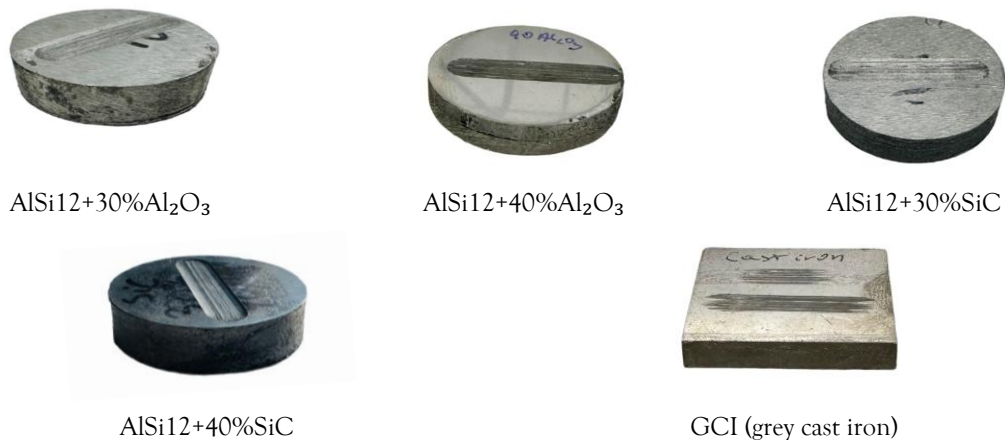
Fig.6.1 The worn surfaces of samples for tribological studies.

To identify the main wear mechanisms, SEM micrographs of the worn surfaces were analyzed **(Fig.6.2)**. The weight percentages of the elements present on the wear track surface and in the wear debris were determined using EDAX analysis. From the SEM analysis the main wear mechanisms in the selected AlSi12/SiC specimens were found to be three–body abrasion and delamination.

(a)   (b)

(c)   (d)
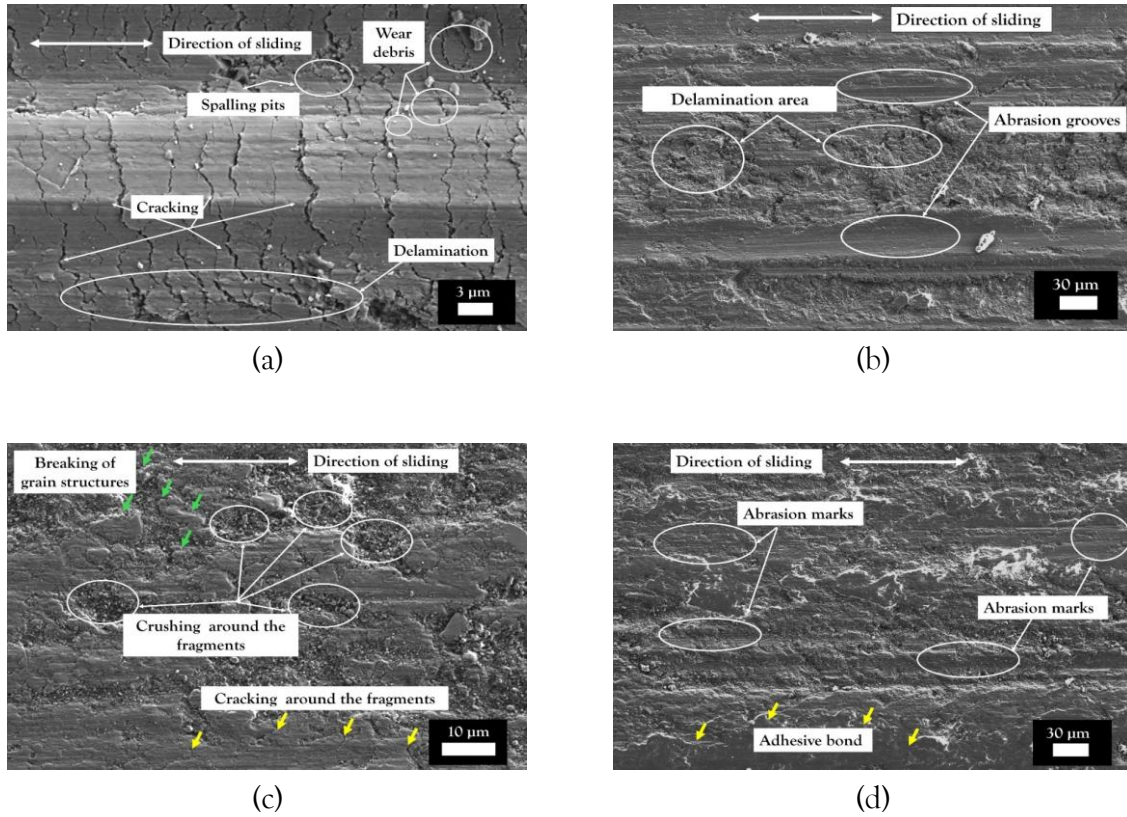
Fig.6.2 SEM micrographs of the composite sample surfaces after the Taber wear test: (a) AlSi12+30%Al_2O_3, (b) AlSi12+40%Al_2O_3, (c) AlSi12+30%SiC, and (d) AlSi12+40%SiC.

Three–body abrasion mechanism

The narrow and wider grooves parallel to the direction of sliding, resulting from abrasive wear can be observed in worn surface of sample **Fig.6.2 (b)** and **Fig.6.2 (d)**. The narrow grooves are likely from the hard ceramic particles within the composite. During the consolidation of AMMCs, hard ceramic particles are embedded in the soft AlSi12 matrix, and these particles are exposed on the surface as the soft Al matrix peels off during the initial rubbing process. In the Taber test, which uses a flat end pin, the surface layer of the Al matrix is first removed, exposing the ceramic particles. As a result, a three–body abrasive wear mechanism occurs in which the AlSi12 matrix undergoes plastic deformation, causing further detachment of ceramic particles. **Fig.6.3 (a)** and **Fig.6.3 (b)** show the exposed ceramic debris and **Fig.6.4 (a)** shows the detached counterpart debris on the wear track. This reinforcing phase released as wear debris acts as a

106

third–body abrasive in the Al matrix [184]. The two factors influencing three–body abrasive mechanism are (i) the weak bond between the metal and the ceramic, which hinders resistance to abrasive wear [163,164,158,159], and (ii) the hardness of the counterpart (abrasive ceramic pin H–10 Calibrade). The inclusion of ceramic reinforcements significantly improves the wear resistance of these composites under two–body abrasive and adhesive wear conditions. However, over time, where hard counterpart material with sharp grains can easily remove the ceramics, the wear resistance of these composites tends to replicate that of the AlSi12 matrix due to the prevalence of three–body abrasive wear mechanisms.

(a)   (b)
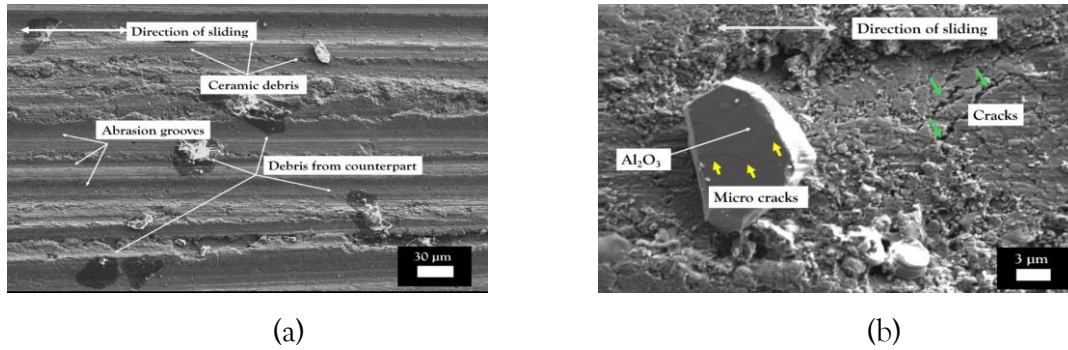
Fig.6.3 SEM micrograph of (a) AlSi12+30 vol.%Al_2O_3 sample (b). AlSi12+40 vol.%Al_2O_3 sample indicating the exposed ceramic debris and debris from counterpart.

Delamination mechanism

Delamination mechanism causes removal of material from the wear surface with initial abrasive wear in terms of micro–ploughing, grooves and cracks transforming into intense adhesive, delamination and plastic deformation at severe conditions [185]. When two surfaces contact, abrasive wear occurs as hard asperities on one surface interact with the softer surface, leading to micro–ploughing, where material is laterally displaced instead of being removed [186]. This repeated interaction creates a smoother surface while generating stress concentrations that can initiate subsurface damage. As the surfaces continue to slide against each other, plastic deformation occurs beneath the surface. This deformation can lead to the nucleation of cracks at the subsurface level [187]. Subsurface cracks and their extension to the surface cause debris to form and peel off from the worn surface (refer to **Fig.6.2 (a)**). The plastic deformation developed by shear stress in subsurface layers of material increases the accumulation of dislocation results in cracks perpendicular to the direction of sliding [188]. Further microcracks can deepen, and spread, leading to fatigue failure. In short, plastic deformation progresses into different stages starting from delamination, breaking of grain structures, cracking around the fragments and then crushing of the fragments as shown in **Fig.6.2 (c)**. Composite sample AlSi12+40% Al_2O_3 under sliding wear conditions undergoes plastic deformation and gradual material transfer to the counterface as shown in **Fig.6.2 (d)**.

107

The wear mechanism of reference material GCI slightly differs from the wear mechanism of composite materials. **Fig.6.4** represents the SEM micrographs of tribosurface of a GCI sample cut from the Brembo brake disc. SEM micrographs reveal minor cracks and voids on the wear tracks. The wear debris held on the wear track mainly of counterspecimen was revealed by the EDS spot (see **Fig.6.4 (c–e)**. When cast iron wears, it undergoes subsurface plastic deformation, which leads to crack formation and ultimately debris generation. This process supports the delamination theory (see **Fig.6.4 (b))**. Few evidence of adhesion was observed **(Fig.6.2. (d))**. When the main wear mechanism is related to delamination and plastic deformation, the material hardness has the dominant influence on abrasive wear [189].
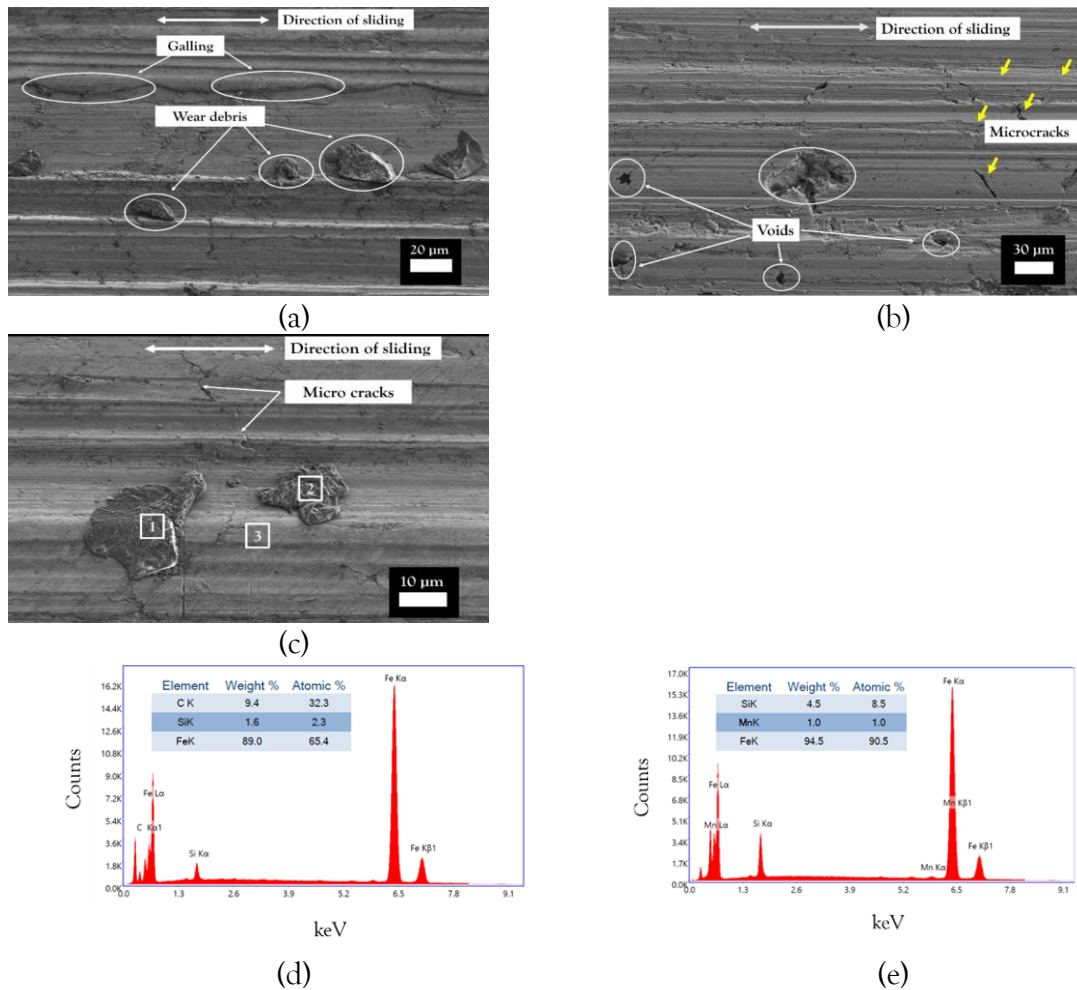
Fig.6.4 (a–c) Scanning electron micrographs of debris, voids and cracks obtained from wear experiments of metallographically polished surfaces of grey cast iron tribosurface. **(d)** SEM–EDS spot analysis of grey cast iron tribosurface for identification of various elements present at point 1 and point 2 in figure (c). **(e)** SEM–EDS analysis of grey cast iron tribosurface for identification of various elements present at point 3 in figure (c).

Mass loss calculations for the material samples after the wear test are listed in **Table 6.1** and depicted graphically in **Fig.6.5**. It can be seen that the AlSi12 alloy reinforced with 30% ceramic (Al_2O_3 or SiC) has a better wear resistance than the alloy reinforced with 40% ceramic, which is a somewhat counter–intuitive result. The relative mass loss for the hot pressed AlSi12+30%Al_2O_3 and AlSi12+30%SiC samples, was 0.209% and 0.129%, respectively. For the AlSi12+40%Al_2O_3 and AlSi12+40%SiC samples the relative mass loss increased to 0.895% and 0.223%, respectively.

Table 6.1 Mass loss calculations for the composite samples after the Taber linear abrasive test.

Material	Initial mass (g)	Mass after test (g)	Mass loss (g)	Relative mass loss (%)
AlSi12+30%Al_2O_3	20.244	20.202	0.043	0.209
AlSi12+40%Al_2O_3	8.7530	8.6750	0.078	0.895
AlSi12+30%SiC	22.442	22.413	0.020	0.129
AlSi12+40%SiC	10.196	10.173	0.023	0.223
Grey cast iron	42.560	42.558	0.001	0.004
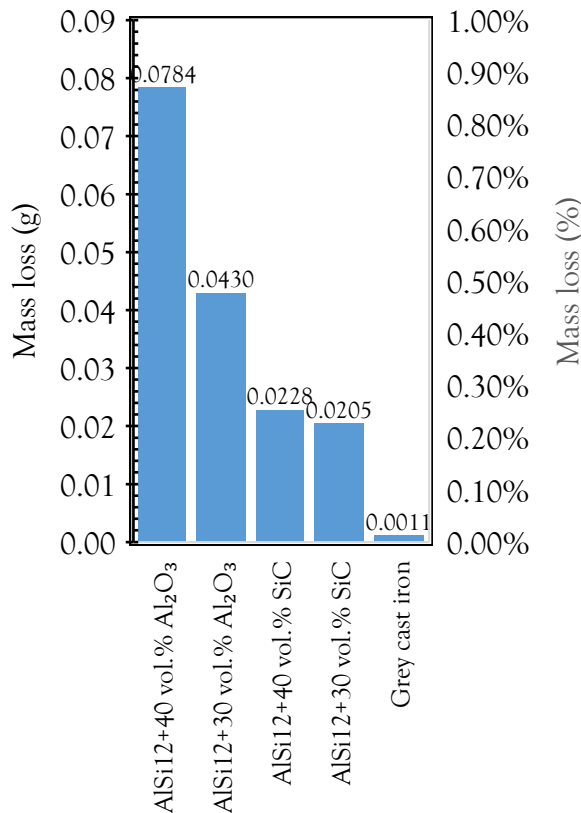
Fig.6.5 Comparison of mass loss of the composite samples and GCI.

This difference in wear performance can be attributed to the distinct wear mechanisms present in composites which are influenced by different levels of surface porosity. Specifically, higher porosity leads to increased surface roughness in the sample. The pore–induced surface roughness of the AlSi12+40%Al_2O_3 and AlSi12+40%SiC samples (i.e. porosity of 7.84% and 4.23%, respectively) results in a lower hardness. The inferior densification of the AlSi12–matrix composites with 40% of the ceramic phase is the effect of the sintering process itself (described in detail in Section 4.1) The ceramic particles are readily exposed to the surface due to densification process making them easily removable. This leads to a material transfer from the worn surface to the counterspecimen surface. The composites with less than 30% ceramic content (i.e. AlSi12+10% ceramic and AlSi12+20% ceramic) were also tested for wear resistance and significant material loss was observed. This is primarily due to the lower content of the ceramic reinforcement, which leads to substantial plastic deformation of the softer AlSi12 matrix. These results are not included here due to their low scientific significance.

It is needed to have more than 20% ceramic particles in AMMCs to achieve better wear resistance and friction properties [183]. From **Fig.6.6**, it is seen that the AlSi12 matrix reinforced with 30 vol.%Al_2O_3 and SiC have the optimum wear resistance. Comparing AlSi12+30%Al_2O_3 with AlSi12+30%SiC, the latter has superior wear resistance. This is primarily due to SiC grains preventing the slipping of large primary silicon particles during wear, thereby imparting wear resistance [190]. There are a number of studies on Al alloys reinforced with Al_2O_3 and SiC using powder metallurgy technique showing that Al alloys reinforced with SiC have better wear resistance than Al alloys reinforced with Al_2O_3 particles [166,167,159,160]. It was also showed in [184] that Al composites reinforced with ceramic particles in the range of 2–30 wt.% show superior wear resistance when SiC is selected rather than Al_2O_3 reinforcement. Compared to all the composites samples under study, GCI has the least relative mass loss i.e. 0.004%. The improvement in the wear resistance of GCI can be related to its microstructural characteristics, including a pearlitic matrix and the distribution of graphite flakes, which contribute to GCI mechanical properties and hardness. Additionally, graphite present in GCI may acts as a solid lubricant for hard grains of the counter sample to remove material at loading conditions [191], [192].
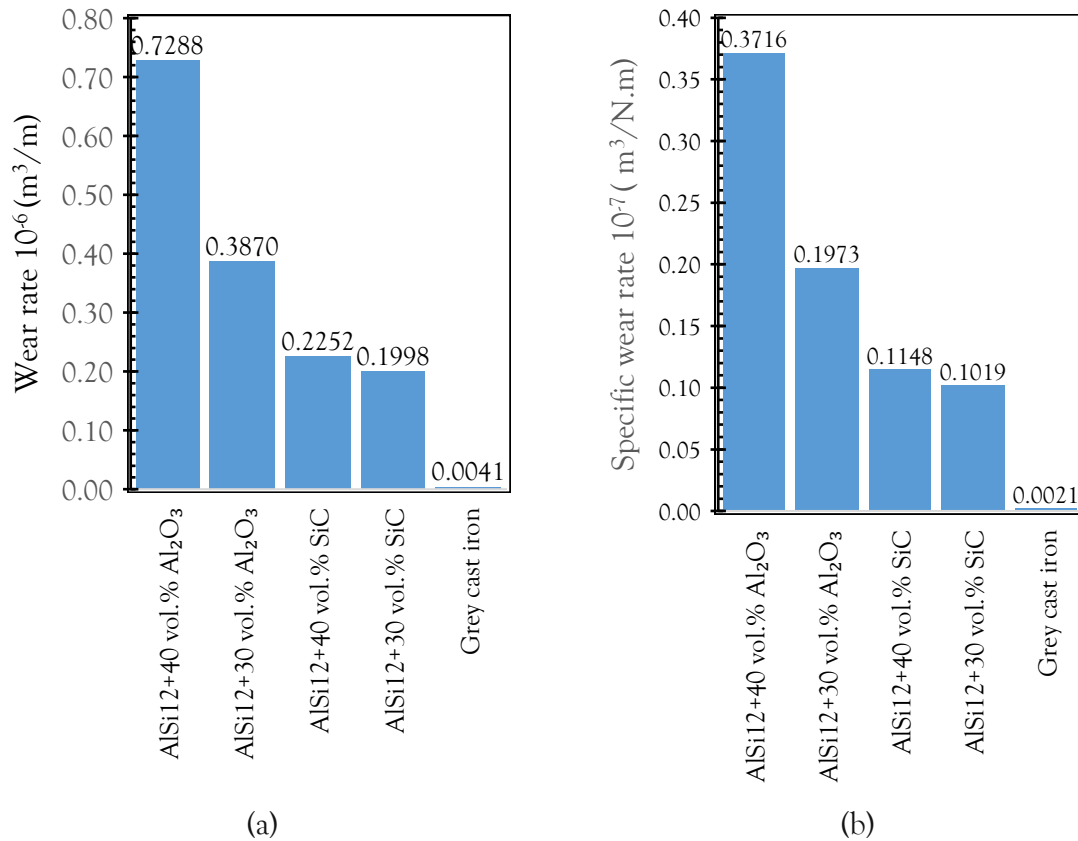
Fig.6.6 (a) Comparison of the wear rate (cm^3/cm) after wear tests for all the samples, **(b)** comparison of the specific wear rate (cm^3/N.cm) for all the samples.

Table 6.2 Wear rate relative to the reference material (GCI).

Material	Specific wear rate ($\times 10^{-7}$ cm^3/N.cm)	Wear rate relative to GCI
AlSi12+30%Al$_2$O$_3$	0.1973	93.705
AlSi12+40%Al$_2$O$_3$	0.1019	176.468
AlSi12+30%SiC	0.3716	48.370
AlSi12+40%SiC	0.1148	54.531
Grey cast iron	0.0021	1.000

Table 6.2 shows the specific wear rates relative to the reference material grey cast iron (GCI). It is evident that the outer layer of the FGMs suffered more abrasive wear than the GCI. The possible reasons are outlined below.

The abrasive ceramic pin (H–10 Calibrade, Taber Industries) is a non–resilient, vitrified pin designed to evaluate steel and ferrous alloys for resistance to abrasion. Examining the brake pads, abrasive ceramic pin are suited for than grey cast iron discs. For the Al brake discs the Non–Asbestos Organic (NAO) brake pad materials are more compatible with due to their low

111

hardness and poor tribological performance [193]. Secondly, the Taber wear test using a flat pin of 6 mm diameter does not completely represent the brake disc–brake pad tribological system due to the smaller contact surface area. It is recommended to utilize a more appropriate counter sample, preferably one prepared from the brake pads specifically designed for composite brake discs. Additionally, employing wear tests that utilize a larger contact surface is essential for accurately representing the brake system, which is crucial for the intended application of the brake disc material.

COMPARISON of AlSi12/Al$_2$O$_3$ and AlSi12/SiC as POTENTIAL BRAKE DISC MATERIALS

This chapter presents a comparison of the thermal conductivity and thermal residual stress between AlSi12/Al$_2$O$_3$ and AlSi12/SiC FGMs. Based on the results, key observations are reported regarding their potential application as brake disc materials in the automotive sector.

Graded aluminum matrix composites, particularly those reinforced with Al$_2$O$_3$ or SiC, are being explored as alternatives to traditional GCI or ceramic matrix composite materials for automotive brake discs. They offer several key advantages over conventional brake disc materials. A notable benefit is their capacity to significantly reduce weight compared to GCI, which contributes to enhanced fuel efficiency. Achieving this weight reduction is essential for improving vehicle performance and reducing energy consumption. A comparative analysis of the relative density of the AlSi12/Al$_2$O$_3$ and AlSi12/SiC composites consolidated by the HP and SPS techniques reveals several salient findings. Firstly, the relative density of AlSi12/Al$_2$O$_3$ samples is higher than that of AlSi12/SiC samples. Secondly, the HP samples demonstrate higher density compared to the SPS samples. These observations are presented in graphical form in **Fig.7.1.**
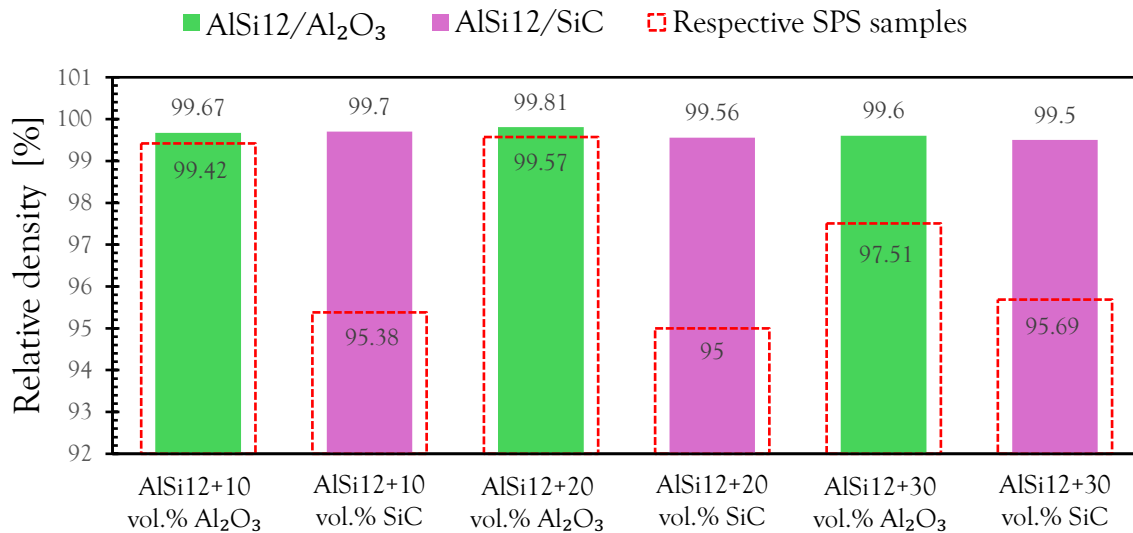
Fig.7.1 Comparison of the relative density of AlSi12/Al$_2$O$_3$ and AlSi12/SiC composites produced by hot pressing (HP) and spark plasma sintering (SPS). The solid columns represent the HP samples, whereas those with the broken line contours represent the SPS samples.

The AlSi12/Al_2O_3 and AlSi12/SiC composite samples fabricated in this study using powder metallurgy techniques (HP and SPS) exhibit a measured density not exceeding 3 g/cm³ (**Fig.7.2**). This is at least two times less than the density of GCI (7 g/cm³) [194], which is commonly used material for serial brake discs.
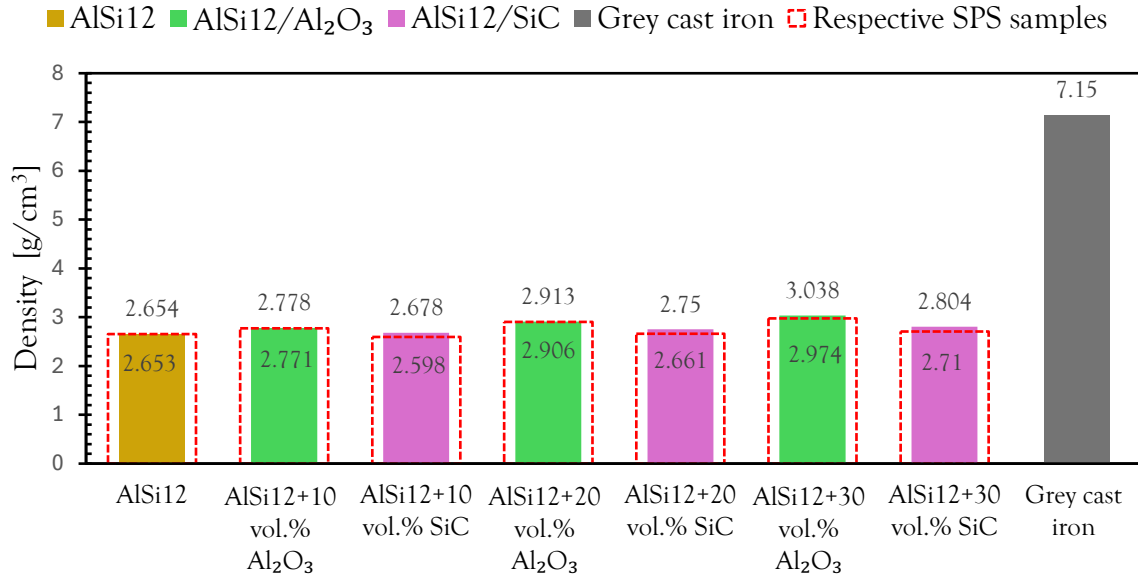
Fig.7.2 Comparison of the density of the AlSi12/Al_2O_3, AlSi12/SiC composites and pure AlSi12 compact measured in–house with the density of GCI [194].

In addition to the thermal properties and processing–induced thermal residual stresses, which are the main focus of this dissertation, the basic mechanical properties of a series of AlSi12/Al_2O_3 and AlSi12/SiC composites with varying volume fractions (10%, 20%, and 30%) were measured to provide a more general characterization of the materials under investigation. **Table 7.1** presents the measured values of fracture toughness, bending strength, and Vickers hardness for the composites produced by HP. The addition of Al_2O_3 and SiC enhanced the bending strength of composites. Between the two, Al_2O_3 provided a greater improvement in strength compared to SiC reinforcement. This is primarily due to several metallurgical and microstructural factors. Firstly, Al_2O_3 forms stronger interfacial bonds with the metal matrix because of its superior chemical compatibility and wetting behavior during sintering [195]. Secondly, Al_2O_3 particles are generally more uniform in size and spherical in shape (see **Fig.3.3**), promoting better dispersion within the matrix and reducing stress concentrations. In addition, Al_2O_3 has a CTE closer to that of AlSi12 (see **Table 3.6**), which reduces thermal mismatch stresses during cooling after sintering (see **Table 7.2**). This helps preserve the interfacial integrity of AlSi12/Al_2O_3 composites and FGMs, minimizing microcracking. The addition of Al_2O_3 and SiC enhances composite bending strength but compromises fracture toughness due to limited plastic deformation, brittle crack propagation along particle interfaces, and defects like particle agglomeration, residual porosity acting as the stress concentration sites, and unreacted silica. It

is evident from **Table 7.1** that the bending strength values of the AlSi12/SiC composites are inferior to those of AlSi12/Al$_2$O$_3$ composites, both produced by HP. This may be attributed to the Hall–Petch relationship, which states that decreasing grain size leads to enhanced strength due to an increase in grain boundaries, which impede dislocation movement. Since both composites share the same metal matrix (AlSi12), the variation in reinforcement particle size, with Al$_2$O$_3$ at 5 µm and SiC at 10 µm, likely results in finer grain structures in the Al$_2$O$_3$–reinforced composites. Furthermore, smaller Al$_2$O$_3$ particles may also restrict grain growth during processing more effectively and thereby improve strength. The Vickers hardness behavior shows a clear trend of increasing hardness with the increasing volume percentage of both Al$_2$O$_3$ and SiC reinforcements in the AlSi12 matrix. It is important to note that the values reported are based on macro Vickers hardness measurements, which cover a substantial portion of the material. This ensures that the readings account for both the matrix and reinforcement phases, providing a reliable representation of the composite's overall hardness behavior.

Table 7.1 Mechanical properties of AlSi12/Al$_2$O$_3$ and AlSi12/SiC composites produced by hot pressing (HP). The bending strength and the fracture toughness (SEVNB probe) were measured in four–point bending. The Vickers hardness was measured under 2 kg force.

Material	Fracture toughness [MPa√m]	Bending strength [MPa]	Vickers hardness [HV2]
AlSi12+10 vol.% Al$_2$O$_3$	12.4 ± 0.81	648.21 ± 19.22	64.90 ± 0.41
AlSi12+20 vol.% Al$_2$O$_3$	9.23 ± 0.82	700.08 ± 7.11	82.73 ± 1.70
AlSi12+30 vol.% Al$_2$O$_3$	8.75 ± 0.54	766.98 ± 8.78	106.3 ± 2.94
AlSi12+10 vol.% SiC	12.9 ± 0.51	625.38 ± 9.19	63.00 ± 1.16
AlSi12+20 vol.% SiC	9.31 ± 0.67	647.69 ± 8.92	78.80 ± 1.16
AlSi12+30 vol.% SiC	8.83 ± 0.4	*)	103.7 ± 2.15

*) The bending strength for AlSi12+30 vol.% SiC is not available due to technical difficulties encountered in this test.

During the braking, kinetic energy is converted into thermal energy through friction, generating significant heat. Efficient heat dissipation is crucial to prevent brake fade and thermal cracking, which can compromise both safety and performance. In this study, the three–layer AlSi12/Al$_2$O$_3$ FGM fabricated by HP exhibits the highest thermal conductivity, followed by AlSi12/SiC FGM produced by HP and SPS, respectively. Their thermal conductivity reaches approximately 140 W/mK for the entire temperature range from 0 to 300 °C as shown in **Fig.7.3**. By selecting two ceramic reinforcements with significantly different thermal conductivities, as described in the Section 3.1.1, the study aimed to investigate the influence of the reinforcement's thermal conductivity on the overall thermal behavior of the graded composites. Interestingly, despite this large difference, the measured thermal conductivities of

the hot–pressed three–layer AlSi12/Al$_2$O$_3$ and AlSi12/SiC FGMs were found to be nearly comparable across the temperature range from room temperature to 300 °C as shown in **Fig.7.3**. This can be explained by the decrease in the ability of AlSi12/SiC FGMs to conduct heat due to the alumina coating forming around the Al and Si grains, as discussed in Subsection 5.3.1. Additionally, both types of FGM demonstrate more than twice the thermal conductivity of grey cast iron, as depicted in **Fig.7.4**. Although grey cast iron is traditionally used for brake discs due to its relatively high thermal conductivity, the superior heat dissipation of AlSi12/Al$_2$O$_3$ and AlSi12/SiC FGMs makes them promising alternatives for automotive brake discs provided that their wear resistance is higher or comparable with that of GCI. However, as demonstrated in Chapter 6, the wear resistance of the AlSi12/Al$_2$O$_3$ and AlSi12/SiC composites, as measured by the Taber abrasive test, was significantly lower than that of GCI. On the other hand, to definitively state that AlSi12/Al$_2$O$_3$ and AlSi12/SiC composites are less resistant to frictional wear than GCI, a properly designed test rig mimicking the real braking system must be used. At this time, the issue remains open and further research is required.
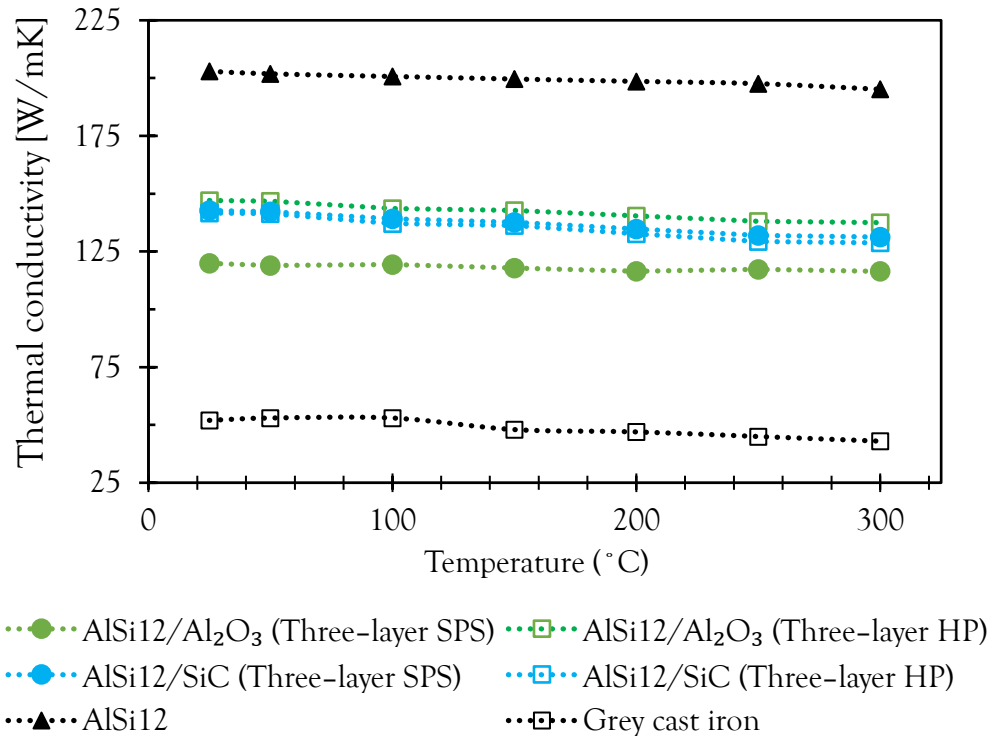
Fig.7.3 Comparison of thermal conductivity of the HP and SPS samples of three–layer AlSi12/Al$_2$O$_3$ and AlSi12/SiC FGMs with the GCI and an unreinforced AlSi12 compact.
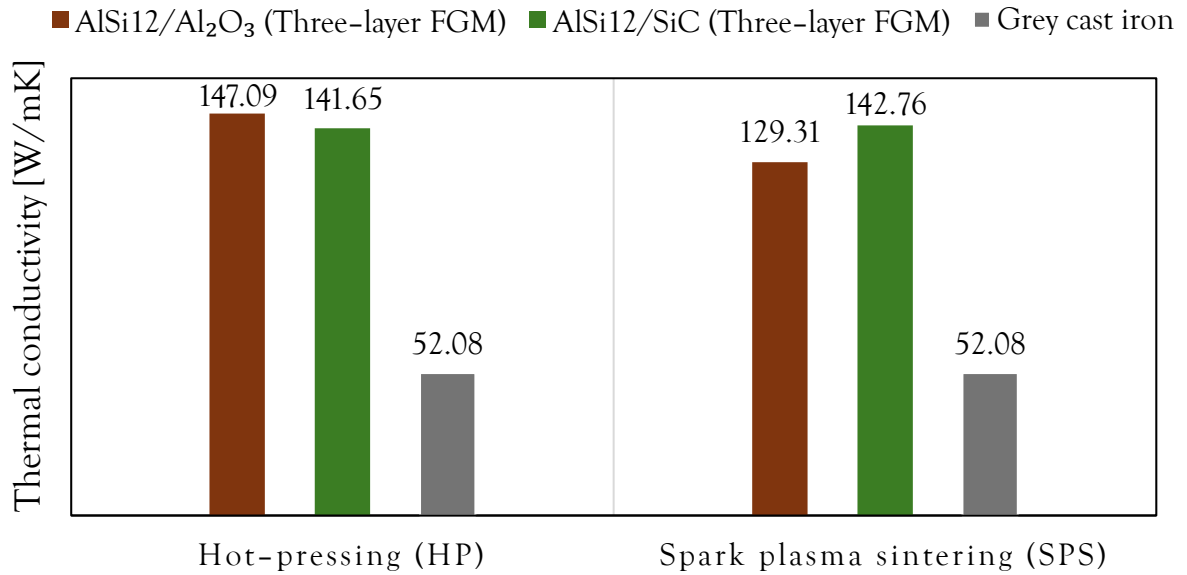
Fig.7.4 Comparison of measured thermal conductivity of three–layer AlSi12/Al$_2$O$_3$ and AlSi12/SiC FGMs with GCI at room temperature (thermal conductivity of GCI taken from [29]).

One key objective of this study was to demonstrate that implementing a graded structure effectively reduces thermal residual stresses in both the metal matrix and ceramic reinforcement of AlSi12/Al$_2$O$_3$and AlSi12/SiC composites. A comparative analysis of residual stress in these materials reveals that the residual stress in the ceramic phase is compressive due to its lower thermal expansion coefficient, which in turn induces tensile stress in the aluminum matrix. This pattern is consistent for both materials (**Fig.7.5**). It is to be noted that the average TRS in the matrix and the reinforcement are practically equal in both AlSi12/Al$_2$O$_3$ and AlSi12/SiC for the ceramic content of 20 vol.%. However, as the reinforcement content (Al$_2$O$_3$ or SiC) increases to 30%, the tensile residual stress in the matrix and compressive stress in the ceramic phase also increase being significantly higher for AlSi12/SiC than AlSi12/Al$_2$O$_3$. It is known that residual stress is influenced by the geometry and size of the reinforcement particles [196,197]. In this regard, AlSi12/SiC exhibits higher stress levels compared to AlSi12/Al$_2$O$_3$, likely due to the distinct shapes of the 40 μm SiC particles as compared to the 10 μm Al$_2$O$_3$ particles.

Neutron diffraction experimental analysis (**Fig.7.5**) further reveals that residual stresses within the FGM layers are approximately 10% lower than those in their ungraded samples. In contrast, grey cast iron casting generates significant and uneven residual stresses within the material [198]. During mechanical machining of components, extrusion and friction are the primary factors contributing to the development of residual compressive stress [161]. The reduction of thermal residual stress in FGMs plays a crucial role in improving key mechanical properties, particularly flexural strength and fracture toughness, which are essential for the

117

durability and performance of these materials. Lower residual stress levels enhance structural integrity, reducing the risk of premature failure due to thermal fatigue or cracking. Given these advantages, the improved thermal stress distribution in FGMs makes them highly suitable for applications such as automotive brake discs, where the mechanical strength and thermal stability are critical for long-term performance.

Considering only the density, thermal conductivity and thermal residual stress levels in the AlSi12/Al$_2$O$_3$ and AlSi12/SiC FGMs, it is difficult to definitely state which material would be a better choice to replace the GCI. A slight advantage is demonstrated by the hot-pressed AlSi12/Al$_2$O$_3$ FGM due to its lower TRS and slightly higher thermal conductivity at a comparable density to AlSi12/SiC.
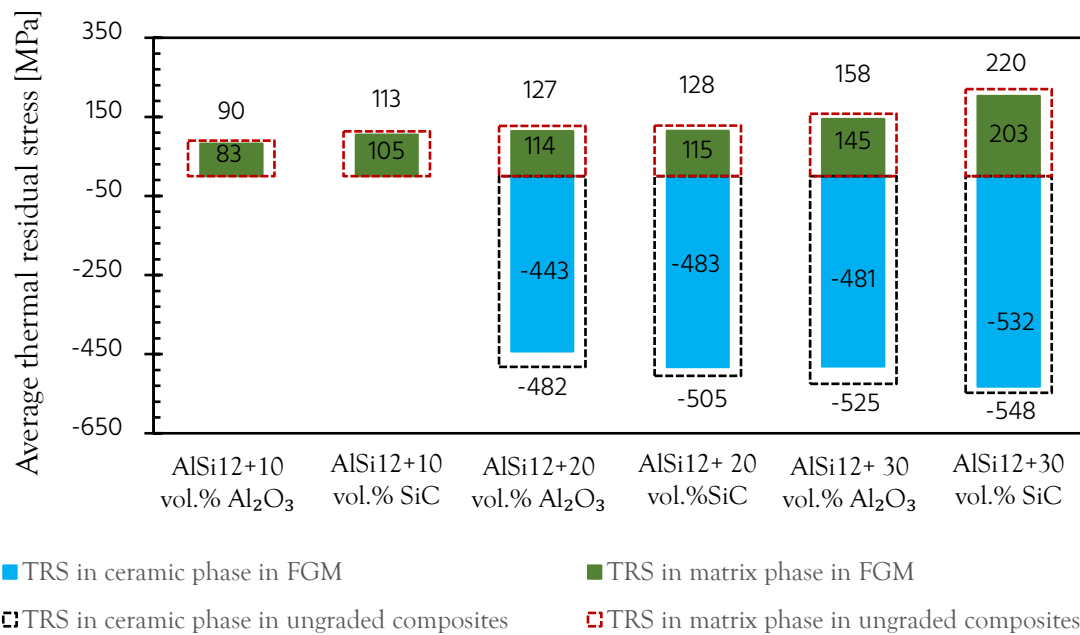
Fig.7.5 Comparison of average thermal residual stress in the hot-pressed ungraded composites and three-layer AlSi12/Al$_2$O$_3$ and AlSi12/SiC FGMs measured by neutron diffraction.

Table 7.2 presents the percetage reduction in average TRS in AlSi12/Al$_2$O$_3$ and AlSi12/SiC, with 10 %, 20% and 30% ceramic content for ungraded and graded composites. The TRS reduction in AlSi12/Al$_2$O$_3$ both graded and ungraded composites becomes more pronounced at 30 vol.% ceramic content. It is approximately 40% lower than AlSi12/SiC for the metal phase and approximately 4-10% lower than in AlSi12/SiC for the ceramic phase. Overall, the AlSi12/Al$_2$O$_3$ both graded and ungraded consistently exhibit reduced TRS in both the metal matrix and the ceramic phase when compared to AlSi12/SiC.

Table 7.2 Reduction in (%) of the average thermal residual stress (TRS) in AlSi12/Al$_2$O$_3$ ungraded composites and FGMs compared to AlSi12/SiC counterparts.

	FGM		Ungraded composite	
Vol.% of ceramic	TRS in AlSi12	TRS in Al$_2$O$_3$	TRS in AlSi12	TRS in Al$_2$O$_3$
10	26.51%	–	25.56%	–
20	0.88%	9.03%	0.79%	4.77%
30	40.00%	10.6%	39.24%	4.38%

SUMMARY, CONCLUSIONS and FUTURE RESEARCH

8.1 Summary

The doctoral thesis successfully achieved its primary objective of investigating the influence of material microstructure on the thermal conductivity and processing–induced thermal residual stresses of two Al–matrix graded composites, AlSi12/Al$_2$O$_3$ and AlSi12/SiC. This was accomplished through a meticulously designed experimental program, supported by microstructure–based numerical modeling.

The manufacturing process, utilizing hot pressing (HP) and spark plasma sintering (SPS) consolidation techniques, was optimized to produce flaw–free, high–quality ungraded composites and FGMs. Experimental optimization focused on design parameters, such as the content of ceramic, number of layers, thickness of each layer, and process parameters for both HP and SPS. The study systematically compared the quality of materials fabricated via hot pressing and spark plasma sintering, evaluating their respective advantages and limitations in terms of their processing conditions. The proposed two–step consolidation technique (cold compaction and hot pressing) of powder blends leading to seamless bonding between layers, enabling a smooth transition of properties in the proposed stepwise graded structure.

Thermal conductivity measurements, conducted using the laser flash method, alongside residual stress assessments via neutron diffraction, provided critical insights into the thermal and mechanical stability of the composites. Furthermore, comprehensive microstructural characterization employing SEM, TEM, XRD, and EDX enabled a deeper understanding of the relationship between microstructure and its impact on thermal conductivity and processing–induced residual stresses in these materials. A numerical model for computing thermal conductivity and thermal residual stresses was developed directly from the material's real microstructure, enabled by the high quality of the micro–XCT scans and the better selection of finite element shapes and smoothing methods. A comparison of the numerical results with experimental data revealed the capability of these modeling techniques to predict thermal conductivity and TRS in the Al–matrix FGMs. In addition, the coefficient of thermal expansion and tribological behavior of these composites were analyzed to assess their suitability for potential applications in automobile brake discs.

8.2 Conclusions and Future Research

The following are the key conclusions drawn from the dissertation:

The quality and structural integrity of the ungraded composites and three-layer graded composites $AlSi12/Al_2O_3$ and $AlSi12/SiC$ were successfully achieved through optimized processing conditions. SEM analysis confirmed a uniform distribution of ceramic particles, indicating strong bonding quality. The aluminum alloy formed a continuous matrix across the layers, ensuring a smooth transition that facilitated the formation of a strong metallurgical bond. Notably, no macro-pores or cracks were detected, further validating the reliability of the composite structure. Additionally, the choice of consolidation technique played a crucial role in determining the final density of the composites. The lower and well-controlled heating rate of hot (HP) compared to spark plasma sintering (SPS) resulted in the HP samples exhibiting slightly higher density, with a maximum percentage difference of 3.58%. Furthermore, when comparing $AlSi12/Al_2O_3$ and $AlSi12/SiC$ composites, the Al_2O_3-reinforced composites exhibited higher density than the SiC-reinforced composites. Specifically, for HP processing: The relative density of $AlSi12/SiC$ was 98% and the relative density of $AlSi12/Al_2O_3$ was 99%. For SPS processing: The relative density of $AlSi12/SiC$ was 95% and the relative density of $AlSi12/Al_2O_3$ was 98%. These results highlight the influence of both material reinforcement and consolidation technique on the final density of the composites.

The thermal conductivity in $AlSi12/Al_2O_3$ and $AlSi12/SiC$ composites and three-layer FGMs is strongly influenced by the processing method and ceramic content. Despite using the same starting powders and achieving similar densities, the HP samples exhibit higher thermal conductivity than SPS samples. This difference is related to the processing techniques leading to differences in the densification and grain growth in the final sinters. Since the grain size and grain boundaries significantly impact the heat transfer, the HP samples exhibit a superior thermal performance. This observation confirms **Hypothesis 2**, which stated that grain size of the metal matrix can affect the thermal conductivity of these composites and FGMs.

Additionally, a linear decline in thermal conductivity is observed with increasing ceramic content in $AlSi12/Al_2O_3$ and $AlSi12/SiC$ composites. Particularly in $AlSi12/SiC$ composites, although SiC reinforcement is generally expected to enhance thermal conductivity, the results exhibit an unexpected negative trend. This is attributed to the presence of Al_2O_3 coatings formed during the sintering using hot pressing and spark plasma sintering at the metal-ceramic interface, which hinders the heat transfer. This phenomenon is further confirmed by XRD and TEM analysis, validating the impact of interfacial reactions on thermal performance. This supports **Hypothesis 3**, which proposed that the formation of new phases during sintering affects the thermal conductivity of $AlSi12/SiC$ composites and FGMs.

The experimentally determined thermal conductivity and micro–XCT–based FEM results show a relative error of within 4% for ungraded composites and 8% for FGMs, validating the proposed numerical model for predicting thermal conductivity. Finally, when comparing both material thermal conductivity measurements of three–layer FGMs with those of grey cast iron and unreinforced AlSi12 alloy, the HP-fabricated Al_2O_3–reinforced FGM exhibited the highest thermal conductivity, followed by SiC–reinforced FGMs produced via HP and SPS. Notably, the thermal conductivity of both FGM types was at least twice as high as that of grey cast iron, the conventional material used for automotive brake discs.

Thermal residual stress measurements were conducted using the neutron diffraction (ND) technique and compared with micro–XCT–based FEM modeling. The measured and computed residual stresses in both the ceramic and metal phases of the ungraded and graded composites remain well below their respective ultimate compressive and tensile strengths. On average, the residual stresses within the FGM layers decreased by approximately 10% compared to the ungraded composite, demonstrating that the selected design parameters effectively minimize the average residual stresses. This outcome directly confirms **Hypothesis 1**, which stated that average TRS in FGMs would be lower than in ungraded composites.

Thermal residual stress is primarily influenced by the shapes and sizes of the ceramic particles used in the composites. In the present study, the AlSi12/SiC composites and FGM exhibit higher stress levels. Finally, the experimentally measured TRS and micro–XCT–based FEM results show a relative error of within 4%, validating the proposed numerical model for predicting TRS in graded Al–matrix composites. This confirms **Hypothesis 4**, which asserted that micro–XCT–based finite element models, when properly configured, can accurately predict thermal conductivity and TRS in these composites and FGMs.

These findings highlight the critical role of processing techniques and the impact of graded microstructure minimizing thermal residual stresses during production. This demonstrates the potential of graded structures for high–performance applications, such as automotive brake discs, where strength and durability are essential.

The measurements showed that the coefficients of thermal expansion (CTE) of the AlSi12/SiC composites are by approximately 32% lower than that of the unreinforced aluminum alloy (AlSi12) matrix. The thermal expansion of the AlSi12/SiC composites is influenced by the ceramic content, and the behavior of the graded AlSi12/SiC composites closely follows the rule of mixtures. A similar trend in thermal expansion is anticipated for graded AlSi12/Al_2O_3 as well.

Tribological studies have shown that Al alloys reinforced with ceramic particles provide optimal wear resistance at a certain ceramic content. Wear tests conducted on samples with 10%, 20%, 30%, and 40% Al_2O_3 and SiC showed that the samples with 30% ceramic content had the best wear resistance. Furthermore, when comparing AlSi12+30%Al_2O_3 with AlSi12+30%SiC composites, the Al alloy reinforced with 30% SiC exhibited superior wear

resistance. However, the ceramic–rich layer of the graded sample experienced more abrasive wear in the linear pin–on–flat test than the reference material, grey cast iron, due to the testing conditions and the use of an unsuitable counterpart material.

Overall, the outcome of this dissertation will enable a better understanding of the design and thermal behavior of the $AlSi12/Al_2O_3$ and $AlSi12/SiC$ graded composites with reduced thermal residual stresses (TRS), making them less prone to uncontrolled fracture under service conditions. And its findings could influence industries seeking lightweight structural materials with high thermal conductivity, minimal thermal expansion, high wear resistant and high specific strength.

The following outcomes can be considered as highlights of this dissertation:

- A complete chain of interrelated research blocks of "fabrication, characterization, and modeling" was employed. Having all individual elements of this research chain under control made it possible to ascertain the key impacts of the graded composite structure on the thermal properties and thermal residual stress under investigation..

- The proposed numerical modeling tool, using actual material microstructure images obtained through micro–computed tomography (micro–XCT), offers predictive capability for residual stresses which cannot be achieved by the micromechanical models based on the Eshelby's solution [199]. In particular, the micro–XCT FEM model properly captured the nonlinear behavior of tensile residual stresses in the AlS12 matrix of ungraded AlSi12/SiC composites and FGMs. Moreover, this modeling approach can support expensive and time-consuming measurement techniques such as neutron diffraction and synchrotron diffraction, by utilizing the results from micro–XCT–based finite element (FE) modeling.

- Across the varying material compositions and processing methods, the micro–XCT–based finite element (FE) models consistently achieved high predictive accuracy with errors below 10%, demonstrating remarkable robustness and versatility.

Future research on the topics considered in this thesis should be focused on addressing specific issues such as accurate assessment of the thermal behavior at the interface. This could be approached by comparing the experimental results with a numerical model in which interfacial thermal conductance is incorporated, using interfacial thermal conductance values estimated experimentally through methods such as Time–Domain Thermoreflectance (TDTR), Frequency–Domain Thermoreflectance (FDTR), and others.

In the process of sintering of Al/SiC composites and FGMs, an increase in the SiC content results in a decrease in thermal conductivity due to interfacial reactions that occur at elevated temperatures. Increasing the size of the SiC particles and adding silicon to the aluminum matrix can help mitigate these effects, though trade–offs remain. Future research

should focus on advanced processing methods, alloying strategies and optimized graded structures to improve the performance of aluminum matrix composites (AMMCs) in high-performance applications.

References

[1]   Kota, N., Charan, M. S., Laha, T., and Roy, S., "Review on Development of Metal/Ceramic Interpenetrating Phase Composites and Critical Analysis of Their Properties," *Ceram. Int.*, Vol. 48, No. 2, 2022, pp. 1451–1483.

[2]   Ibrahim, I. A., Mohamed, F. A., and Lavernia, E. J., "Particulate Reinforced Metal Matrix Composites–a Review," *J. Mater. Sci.*, Vol. 26, 1991, pp. 1137–1156.

[3]   Kumar, S. N. N., Devarajaiah, R. M., and Ram Prabhu, T., "Review on Aluminium Based Functionally Graded Composites," *Mater. Today Proc.*, Vol. 39, 2021, pp. 1743–1749.

[4]   Miranda, R. M., Santos, T. G., Gandra, J., Lopes, N., and Silva, R. J. C., "Reinforcement Strategies for Producing Functionally Graded Materials by Friction Stir Processing in Aluminium Alloys," *J. Mater. Process. Technol.*, Vol. 213, No. 9, 2013, pp. 1609–1615.

[5]   Sheraf, J., and Darius Gnanaraj, S., "Synthesis of Functionally Graded Aluminium Metal Matrix Composites – a Mini Review," *Mater. Today Proc.*, 2023.

[6]   Chen, M., Bai, Y., Zhang, Z., and Zhao, H., "The Preparation of High-Volume Fraction SiC/Al Composites with High Thermal Conductivity by Vacuum Pressure Infiltration," *Crystals*, Vol. 11, No. 5, 2021.

[7]   Hassanzadeh-Aghdam, M. K., and Ansari, R., "A Micromechanics-Based Hierarchical Analysis of Thermal Conductivity of Metallic Nanocomposites with Agglomerated Ceramic Nanoparticles," *Arab. J. Sci. Eng.*, Vol. 46, No. 8, 2021, pp. 7143–7151.

[8]   Xu, Y., Tanaka, Y., Goto, M., Zhou, Y., and Yagi, K., "Thermal Conductivity of SiC Fine Particles Reinforced Al Alloy Matrix Composite with Dispersed Particle Size," *J. Appl. Phys.*, Vol. 95, No. 2, 2004, pp. 722–726.

[9]   Lindroos, V. K., and Talvitie, M. J., "Recent Advances in Metal Matrix Composites," *J. Mater. Process. Technol.*, Vol. 53, 1995, pp. 273–284.

[10]   Ribes, H., Suéry, M., L'espérance, G., and Legoux, J. G., "Microscopic Examination of the Interface Region in 6061-Al/SiC Composites Reinforced with as-Received and Oxidized SiC Particles," *Metall. Trans. A*, Vol. 21, No. 9, 1990, pp. 2489–2496.

[11]   Ramnath, B. V., Elanchezhian, C., Annamalai, R. M., Aravind, S., Sri, T., Atreya, A., Vignesh, V., and Subramanian, C., "Aluminium Metal Matrix Composites–A Review," *Rev. Adv. Mater. Sci.*, Vol. 38, 2014, pp. 55–60.

[12]   Narayana Murty, S. V. S., Nageswara Rao, B., and Kashyap, B. P., "On the Hot Working Characteristics of 6061Al–SiC and 6061–Al_2O_3 Particulate Reinforced Metal Matrix Composites," *Compos. Sci. Technol.*, Vol. 63, No. 1, 2003, pp. 119–135.

[13]   Qu, X. H., Zhang, L., Wu, M., and Ren, S. Bin, "Review of Metal Matrix Composites with High Thermal Conductivity for Thermal Management Applications," *Prog. Nat. Sci.: Mater. Int.*, Vol. 21, No. 3, 2011, pp. 189–197.

[14]   Sharma, S., Dhanasekaran, S., and Sreenivasan, V. S., "Microstructure and Mechanical Behavior of SiC Reinforced Aluminum Metal Matrix Composites for Automobile Applications," Vol. 4, 2014.

[15]   Purohit, R., Qureshi, M. M. U., and Jain, A., "Forming Behaviour of Aluminium Matrix Nano Al_2O_3 Composites for Automotive Applications," *Adv. Mater. Process. Technol.*, Vol. 6, No. 2, 2020, pp. 324–335.

[16]   Abbas, M. R., B., U. M., Noor, A. M., Ahmad, N., and Rajoo, S., "Microstructural Evaluation of a Slurry Based Ni/YSZ Thermal Barrier Coating for Automotive Turbocharger Turbine Application," *Mater. Des.*, Vol. 109, 2016, pp. 47–56.

[17]   Drake, J. T., Williamson, R. L., and Rabin, B. H., "Finite Element Analysis of Thermal Residual Stresses at Graded Ceramic-metal Interfaces. Part II. Interface Optimization for Residual Stress Reduction," *J. Appl. Phys.*, Vol. 74, No. 2, 1993, pp. 1321–1326.

[18]   Lee, Y. D., and Erdogan, F., "Residual/Thermal Stresses in FGM and Laminated Thermal Barrier Coatings," *Int. J. Fract.*, Vol. 69, No. 2, 1994, pp. 145–165.

[19]   Jin, Z. H., and Paulino, G. H., "Transient Thermal Stress Analysis of an Edge Crack in a Functionally Graded Material," *Int. J. Fract.*, Vol. 107, No. 1, 2001, pp. 73–98.

[20]   Erdogan, F., and Wu, B. H., "Crack Problems in FGM Layers under Thermal Stresses," *J. Therm. Stress.*, Vol. 19, No. 3, 1996, pp. 237–265.

[21]   Tan Engin and Kaplan, Y. and A. H. and A. S., "Production of the AA2196–TiB2 MMCs via PM Technology," 2019.

[22]   Orrù, R., Licheri, R., Locci, A. M., Cincotti, A., and Cao, G., "Consolidation/Synthesis of Materials by Electric Current Activated/Assisted Sintering," *Mater. Sci. Eng., R*, Vol. 63, Nos. 4-6, 2009, pp. 127–287.

[23]   Rahimian, M., Ehsani, N., Parvin, N., and Baharvandi, H. R., "The Effect of Sintering Temperature and the Amount of Reinforcement on the Properties of $Al–Al_2O_3$ Composite," *Mater. Des.*, Vol. 30, No. 8, 2009, pp. 3333–3337.

[24]   Kimoto, Y., Nagaoka, T., Mizuuchi, K., Fukusumi, M., Morisada, Y., and Fujii, H., "Thermal Conductivity of Al/SiC Particulate Composites Produced by Friction Powder Sintering," *J. Jpn. Soc. Powder Powder Metall.*, Vol. 63, No. 7, 2016, pp. 563–567.

[25]   Neubrand, A., Chung, T.–J., Rödel, J., Steffler, E. D., and Fett, T., "Residual Stresses in Functionally Graded Plates," *J. Mater. Res.*, Vol. 17, No. 11, 2002, pp. 2912–2920.

[26]   Fitzpatrick, M. E., Hutchings, M. T., and Withers, P. J., "Separation of Macroscopic, Elastic Mismatch and Thermal Expansion Misfit Stresses in Metal Matrix Composite Quenched Plates from Neutron Diffraction Measurements," *Acta Materialia*, Vol. 45, No. 12, 1997, pp. 4867–4876.

[27]   Leszczyńska–Madej, B., Garbiec, D., and Madej, M., "Effect of Sintering Temperature on Microstructure and Selected Properties of Spark Plasma Sintered Al-SiC Composites," *Vacuum*, Vol. 164, 2019, pp. 250–255.

[28]   Balokhonov, R., Romanova, V., Zinovieva, O., and Zemlianov, A., "Microstructure–Based Analysis of Residual Stress Concentration and Plastic Strain Localization Followed by Fracture in Metal–Matrix Composites," *Eng. Fract. Mech.*, Vol. 259, 2022, p. 108138.

[29]   Maj, J., Basista, M., Węglewski, W., Bochenek, K., Strojny-Nędza, A., Naplocha, K., Panzner, T., Tatarková, M., and Fiori, F., "Effect of Microstructure on Mechanical Properties and Residual Stresses in Interpenetrating Aluminum–Alumina Composites Fabricated by Squeeze Casting," *Mater. Sci. Eng. A*, Vol. 715, 2018, pp. 154–162.

[30]   Guo, J., Fu, H., Pan, B., and Kang, R., "Recent Progress of Residual Stress Measurement Methods: A Review," *Chin. J. Aeronaut.*, Vol. 34, No. 2, 2021, pp. 54–78.

[31]   F. A. Kandil, J. D. Lord, A. T. Fry, and P. V. Grant, "A Review of Residual Stress Measurement Methods– A Guide to Technique Selection," Teddington, Middlesex, UK, 2002.

[32]   Eshelby, J. D., "The Determination of the Elastic Field of an Ellipsoidal Inclusion, and Related Problems," 1957.

[33]   Bouafia, F., Serier, B., and Bouiadjra, B. A. B., "Finite Element Analysis of the Thermal Residual Stresses of SiC Particle Reinforced Aluminum Composite," *Comput. Mater. Sci.*, Vol. 54, No. 1, 2012, pp. 195–203.

[34]   Guzmán, R. E., and Hernández Arroyo, E., "Influence of Thermal Residual Stress on Behaviour of Metal Matrix Composites Reinforced with Particles," Vol. 687, 2016.

[35]   Zhang, X. X., Xiao, B. L., Andrä, H., and Ma, Z. Y., "Multiscale Modeling of Macroscopic and Microscopic Residual Stresses in Metal Matrix Composites Using 3D Realistic Digital Microstructure Models," *Compos. Struct.*, Vol. 137, 2016, pp. 18–32.

[36]   Kamaruzaman, F. F., Nuruzzaman, D. M., Ismail, N. M., Hamedon, Z., Iqbal, A. K. M. A., and Azhari, A., "Microstructure and Properties of Aluminium–Aluminium Oxide Graded Composite Materials," *IOP Conf. Ser.: Mater. Sci. Eng.*, Vol. 319, No. 1, 2018.

[37]   Gudlur, P., Forness, A., Lentz, J., Radovic, M., and Muliana, A., "Thermal and Mechanical Properties of Al/Al$_2$O$_3$ Composites at Elevated Temperatures," *Mater. Sci. Eng. A*, Vol. 531, 2012, pp. 18–27.

[38]   Tatar, C., "Investigation of Thermal Conductivity and Microstructure of the A–Al$_2$O$_3$ Particulate Reinforced Aluminum Composites (Al/Al$_2$O$_3$ –MMC) by Powder Metallurgy Method," *Phys. B: Condens. Matter*, Vol. 405, 2010, pp. 896–899.

[39]   Rahimian, M., Parvin, N., and Ehsani, N., "The Effect of Production Parameters on Microstructure and Wear Resistance of Powder Metallurgy Al–Al$_2$O$_3$ Composite," *Mater. Des.*, Vol. 32, No. 2, 2011, pp. 1031–1038.

[40]   Sujan, D., Oo, Z., Rahman, M. E., Maleque, M. A., and Tan, C. K., "Physio–Mechanical Properties of Aluminium Metal Matrix Composites Reinforced with Al$_2$O$_3$ and SiC," *Int. J. Eng. Appl. Sci.*, Vol. 6, 2012, pp. 288–291.

[41]   Maj, J., Węglewski, W., Bochenek, K., Rogal, Ł., Woźniacka, S., and Basista, M., "A Comparative Study of Mechanical Properties, Thermal Conductivity, Residual Stresses, and Wear Resistance of Aluminum–

Alumina Composites Obtained by Squeeze Casting and Powder Metallurgy," *Metall. Mater. Trans. A*, Vol. 52, 2021, pp. 4727–4736.

[42] Leszczyńska-Madej, B., Madej, M., Wąsik, A., and Garbiec, D., "Spark Plasma Sintering of Al–SiC Composites with High SiC Content: Study of Microstructure and Tribological Properties," *Arch. Civ. Mech. Eng.*, Vol. 23, No. 4, 2023, p. 229.

[43] Carotenuto, G., Gallo, A., and Nicolais, L., "Degradation of SiC Particles in Aluminium–Based Composites," *J Mater Sci*, Vol. 29, 1994, pp. 4967–4974.

[44] Lee Jae-Chul, Byun', J.-Y., Oh', C.-S., Seok, H.-K., and Lee', H.-I., "Effect of Various Processing Methods on the Interfacial Reactions in SiC/2024 Al Composites," Acta Metallurgica Inc, 1997.

[45] Sritharan, T., Chan, L. S., Tan, L. K., and Hung, N. P., "A Feature of the Reaction between Al and SiC Particles in an MMC," *Mater. Charact.*, Vol. 47, No. 1, 2001, pp. 75–77.

[46] Aydin, M., "An Experimental Study of The Effects of Ceramic Composition on The Electrical and Thermal Properties of Al/SiC Composites," *Eur. J. Sci. Technol.*, 2021.

[47] Hasselman, D. P. H., Donaldson, K. Y., and Geiger, A. L., "Effect of Reinforcement Particle Size on the Thermal Conductivity of a Particulate–Silicon Carbide–Reinforced Aluminum Matrix Composite," *J. Am. Ceram. Soc.*, Vol. 75, No. 11, 1992, pp. 3137–3140.

[48] Chen, Z., Tan, Z., Ji, G., Fan, G., Schryvers, D., Ouyang, Q., and Li, Z., "Effect of Interface Evolution on Thermal Conductivity of Vacuum Hot Pressed SiC/Al Composites," *Adv. Eng. Mater.*, Vol. 17, No. 7, 2015, pp. 1076–1084.

[49] Kawai, C., "Effect of Interfacial Reaction on the Thermal Conductivity of Al–SiC Composites with SiC Dispersions," *J. Am. Ceram. Soc.*, Vol. 84, No. 4, 2001, pp. 896–898.

[50] Mizuuchi, K., Inoue, K., Agari, Y., Nagaoka, T., Sugioka, M., Tanaka, M., Takeuchi, T., Tani, J. I., Kawahara, M., Makino, Y., and Ito, M., "Processing of Al/SiC Composites in Continuous Solid–Liquid Co–Existent State by SPS and Their Thermal Properties," *Compos. B Eng.*, Vol. 43, No. 4, 2012, pp. 2012–2019.

[51] Hekner, B., Myalski, J., Pawlik, T., and Sopicka-Lizer, M., "Effect of Carbon in Fabrication Al–SiC Nanocomposites for Tribological Application," *Materials*, Vol. 10, No. 6, 2017.

[52] Gui, M., Kang, S. B., and Euh, K., "Thermal Conductivity of Al–SiC$_p$ Composites by Plasma Spraying," *Scr. Mater.*, Vol. 52, No. 1, 2005, pp. 51–56.

[53] Ghasemi, H. M., Emamy, M., Eskandari, H., Hokamoto, K., Nishida, M., and Matsuda, M., "Interfacial Characterisation in Al–20 Vol.–%SiC$_p$ Explosively Compacted Composite," *Mater. Sci. Technol.*, Vol. 25, No. 1, 2009, pp. 108–110.

[54] Koç, M., and Zeybek, M. S., "Investigation of the Effect of High–Frequency Induction Sintering on Phase Structure and Microstructure of SiC Reinforced Aluminum Matrix Composites," *Sakarya Univ. J. Sci.*, Vol. 28, No. 3, 2024, pp. 550–557.

[55] Zhang, Z. H., Wang, F. C., Luo, J., Lee, S. K., and Wang, L., "Microstructures and Mechanical Properties of Spark Plasma Sintered Al–SiC Composites Containing High Volume Fraction of SiC," *Mater. Sci. Eng., A*, Vol. 527, Nos. 27–28, 2010, pp. 7235–7240.

[56] Lin, X., Xu, Q., Deng, T., Yang, B., and Chen, L., "Improving Thermal Conductivity of Al/SiC Composites by Post-Oxidization of Reaction-Bonded Silicon Carbide Preforms," *Sci. Rep.*, Vol. 14, No. 1, 2024.

[57] Kawai, C., "Fabrication of Al–SiC Composites Using a Hot-Forging Technique and Their Thermal Conductivity," *J. Ceram. Soc. Jpn.*, Vol. 110, 2002, pp. 1016–1020.

[58] Zhang, Q., Wu, G., Sun, D., Chen, G., Jiang, L., Mg, S. C., Ni, F., and Al, Z., "Microstructure and Thermal Conduction Properties of an Al–12Si Matrix Composite Reinforced with Dual Sized SiC Particles," *J. Mater. Sci.*, Vol. 39, 2004, pp. 303–305.

[59] Teng, F., Yu, K., Luo, J., Fang, H. jie, Shi, C. li, Dai, Y. long, and Xiong, H. qing, "Microstructures and Properties of Al–50%SiC Composites for Electronic Packaging Applications," *Trans. Nonferrous Met. Soc. China*, Vol. 26, No. 10, 2016, pp. 2647–2652.

[60] Arpón, R., Molina, J. M., Saravanan, R. A., García–Cordovilla, C., Louis, E., and Narciso, J., "Thermal Expansion Behaviour of Aluminium/SiC Composites with Bimodal Particle Distributions," *Acta Materialia*, Vol. 51, No. 11, 2003, pp. 3145–3156.

[61] Sugio, K., Choi, Y. B., and Sasaki, G., "Effect of the Interfacial Thermal Resistance on the Effective Thermal Conductivity of Aluminum Matrix Composites," *Mater. Trans.*, Vol. 57, No. 5, 2016, pp. 582–589.

[62] Liu, Q., Wang, F., Shen, W., Qiu, X., He, Z., Zhang, Q., and Xie, Z., "Influence of Interface Thermal Resistance on Thermal Conductivity of SiC/Al Composites," *Ceram. Int.*, Vol. 45, No. 17, 2019, pp. 23815–23819.

[63] Chen, M., Bai, Y., Zhang, Z., and Zhao, H., "The Preparation of High–Volume Fraction SiC/Al Composites with High Thermal Conductivity by Vacuum Pressure Infiltration," *Crystals*, Vol. 11, No. 5, 2021.

[64] Molina, J. M., Prieto, R., Narciso, J., and Louis, E., "The Effect of Porosity on the Thermal Conductivity of Al–12 Wt.% Si/SiC Composites," *Scripta Materialia*, Vol. 60, No. 7, 2009, pp. 582–585.

[65] Erdemir, F., Canakci, A., Varol, T., and Ozkaya, S., "Corrosion and Wear Behavior of Functionally Graded Al2024/SiC Composites Produced by Hot Pressing and Consolidation," *J. Alloys Compd.*, Vol. 644, 2015, pp. 589–596.

[66] Natarajan, N., Vijayarangan, S., and Rajendran, I., "Wear Behaviour of A356/25SiCp Aluminium Matrix Composites Sliding against Automobile Friction Material," *Wear*, Vol. 261, Nos. 7–8, 2006, pp. 812–822.

[67] Surya, M. S., and Nilesh, T. V., "Synthesis and Mechanical Behaviour of (Al/SiC) Functionally Graded Material Using Powder Metallurgy Technique," *Mater. Today Proc.*, Vol. 18, 2019, pp. 3501–3506.

[68] Surya, M. S., and Prasanthi, G., "Tribological Behaviour of Aluminum Silicon Carbide Functionally Graded Material," *Tribol. Ind.*, Vol. 40, No. 2, 2018, p. 247.

[69]   Erdemir, F., Canakci, A., and Varol, T., "Microstructural Characterization and Mechanical Properties of Functionally Graded Al2024/SiC Composites Prepared by Powder Metallurgy Techniques," *Trans. Nonferrous Met. Soc. China (English Edition)*, Vol. 25, No. 11, 2015, pp. 3569–3577.

[70]   Vijaya Kumar, P., Jebakani, & D., Velmurugan, & C., and Senthilkumar, & V, "Effect of SiC on Mechanical and Microstructural Characteristics of Al Based Functionally Graded Material," *Silicon*, Vol. 14, 2022, pp. 1247–1252.

[71]   Surya, M. S., and Prasanthi, G., "Effect of Silicon Carbide Weight Percentage and Number of Layers on Microstructural and Mechanical Properties of Al7075/SiC Functionally Graded Material," *Silicon*, Vol. 14, No. 4, 2022, pp. 1339–1348.

[72]   Bhattacharyya, M., Kumar, A. N., and Kapuria, S., "Synthesis and Characterization of Al/SiC and Ni/Al_2O_3 Functionally Graded Materials," *Mater. Sci. Eng., A*, Vol. 487, Nos. 1–2, 2008, pp. 524–535.

[73]   Siva Surya, M., "Effect of SiC Weight Percentage and Sintering Duration on Microstructural and Mechanical Behaviour of Al6061/SiC Composites Produced by Powder Metallurgy Technique," *Silicon*, Vol. 14, 2022, pp. 273–2739.

[74]   Surya, M. S., "Fabrication, Interlayer Bonding and Mechanical Characterization of Four Layered AA7075/SiC Functionally Graded Material," *Silicon*, Vol. 15, No. 10, 2023, pp. 4521–4528.

[75]   Übeyli, M., Balci, E., Sarikan, B., Öztaş, M. K., Camuşcu, N., Yildirim, R. O., and Keleş, Ö., "The Ballistic Performance of SiC–AA7075 Functionally Graded Composite Produced by Powder Metallurgy," *Mater. Des.*, Vol. 56, 2014, pp. 31–36.

[76]   Lin, C.-Y., Bathias, C., McShane, H. B., and Rawlings, R. D., "Production of Silicon Carbide Al 2124 Alloy Functionally Graded Materials by Mechanical Powder Metallurgy Technique," *Powder Metall.*, Vol. 42, No. 1, 1999, pp. 29–33.

[77]   Aydın, M., Toker, G. P., Acar, E., and Karaca, H. E., "Processing and Compressive Response of Al/SiC Functionally Graded Composites," *Eur. Phys. J. Plus*, Vol. 135, No. 6, 2020, p. 486.

[78]   Acar, E., and Aydın, M., "Damping Behavior of Al/SiC Functionally Graded and Metal Matrix Composites," *J. Asian Ceram. Soc.*, Vol. 9, No. 2, 2021, pp. 578–585.

[79]   Alizadeh, A., Ebrahimi, F., Zahmatkesh, M. R., and Hajizamani, M., "Effect of Solution Heat Treatment on Microstructure, Matrix/Reinforcement Interface, and Mechanical Properties of Functionally Graded Al–SiC Composite Synthesized by Hot Pressing," *Trans. Indian Inst. Met.*, Vol. 76, No. 8, 2023, pp. 2285–2293.

[80]   Manohar, G., Maity, S. R., and Pandey, K. M., "Microstructural and Mechanical Properties of Microwave Sintered AA7075/Graphite/SiC Hybrid Composite Fabricated by Powder Metallurgy Techniques," *Silicon*, Vol. 14, 2022, pp. 5179–5189.

[81]   Srinivas, P. N. S., Babu P, R., and Balakrishna, B., "Microstructural, Mechanical and Tribological Characterization on the Al Based Functionally Graded Material Fabricated Powder Metallurgy," *Mater. Res. Express*, Vol. 7, No. 2, 2020.

[82]   Karacif, K., "Hardness and Corrosion Properties of Functionally Graded AA5083/Al_2O_3 Composites Produced by Powder Metallurgy Method," *Int. J. Mater. Res.*, Vol. 111, No. 9, 2020, pp. 719–725.

[83] Kamaruzaman, F. F., Nuruzzaman, D. M., Chowdhury, M. A., Jamaludin, S. N. S., Basri, S., and Ismail, N. M., "Characterisation of Four-Layered Al–Al$_2$O$_3$ Functionally Graded Material Prepared through Powder Metallurgy and Pressureless Sintering," *Int. J. Mater. Prod. Technol.*, Vol. 59, No. 1, 2019, pp. 48–62.

[84] Farahmand, S., Monazzah, A. H., and Soorgee, M. H., "The Fabrication of Al$_2$O$_3$ –Al FGM by SPS under Different Sintering Temperatures: Microstructural Evaluation and Bending Behavior," *Ceram. Int.*, Vol. 45, Nos. 17, Part B, 2019, pp. 22775–22782.

[85] J. C. Maxwell, "A Treatise on Electricity and Magnetism," Oxford at the Clarendon, Dove, NY, 1873.

[86] Ordonez Miranda, J., Yang, R., and Alvarado Gil, J. J., "A Model for the Effective Thermal Conductivity of Metal–Nonmetal Particulate Composites," *J. Appl. Phys.*, Vol. 111, No. 4, 2012, p. 044319.

[87] Every, A. G., Tzou, Y., Hasselman, D. P. H., and Raj, R., "The Effect of Particle Size on the Thermal Conductivity of ZnS/Diamond Composites," *Acta Metall. Mater.*, Vol. 40, No. 1, 1992, pp. 123–129.

[88] Lewis, T. B., and Nielsen, L. E., "Dynamic Mechanical Properties of Particulate-filled Composites," *J. Appl. Polym. Sci.*, Vol. 14, No. 6, 1970, pp. 1449–1471.

[89] Hale, D. K., "The Physical Properties of Composite Materials," *J. Mater. Sci.*, Vol. 11, No. 11, 1976, pp. 2105–2141.

[90] Thiele, A. M., Kumar, A., Sant, G., and Pilon, L., "Effective Thermal Conductivity of Three-Component Composites Containing Spherical Capsules," *Int. J. Heat Mass Transf.*, Vol. 73, 2014, pp. 177–185.

[91] Marcos-Gómez, D., Ching-Lloyd, J., Elizalde, M. R., Clegg, W. J., and Molina-Aldareguia, J. M., "Predicting the Thermal Conductivity of Composite Materials with Imperfect Interfaces," *Compos. Sci. Technol.*, Vol. 70, No. 16, 2010, pp. 2276–2283.

[92] Madan, R., and Bhowmick, S., "Modeling of Functionally Graded Materials to Estimate Effective Thermo-Mechanical Properties," *World J. Eng.*, Vol. 19, No. 3, 2021.

[93] Schapery, R. A., "Thermal Expansion Coefficients of Composite Materials Based on Energy Principles," *J. Compos. Mater.*, Vol. 2, No. 3, 1968, pp. 380–404.

[94] Kerner, E. H., "The Elastic and Thermo-Elastic Properties of Composite Media," *Proc. Phys. Soc. Sect. B.*, Vol. 69, No. 8, 1956, pp. 808–813.

[95] Turner, P. S., "The Problem of Thermal-Expansion Stresses in Reinforced Plastics," *J. Res. Natl. Bur. Stand.*, Vol. 37, 1946, pp. 239–250.

[96] Gudlur, P., Muliana, A., and Radovic, M., "Effective Thermo-Mechanical Properties of Aluminum–Alumina Composites Using Numerical Approach," *Compos. B Eng.*, Vol. 58, 2014, pp. 534–543.

[97] Sharma, N. K., Misra, R. K., and Sharma, S., "Modeling of Thermal Expansion Behavior of Densely Packed Al/SiC Composites," *Int. J. Solids Struct.*, Vols. 102–103, 2016, pp. 77–88.

[98] Voigt, W., "Ueber Die Beziehung Zwischen Den Beiden Elasticitätsconstanten Isotroper Körper," *Annalen der Physik*, Vol. 274, No. 12, 1889, pp. 573–587.

[99] Reuss, A., "Berechnung Der Fließgrenze von Mischkristallen Auf Grund Der Plastizitätsbedingung Für Einkristalle," *J. Appl. Math. Mech.*, Vol. 9, No. 1, 1929, pp. 49–58.

[100] Shen, H.-S., "Functionally Graded Materials," CRC Press, 2016.

[101] Reddy, J. N., and Chin, C. D., "Thermomechanical Analysis of Functionally Graded Cylinders and Plates," *J. Therm. Stress.*, Vol. 21, No. 6, 1998, pp. 593–626.

[102] Swaminathan, K., and Sangeetha, D. M., "Thermal Analysis of FGM Plates – A Critical Review of Various Modeling Techniques and Solution Methods," *Compos. Struct.* Volume 160, 43–60.

[103] Apalak, M. K., and Gunes, R., "Thermal Residual Stress Analysis of Ni–Al$_2$O$_3$, Ni–TiO2, and Ti–SiC Functionally Graded Composite Plates Subjected to Various Thermal Fields," *J. Thermoplast. Compos. Mater.*, Vol. 18, No. 2, 2005, pp. 119–152.

[104] Noda, N., "Thermal Stresses in Functionally Graded Materials," *J. Therm. Stress.*, Vol. 22, Nos. 4–5, 1999, pp. 477–512.

[105] Praveen, G. N., and Reddy, J. N., "Nonlinear Transient Thermoelastic Analysis of Functionally Graded Ceramic–Metal Plates," *Int. J. Solids Struct.*, Vol. 35, No. 33, 1998, pp. 4457–4476.

[106] Yin, H. M., Paulino, G. H., Buttlar, W. G., and Sun, L. Z., "Effective Thermal Conductivity of Two–Phase Functionally Graded Particulate Composites," *J. Appl. Phys.*, Vol. 98, No. 6, 2005.

[107] Yin, H. M., Paulino, G. H., Buttlar, W. G., and Sun, L. Z., "Effective Thermal Conductivity of Functionally Graded Particulate Nanocomposites With Interfacial Thermal Resistance," *J. Appl. Mech.*, Vol. 75, No. 5, 2008.

[108] Shabana, Y. M., and Noda, N., "Numerical Evaluation of the Thermomechanical Effective Properties of a Functionally Graded Material Using the Homogenization Method," *Int. J. Solids Struct.*, Vol. 45, Nos. 11–12, 2008, pp. 3494–3506.

[109] Pélegris, C., Ferguen, N., Leclerc, W., Lorgouilloux, Y., Hocquet, S., Rigo, O., Guessasma, M., Bellenger, E., Courtois, C., Lardot, V., and Leriche, A., "Thermal Conductivity Modelling of Alumina/Al Functionally Graded Composites," *Can. J. Chem. Eng.*, Vol. 93, No. 2, 2015, pp. 192–200.

[110] Muliana, A. H., "A Micromechanical Model for Predicting Thermal Properties and Thermo–Viscoelastic Responses of Functionally Graded Materials," *Int. J. Solids Struct.*, Vol. 46, No. 9, 2009, pp. 1911–1924.

[111] Araki, N., Makino, A., Ishiguro, T., and Mihara, J., "An Analytical Solution of Temperature Response in Multilayered Materials for Transient Methods," *Int. J. Thermophys.*, Vol. 13, No. 3, 1992, pp. 515–538.

[112] Ishiguro, T., Makino, A., Araki, N., and Noda, N., "Transient Temperature Response in Functionally Gradient Materials," *Int. J. Thermophys.*, Vol. 14, No. 1, 1993, pp. 101–121.

[113] Tanigawa, Y., "Theoretical Approach of Optimum Design for a Plate of Functionally Gradient Materials under Thermal Loading," *Thermal Shock and Thermal Fatigue Behavior of Advanced Ceramics*, Vol. 241, Springer Netherlands, Dordrecht, 1993, pp. 171–180.

[114] Ravichandran, K. S., "Thermal Residual Stresses in a Functionally Graded Material System," *Mater. Sci. Eng., A.*, Vol. 201, Nos. 1–2, 1995, pp. 269–276.

[115] Tanaka, K., Tanaka, Y., Enomoto, K., Poterasu, V. F., and Sugano, Y., "Design of Thermoelastic Materials Using Direct Sensitivity and Optimization Methods. Reduction of Thermal Stresses in Functionally Gradient Materials," *Comput. Methods Appl. Mech. Eng.*, Vol. 106, Nos. 1–2, 1993, pp. 271–284.

[116] Tanaka, K., Tanaka, Y., Watanabe, H., Poterasu, V. F., and Sugano, Y., "An Improved Solution to Thermoelastic Material Design in Functionally Gradient Materials: Scheme to Reduce Thermal Stresses," *Comput. Methods Appl. Mech. Eng.*, Vol. 109, Nos. 3–4, 1993, pp. 377–389.

[117] Burlayenko, V. N., Altenbach, H., Sadowski, T., Dimitrova, S. D., and Bhaskar, A., "Modelling Functionally Graded Materials in Heat Transfer and Thermal Stress Analysis by Means of Graded Finite Elements," *Appl. Math. Model.*, Vol. 45, 2017, pp. 422–438.

[118] Basista, M., Węglewski, W., Bochenek, K., Poniżnik, Z., and Nowak, Z., "Micro-CT Finite Element Analysis of Thermal Residual Stresses and Fracture in Metal–Ceramic Composites," *Adv. Eng. Mater.*, Vol. 19, No. 8, 2017, p. 1600725.

[119] De Giovanni, M., Warnett, J. M., Williams, M. A., Haribabu, N., and Srirangam, P., "X-Ray Tomography Investigation of Intensive Sheared Al–SiC Metal Matrix Composites," *Mater. Charact.*, Vol. 110, 2015, pp. 258–263.

[120] Węglewski, W., Bochenek, K., Basista, M., Schubert, Th., Jehring, U., Litniewski, J., and Mackiewicz, S., "Comparative Assessment of Young's Modulus Measurements of Metal–Ceramic Composites Using Mechanical and Non–Destructive Tests and Micro-CT Based Computational Modeling," *Comput. Mater. Sci.*, Vol. 77, 2013, pp. 19–30.

[121] Mackin, T. J., Noe, S. C., Ball, K. J., Bedell, B. C., Bim–Merle, D. P., Bingaman, M. C., Bomleny, D. M., Chemlir, G. J., Clayton, D. B., Evans, H. A., Gau, R., Hart, J. L., Karney, J. S., Kiple, B. P., Kaluga, R. C., Kung, P., Law, A. K., Lim, D., Merema, R. C., Miller, B. M., Miller, T. R., Nielson, T. J., O'Shea, T. M., Olson, M. T., Padilla, H. A., Penner, B. W., Penny, C., Peterson, R. P., Polidoro, V. C., Raghu, A., Resor, B. R., Robinson, B. J., Schambach, D., Snyder, B. D., Tom, E., Tschantz, R. R., Walker, B. M., Wasielewski, K. E., Webb, T. R., Wise, S. A., Yang, R. S., and Zimmerman, R. S., "Thermal Cracking in Disc Brakes," *Eng. Fail. Anal.*, Vol. 9, No. 1, 2002, pp. 63–76.

[122] Gao, M., Yang, B., Huang, Y., and Wang, G., "Effects of General Imperfect Interface/Interphase on the in–Plane Conductivity of Thermal Composites," *Int. J. Heat Mass Transf.*, Vol. 172, 2021, p. 121213.

[123] Deuis, R. L., Subramanian, C., and Yellupb, J. M., "Dry Sliding Wear of Aluminium Composites–A Review," *Compos. Sci. Technol.*, Vol. 57, 1997, pp. 415–435.

[124] Qi Hai bo, Ding Zhan lai, Fan Yun chang, and Jiang Zhi qing, "Research on Automotive Brake Discs of SiC_p/Al Composite," *Acta Mater. Compos. Sin.*, Vol. 18, No. 1, 2001, pp. 62–66.

[125] William M. Haynes, "CRC Handbook of Chemistry and Physics, 92nd Edition," CRC Press, 2011.

[126] Zajas, J., and Heiselberg, P., "Determination of the Local Thermal Conductivity of Functionally Graded Materials by a Laser Flash Method," *Int. J. Heat Mass Transf.*, Vol. 60, No. 1, 2013, pp. 542–548.

[127] Parker, W. J., Jenkins, R. J., Butler, C. P., and Abbott, G. L., "Flash Method of Determining Thermal Diffusivity, Heat Capacity, and Thermal Conductivity," *J. Appl. Phys.*, Vol. 32, No. 9, 1961, pp. 1679–1684.

[128] ASTM E1461 − 13 (Reapproved 2022), "Standard Test Method for Thermal Diffusivity by the Flash Method," 2022.

[129] Chatterjee, A., Sen, S., Paul, S., Roy, P., Sutradhar, G., and Ghosh, M., "Application of SiC and Graphite Reinforced Aluminium Metal Matrix Composite in Braking Systems and Its Validation Through Finite Element Analysis," *J. Inst. Eng. India Ser. D*, Vol. 104, No. 2, 2023, pp. 449–464.

[130] Chatterjee, A., Sen, S., Paul, S., Roy, P., Seikh, A. H., Alnaser, I. A., Das, K., Sutradhar, G., and Ghosh, M., "Fabrication and Characterization of SiC–Reinforced Aluminium Matrix Composite for Brake Pad Applications," *Metals*, Vol. 13, No. 3, 2023.

[131] Kaczmar, J. W., Pietrzak, K., and Wlosiński, W., "The Production and Application of Metal Matrix Composite Materials," *J. Mater. Process. Technol.*, Vol. 106, Nos. 1–3, 2000, pp. 58–67.

[132] "ASTM E1461-07, Annex X2. Standard Test Method for Thermal Diffusivity by the Flash Method."

[133] Malcolm W. Chase, "NIST–JANAF Thermomechanical Tables, Forth Edition PART I, PART II," *J. Phys. Chem. Ref. Data*, Monograph No. 9, 1998.

[134] Withers, P. J., and Bhadeshia, H. K. D. H., "Residual Stress. Part 1 – Measurement Techniques," *Mater. Sci. Technol.*, Vol. 17, No. 4, 2001, pp. 355–365.

[135] Stuhr, U., "Time–of–Flight Diffraction with Multiple Pulse Overlap. Part I: The Concept," *Nucl. Instrum. Methods Phys. Res., Sect. A*, Vol. 545, Nos. 1–2, 2005, pp. 319–329.

[136] Stuhr, U., Spitzer, H., Egger, J., Hofer, A., Rasmussen, P., Graf, D., Bollhalder, A., Schild, M., Bauer, G., and Wagner, W., "Time–of–Flight Diffraction with Multiple Frame Overlap Part II: The Strain Scanner POLDI at PSI," *Nucl. Instrum. Methods Phys. Res., Sect. A*, Vol. 545, Nos. 1–2, 2005, pp. 330–338.

[137] Eriksson, M., Bergman, F., and Jacobson, S., "On the Nature of Tribological Contact in Automotive Brakes," *Wear*, Vol. 252, Nos. 1–2, 2002, pp. 26–36.

[138] Simpleware Software ScanIP/FE v.4.3, "Simpleware Software ScanIP/FE v.4.3."

[139] Pelissou, C., Baccou, J., Monerie, Y., and Perales, F., "Determination of the Size of the Representative Volume Element for Random Quasi–Brittle Composites," *Int. J. Solids Struct.*, Vol. 46, Nos. 14–15, 2009, pp. 2842–2855.

[140] Czabaj, M. W., Riccio, M. L., and Whitacre, W. W., "Numerical Reconstruction of Graphite/Epoxy Composite Microstructure Based on Sub–Micron Resolution X–Ray Computed Tomography," *Compos. Sci. Technol.*, Vol. 105, 2014, pp. 174–182.

[141] Liu, Q., Sun, M., Sun, X., Liu, B., Ostadhassan, M., Huang, W., Chen, X., and Pan, Z., "Pore Network Characterization of Shale Reservoirs through State-of-the-Art X-Ray Computed Tomography: A Review," *Gas Sci. Eng.*, Vol. 113, 2023, p. 204967.

[142] Hibbett, Karlsson, and Sorensen Inc., "ABAQUS Analysis User's Manual Version 6.6," *Abaqus^{TM}*.

[143] Floury, J., Carson, J., and Pham, Q. T., "Modelling Thermal Conductivity in Heterogeneous Media with the Finite Element Method," *Food Bioprod. Process.*, Vol. 1, No. 2, 2008, pp. 161–170.

[144] Molina, J. M., Prieto, R., Narciso, J., and Louis, E., "The Effect of Porosity on the Thermal Conductivity of Al–12 Wt.% Si/SiC Composites," *Scr. Mater.*, Vol. 60, No. 7, 2009, pp. 582–585. Retrieved 16 January 2025

[145] Wang, J., Chen, Y., Feng, Y., Zhao, G., Jian, X., Huang, Q., Yang, L., and Xu, J., "Influence of Porosity on Anisotropic Thermal Conductivity of SiC Fiber Reinforced SiC Matrix Composite: A Microscopic Modeling Study," *Ceram. Int.*, Vol. 46, No. 18, 2020, pp. 28693–28700.

[146] Subramanian, N., and Rangaraju, K., "The Influence of Inclusion and Porosity on Thermal Conductivity of Metal Matrix Composite Using Mathematical Model," 2021.

[147] Campbell, G. S., and Norman, J. M., "An Introduction to Environmental Biophysics," Springer New York, New York, NY, 1998.

[148] Sequeira, A., Węglewski, W., Bochenek, K., Hutsch, T., Jain, A., Weissgaerber, T., and Basista, M., "Thermal Conductivity of AlSi12/Al_2O_3 –Graded Composites Consolidated by Hot Pressing and Spark Plasma Sintering: Experimental Evaluation and Numerical Modeling," *Metall. Mater. Trans. A.*, Vol. 55, No. 9, 2024, pp. 3706–3723.

[149] Nosewicz, S., Jurczak, G., Wejrzanowski, T., Ibrahim, S. H., Grabias, A., Węglewski, W., Kaszyca, K., Rojek, J., and Chmielewski, M., "Thermal Conductivity Analysis of Porous NiAl Materials Manufactured by Spark Plasma Sintering: Experimental Studies and Modelling," *Int. J. Heat Mass Transf.*, Vol. 194, 2022, p. 123070.

[150] Kida, M., Weber, L., Monachon, C., and Mortensen, A., "Thermal Conductivity and Interfacial Conductance of AlN Particle Reinforced Metal Matrix Composites," *J. Appl. Phys.*, Vol. 109, No. 6, 2011.

[151] Hasselman, D. P. H., and Johnson, L. F., "Effective Thermal Conductivity of Composites with Interfacial Thermal Barrier Resistance," *J. Compos. Mater.*, Vol. 21, 1987, pp. 508–515.

[152] Nan, C.-W., Birringer, R., Clarke, D. R., and Gleiter, H., "Effective Thermal Conductivity of Particulate Composites with Interfacial Thermal Resistance," *J. Appl. Phys.*, Vol. 81, No. 10, 1997, pp. 6692–6699.

[153] Von D A G Bruggerman, "Berechnung verschiedener physikalischer Konstanten von heterogenen Substanzen. I. Dielektrizitätskonstanten und Leitfähigkeiten der Mischkörper aus isotropen Substanzen," *Annalen der Physik*, Vol. 24, 1935, pp. 634–664.

[154] Dai, Y.-J., Gou, J.-J., Ren, X.-J., Bai, F., Fang, W.-Z., and Tao, W.-Q., "A Test-Validated Prediction Model of Thermal Contact Resistance for Ti–6Al–4V Alloy," *Appl. Energy*, Vol. 228, 2018, pp. 1601–1617.

[155] Prasher, R. S., and Phelan, P. E., "A Scattering-Mediated Acoustic Mismatch Model for the Prediction of Thermal Boundary Resistance," *J. Heat Transf.*, Vol. 123, No. 1, 2000, pp. 105–112.

[156] Wang, H., Xu, Y., Shimono, M., Tanaka, Y., and Yamazaki, M., "Computation of Interfacial Thermal Resistance by Phonon Diffuse Mismatch Model," *Mater. Trans.*, Vol. 48, No. 9, 2007, pp. 2349–2352.

[157] Ashcroft, N. W., and Mermin, N. D., "Solid State Physics," Saunders Collage Publishers, Philadelphia, 1976.

[158] Sun, Z., Tian, Z., Weng, L., Liu, Y., Zhang, J., and Fan, T., "The Effect of Thermal Mismatch on the Thermal Conductance of Al/SiC and Cu/Diamond Composites," *J. Appl. Phys.*, Vol. 127, No. 4, 2020.

[159] Chen, Y., Clausen, A. H., Hopperstad, O. S., and Langseth, M., "Stress–Strain Behaviour of Aluminium Alloys at a Wide Range of Strain Rates," *Int. J. Solids Struct.*, Vol. 46, No. 21, 2009, pp. 3825–3835.

[160] Smith, D. S., Puech, F., Nait-Ali, B., Alzina, A., and Honda, S., "Grain Boundary Thermal Resistance and Finite Grain Size Effects for Heat Conduction through Porous Polycrystalline Alumina," *Int. J. Heat Mass Transf.*, 2018.

[161] Xiu, Z., Chen, G., Wu, G., Yang, W., and Liu, Y., "Effect of Volume Fraction on Microstructure and Mechanical Properties of Si3N4/Al Composites," *Trans. Nonferrous Met. Soc. China.*, Vol. 21, 2011, pp. s285–s289.

[162] R. B. Bird, W. E. Stewart, and E. N. Lightfoot, "Transport Phenomena," John Wiley & Sons, New York, 2007.

[163] Woodside, W., and Messmer, J. H., "Thermal Conductivity of Porous Media. II. Consolidated Rocks," *J. Appl. Phys.*, Vol. 32, No. 9, 1961, pp. 1699–1706.

[164] Bruggeman, D. A. G., "Berechnung Verschiedener Physikalischer Konstanten von Heterogenen Substanzen. I. Dielektrizitätskonstanten Und Leitfähigkeiten Der Mischkörper Aus Isotropen Substanzen," *Annalen der Physik*, Vol. 416, No. 7, 1935, pp. 636–664.

[165] Hashin, Z., and Shtrikman, S., "A Variational Approach to the Theory of the Elastic Behaviour of Multiphase Materials," *J. Mech. Phys. Solids*, Vol. 11, No. 2, 1963, pp. 127–140.

[166] Hashin, Z., "Assessment of the Self Consistent Scheme Approximation: Conductivity of Particulate Composites," *J. Compos. Mater.*, Vol. 2, No. 3, 1968, pp. 284–300.

[167] Stránský, J., Vorel, J., Zeman, J., and Šejnoha, M., "Mori–Tanaka Based Estimates of Effective Thermal Conductivity of Various Engineering Materials," *Micromachines*, Vol. 2, No. 2, 2011, pp. 129–149.

[168] Xin, L., Xu, J., Li, Z., and Li, Y., "A Mori–Tanaka Method Based Theoretical Approximation for Functionally Graded Thick Wall Tube under Combined Thermal and Mechanical Loads," *J. Therm. Stress.*, Vol. 46, No. 3, 2023, pp. 229–250.

[169] Muraleedharan, M. G., Gordiz, K., Ju, S., Shiomi, J., Yang, V., and Henry, A., "Thermal Interface Conductance between Aluminum and Aluminum Oxide: A Rigorous Test of Atomistic Level Theories," *Mater. Sci.:Condens. Matter*, 2018. Retrieved 7 October 2023.

[170] Stoner, R. J., and Maris, H. J., "Kapitza Conductance and Heat Flow between Solids at Temperatures from 50 to 300 K," *Phys. Rev. B*, Vol. 48, No. 22, 1993, pp. 16373–16387.

[171] Hopkins, P. E., Salaway, R. N., Stevens, R. J., and Norris, P. M., "Temperature-Dependent Thermal Boundary Conductance at Al/Al_2O_3 and Pt/Al_2O_3 Interfaces," *Int. J. Thermophys.*, Vol. 28, No. 3, 2007, pp. 947–957.

[172] Hopkins, P. E., Beechem, T., Duda, J. C., Hattar, K., Ihlefeld, J. F., Rodriguez, M. A., and Piekos, E. S., "Influence of Anisotropy on Thermal Boundary Conductance at Solid Interfaces," *Phys. Rev. B*, Vol. 84, No. 12, 2011, p. 125408.

[173] Zare, R., Sharifi, H., Saeri, M. R., and Tayebi, M., "Investigating the Effect of SiC Particles on the Physical and Thermal Properties of Al6061/SiC$_p$ Composite," *J. Alloys Compd.*, Vol. 801, 2019, pp. 520–528.

[174] Xu, Y., Tanaka, Y., Murata, M., Kamihira, K., Isoda, Y., and Yagi, K., "Thermal Conductivity of Unidirectionally Aligned SiC Whisker Reinforced Al Alloy Matrix Composite with Interfacial Thermal Resistance," *Mater. Trans.*, Vol. 46, No. 2, 2005, pp. 148–151.

[175] Su-Yuan, B., Zhen-An, T., Zheng-Xing, H., Jun, Y., and Jia-Qi, W., "Thermal Conductivity Measurement of Submicron-Thick Aluminium Oxide Thin Films by a Transient Thermo-Reflectance Technique," *Chin. Phys. Lett.*, Vol. 25, No. 2, 2008, p. 593.

[176] Modi, O. P., Prasad, B. K., Yegneswaran, A. H., and Vaidya, M. L., "Dry Sliding Wear Behaviour of Squeeze Cast Aluminium Alloy–Silicon Carbide Composites," *Mater. Sci. Eng., A.*, Vol. 151, No. 2, 1992, pp. 235–245.

[177] Surappa, M. K., Prasad, S. V., and Rohatgi, P. K., "Wear and Abrasion of Cast Al–Alumina Particle Composites," *Wear*, Vol. 77, No. 3, 1982, pp. 295–302.

[178] Bai, B. N. P., Ramasesh, B. S., and Surappa, M. K., "Dry Sliding Wear of A356–Al–SiC$_p$ Composites," *Wear*, Vol. 157, No. 2, 1992, pp. 295–304.

[179] Kuo, S. M., and Rigney, D. A., "Sliding Behavior of Aluminum," *Mater. Sci. Eng., A.*, Vol. 157, No. 2, 1992, pp. 131–143.

[180] Sannino, A. P., and Rack, H. J., "Dry Sliding Wear of Discontinuously Reinforced Aluminum Composites: Review and Discussion," *Wear*, Vol. 189, Nos. 1–2, 1995, pp. 1–19.

[181] Rohatgi, P. K., Schultz, B. F., Daoud, A., and Zhang, W. W., "Tribological Performance of A206 Aluminum Alloy Containing Silica Sand Particles," *Tribol. Int.*, Vol. 43, Nos. 1–2, 2010, pp. 455–466.

[182] Ahmad, F., Lo, S. H. J., Aslam, M., and Haziq, A., "Tribology Behaviour of Alumina Particles Reinforced Aluminium Matrix Composites and Brake Disc Materials," Vol. 68, 2013, pp. 674–680.

[183] Oda, N., Sugimoto, Y., Higuchi, T., and Minesita, K., "Development of Disk Brake Rotor Utilizing Aluminum Metal Matrix Composite," 1997.

[184] Hosking, F. M., Portillo, F. F., Wunderlin, R., and Mehrabian, R., "Composites of Aluminium Alloys: Fabrication and Wear Behaviour," *J. Mater. Sci.*, Vol. 17, No. 2, 1982, pp. 477–498.

[185] Kwok, J. K. M., and Lim, S. C., "High-Speed Tribological Properties of Some Al/SiCp Composites: II. Wear Mechanisms," *Compos. Sci. Technol.*, Vol. 59, No. 1, 1999, pp. 65–75.

[186] Dasgupta, R., Modi, O. P., Yadav, M. S., and Yegneswaran, A. H., "Mechanism of Material Removal under High Stress Abrasive Wear Conditions under Varying Experimental Conditions," *J. Mater. Sci. Lett.*, Vol. 20, No. 20, 2001, pp. 1837–1839.

[187] Das, S., Mondal, D. P., Sawla, S., and Dixit, S., "High Stress Abrasive Wear Mechanism of LM13–SiC Composite under Varying Experimental Conditions," *Metall. Mater. Trans. A.*, Vol. 33, No. 9, 2002, pp. 3031–3044.

[188] P. Suh, N., "The Delamination Theory of Wear," *Wear*, Vol. 25, No. 1, 1973, pp. 111–124.

[189] Rice, R. W., "Micromechanics of Microstructural Aspects of Ceramic Wear," 1985.

[190] Long, T. T., Nishimura, T., Aisaka, T., and Morita, M., "Wear Resistance of Al–Si Alloys and Aluminium Matrix Composites," *Mater. Trans. JIM.*, Vol. 32, No. 2, 1991, pp. 181–188.

[191] Morstein, C. E., Klemenz, A., Dienwiebel, M., and Moseler, M., "Humidity–Dependent Lubrication of Highly Loaded Contacts by Graphite and a Structural Transition to Turbostratic Carbon," *Nat. Commun.*, Vol. 13, No. 1, 2022, p. 5958.

[192] Takeuchi, E., "The Mechanisms of Wear of Cast Iron in Dry Sliding," *Wear*, Vol. 11, No. 3, 1968, pp. 201–212.

[193] Rettig, M., Grochowicz, J., Käsgen, K., Wilwers, T., Labrador, R., Egidazu, N., Gaztanaga, I., Verpoort, C., and Sin, A., "Aluminium Brake Rotor," 2020.

[194] Chioibasu, D., Mihai, S., Cotrut, C. M., Voiculescu, I., and Popescu, A. C., "Tribology and Corrosion Behavior of Gray Cast Iron Brake Discs Coated with Inconel 718 by Direct Energy Deposition," *Int. J. Adv. Manuf. Technol.*, Vol. 121, No. 7, 2022, pp. 5091–5107.

[195] Malaki, M., Fadaei, T. A., Niroumand, B., Gupta, M., "Wettability in Metal Matrix Composites," *Metals*, Vol. 11, No. 7, 2021, p. 1034.

[196] Gupta, V., and Singh, S. B., "Effect of Residual Stress and Reinforcement Geometry in an Anisotropic Composite Rotating Disc Having Varying Thickness," *Int. J. Comput. Mater. Sci. Eng.*, Vol. 01, No. 04, 2012, p. 1250035.

[197] Węglewski, W., Krajewski, M., Bochenek, K., Denis, P., Wysmołek, A., and Basista, M., "Anomalous Size Effect in Thermal Residual Stresses in Pressure Sintered Alumina–Chromium Composites," *Mater. Sci. Eng., A.*, Vol. 762, 2019, p. 138111.

[198] Zhang, S., Ran, Y., Murphy, A., Zhang, G., and Wang, W., "Residual Stress Analysis of Gray Cast Iron Manufacturing Processes," *Mater. Manuf. Process.*, Vol. 35, No. 15, 2020, pp. 1781–1788.

[199] Li, S., Wang, G., "Introduction to Micromechanics and Nanomechanics," 2nd Edition, 2018.